Controlling crystallinity of organic thin films to improve optical and electrical properties in organic optoelectronic devices

유기광전소자의 전기광학적 특성 향상을 위한 결정제어

2018년 8월

서울대학교 대학원

재료공학 전공

최 민 수

Abstract

Controlling crystallinity of organic thin films to improve optical and electrical properties in organic optoelectronic devices

Min-Soo Choi

Department of Materials Science and Engineering

The Graduate School

Seoul National University

Organic semiconductors have been researched intensively because of their advantages of low processing cost, a light weight, substrate flexibility, and applicability to large-area fabrication. A study on organic optoelectronic device, which is consist of photo-active organic layers, is one of the highlighted research field in academia and industry. The organic optoelectronic device can convert between light energy and electrical energy, for example, organic photovoltaic (OPV) and organic photodetector (OPD) which can generate free charges from incident photons, resulting in electrical power or light detection.

In the organic layer, a change in crystallinity of domains and orientation of molecules influences not only electrical properties but also optical properties of organic layer. Thus, a control of crystallinity as well as molecular orientation can be a good strategy to improve the optical properties and electrical properties.

First, we controlled the crystallinity of C_{70} in C_{70}-based organic photovoltaic cells. The crystallinity of 5% 4,4′-Cyclohexylidenebis[N,N-bis(4-methylphenyl)-benzenamine] (TAPC) doped C_{70} is improved significantly, especially the (111)-oriented face-centered cubic structure of C_{70}, if CuI was used as a templating layer. The device with oriented C_{70} domain with increased crystallinity exhibited higher hole mobility (3.3×10^{-5} cm^2 V^{-1} s^{-1}) and electron mobility (5.3×10^{-5} cm^2 V^{-1} s^{-1}) compared to reference one which exhibited hole mobility of 8.2×10^{-6} cm^2 V^{-1} s^{-1} and electron mobility of 3.4×10^{-5} cm^2 V^{-1} s^{-1}. The enhanced mobility led to higher charge extraction. As a result, the use of the templating layer in C_{70}-based solar cells with low donor concentration resulted in significant improvement of the fill factor from 0.51 to 0.57 and the power conversion efficiency from 5.56% to 6.23% under simulated AM 1.5G, 1 sun irradiation. This result demonstrates that the CuI templating layer is effective at improving the crystallinity of the fullerene derivatives as well as the donor materials.

Second, we controlled the initial growth mode of lead (II) phthalocyanine (PbPc) molecules on to C_{60} substrate, which is required structure for the inverted near-infrared (NIR) OPDs which can be combined

with n-channel silicon-based integrated circuits. A spectral response to 1,000 nm was achieved by depositing PbPc on a heated C_{60} layer to form a triclinic rather than a monoclinic phase. The change in initial growth mode was investigated with 10 nm thick PbPc layer on to C_{60} substrate by X-ray diffraction pattern. As a result, NIR OPDs with substrate heating exhibited a much higher responsivity (35.8 mA/W at 960 nm) compared to a device fabricated without substrate heating (8.4 mA/W). The external quantum efficiency also increased from 0.9 to 4.4%.

To further enhancement of NIR response, inverted NIR OPDs with bulk-heterojunction (BHJ) structure was fabricated. In general, PbPc loses crystallinity in a blended layer, which is photo-active layer in OPDs with BHJ structure, resulting in weak NIR absorption in blend films. In this case, neither the use of a templating layer without heating nor substrate heating without the templating layer induced NIR absorption in the blend layer. To form the triclinic phase responsible for NIR light absorption, the substrate was heated during fabrication and C_{60} was used as a templating layer, as well as an electron extraction layer, for an inverted structure. NIR absorption near 950 nm was enhanced, and the structural properties of the film changed dramatically. The OPDs with enhanced NIR absorption exhibited a responsivity of 244 mA/W and an external quantum efficiency of 31.1% at a reverse bias of −3 V and 970 nm. The OPD detectivity also increased to 9.01×10^{12} cm $Hz^{1/2}$/W and 1.36×10^{11} cm $Hz^{1/2}$/W under zero and reverse bias of −3 V, respectively. Furthermore, the origin of the dark current density is investigated. The injection current is

blocked by inserting a blocking layer which can suppress the injection of electrons and analyzed through a theoretical model.

Contents

List of Tables

List of Figures

Chapter 1. Introduction

1.1 Motivation and outline of thesis

Motivation

Organic semiconductors have been researched intensively because of their advantages of low processing cost, a light weight, substrate flexibility, and applicability to large-area fabrication. [1–7] Additionally, organic materials can be designed and synthesized for various purposes, leading to controlling an optical property as well as an electrical property. A study on organic optoelectronic device, which is consist of photo-active organic semiconductor layers, is one of the highlighted research field in academia and industry. The organic optoelectronic device can convert between light energy and electrical energy, for example, organic light emitting diode can produce light energy from electrical energy. Nowadays, organic light emitting diodes are used in industry for various devices, such as display in television and mobile phone and solid state lighting. In contrast, organic photovoltaic cells (OPV) and organic photodetector (OPD) can generate free charges from incident photons resulting in electrical power or light detection.

Just as inorganic materials show crystallinity in thin film, organic materials can possess the crystallinity in the thin film. For decades, the crystallinity of organic materials has been widely researched in the field of organic thin film transistors. [8–14] A major research topic in this field was the

increase in charge mobility of organic materials via control of crystallinity. The studies on crystallinity have also been carried out in the field of OPVs. A change in crystallinity of domains and orientation of molecules in an organic thin film influences not only electrical properties but also optical properties of organic layer. For instance, phthalocyanine dyes, which absorb visible light, show various optical properties with controlled crystal structure. [15–20] A Control of crystallinity as well as molecular orientation can be a good strategy to improve the optical properties and electrical properties.

Outline of thesis

In **chapter 1**, the method to characterize the performance of organic OPVs and OPDs with current density-voltage (J-V) curves and incident photon-to-current efficiency (IPCE), which is same as external quantum efficiency (EQE), is presented. In addition, calculation of OPD parameters, responsivity and detectivity, is also exhibited. Then, introduction to controlling crystallinity is discussed.

In **chapter 2**, an enhancement of fill factor through an increase of the crystallinity in fullerene-based OPV is discussed. The crystallinity of 5% 4,4′-Cyclohexylidenebis[N,N-bis(4-methylphenyl)-benzenamine] (TAPC) doped C_{70} is improved significantly, especially the (111)-oriented face-centered cubic structure of C_{70}, if CuI was used as a templating layer. The device with oriented C_{70} domain with increased crystallinity exhibited higher hole mobility (3.3 ×

10^{-5} cm^2 V^{-1} s^{-1}) and electron mobility (5.3×10^{-5} cm^2 V^{-1} s^{-1}) compared to reference one which exhibited hole mobility of 8.2×10^{-6} cm^2 V^{-1} s^{-1} and electron mobility of 3.4×10^{-5} cm^2 V^{-1} s^{-1}. As a result, the use of the templating layer in C$_{70}$-based solar cells with low donor concentration resulted in significant improvement of the fill factor from 0.51 to 0.57 and the power conversion efficiency from 5.56% to 6.23% under simulated AM 1.5G, 1 sun irradiation. This result demonstrates that the CuI templating layer is effective at improving the crystallinity of the fullerene derivatives as well as the donor materials.

In **chapter 3**, inverted NIR OPD with oriented lead (II) phthalocyanine molecules via substrate heating is introduced. We controlled the initial growth mode of lead (II) phthalocyanine (PbPc) molecules on to C$_{60}$ substrate, which is required structure for the inverted near-infrared (NIR) OPDs which can be combined with n-channel silicon-based integrated circuits. A spectral response to 1,000 nm was achieved by depositing PbPc on a heated C$_{60}$ layer to form a triclinic rather than a monoclinic phase. The change in initial growth mode was investigated with 10 nm thick PbPc layer on to C$_{60}$ substrate by x-ray diffraction pattern. As a result, NIR OPDs with substrate heating exhibited a much higher responsivity (35.8 mA/W at 960 nm) compared to a device fabricated without substrate heating (8.4 mA/W). The external quantum efficiency also increased from 0.9 to 4.4%.

To further enhancement of NIR response, inverted NIR OPDs with bulk-

heterojunction (BHJ) structure is introduced in **chapter 4**. In general, PbPc loses crystallinity in a blended layer, which is photo-active layer in OPDs with BHJ structure, resulting in weak NIR absorption in blend films. In this case, neither the use of a templating layer without heating nor substrate heating without the templating layer induced NIR absorption in the blend layer. To form the triclinic phase responsible for NIR light absorption, the substrate was heated during fabrication and C_{60} was used as a templating layer, as well as an electron extraction layer, for an inverted structure. NIR absorption near 950 nm was enhanced, and the structural properties of the film changed dramatically. The OPDs with enhanced NIR absorption exhibited a responsivity of 244 mA/W and an external quantum efficiency of 31.1% at a reverse bias of −3 V and 970 nm. The OPD detectivity also increased to 9.01×10^{12} cm $Hz^{1/2}$/W and 1.36×10^{11} cm $Hz^{1/2}$/W under zero and reverse bias of −3 V, respectively. Furthermore, the origin of the dark current density is investigated. The injection current is blocked by inserting a blocking layer which can suppress the injection of electrons and analyzed through a theoretical model (in **chapter 5**).

1.2 Working principle of organic photovoltaic cells and organic photodetectors

OPVs and OPDs, which can convert light energy (photons) to electrical energy (free charges), consist of donor and acceptor materials. In figure 1.1 shows charge generation mechanism of OPV and OPD, which can be described with several steps.

(1) Light absorption: The incident photons generate hole-electron pairs in the organic molecules due to electron transition from highest occupied molecular orbital (HOMO) to lowest unoccupied molecular orbital (LUMO) bands. The absorption depends on molecular extinction coefficient and the thickness of organic layer.

(2) Exciton generation: The generated hole-electron pairs by photon absorption results in so-called 'exciton'. These excitons have energy which is smaller than the energy gap between the HOMO and LUMO bands. The energy difference between this energy and energy gap is called "exciton binding energy" and usually in range of ~0.3 eV, which is much higher than inorganic case (~10 meV). Therefore, the generated excitons in the organic layer cannot be separated into free charge carriers.

(3) Exciton diffusion: The generated excitons in the organic layer can diffuse to the donor/acceptor interface according to the concentration gradient. In order to absorb all the light, the thickness of the photo-active layer should increase
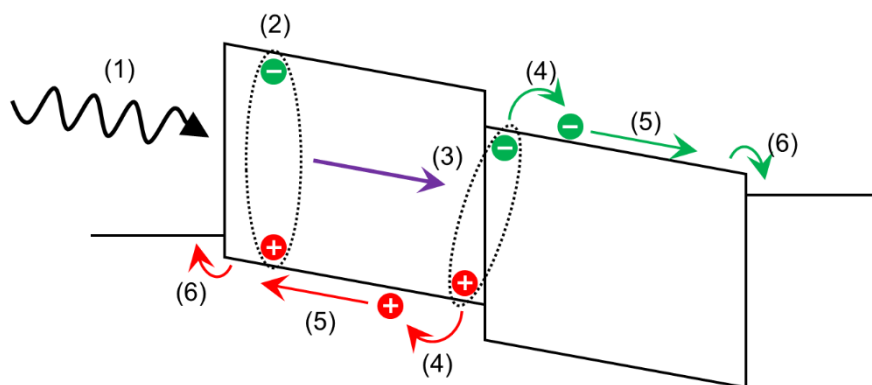
Figure 1.1 Charge generation mechanism of organic photovoltaic and photodetector.

up to 100 nm. However, since the exciton diffusion distance is ~ 10 nm, the device with planar-heterojunction is mainly composed of organic layers with a thickness of 20 ~ 40 nm. A bulk-heterojunction structure is proposed as a device structure to overcome this.

(4) Hole-electron separation

The excitons diffused to the donor/acceptor interface form a charge-transfer (CT) state at the interface. To form CT state, the LUMO level of donor should be higher than that of acceptor and the HOMO level of donor should be lower than that of acceptor. The CT state is still tied to the electrical attraction, and the local field (for example, built-in potential or applied electric field) at the interface is needed to overcome this.

(5) Free charge carrier transport

The free charges separated from CT state at the interface go through the organic material to the electrode. Traps or energy barriers inside the organic material can interfere with charge transport. If this obstacle is absent, the charge extraction efficiency can approach ~100%.

(6) Charge collection

The energy level of the anode should be higher than the HOMO level of a donor material in order to remove charge extraction barrier which can interrupt the charge extraction. However, the anode with too high energy level may reduce the electric field inside the device, which may hinder the effective

charge extraction. For the same reason, the energy level of the cathode should be lower than the LUMO level of an acceptor material.

As shown in Figure 1.2, OPVs and OPDs have the same principle but differ in driving method. OPV is a device that produces electricity. The current flows in the opposite direction to the applied voltage, leading to an electric power generation. On the other hand, an OPDs is a device for detecting light, which applies a reverse voltage to maximize extraction efficiency of free charges formed inside.
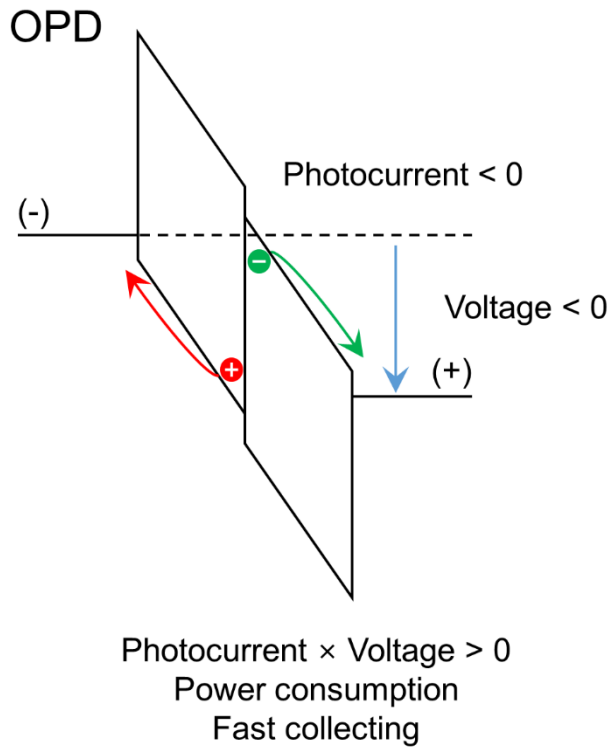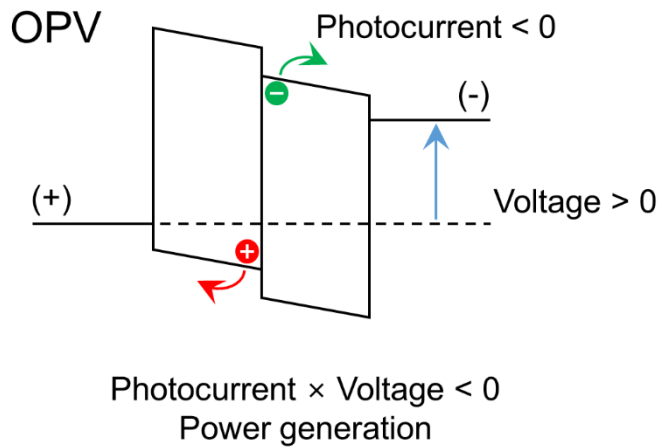
Figure 1.2 Schematic energy band diagram of organic photovoltaic and organic photodetector. They have different working conditions.

1.3 Device characterization of organic photovoltaic cells and organic photodetectors

The current density-voltage (J-V) characteristics represent the performance of not only OPVs but also OPDs. As shown in Figure 1.3, the graph generally shows diode characteristics. The device characteristics are measured from the reverse voltage region to the region where charge injection occurs, and the performance of the device is extracted using the obtained J-V curves.

OPV characteristics from J-V curves

To understand OPV characteristics, a graph of the positive voltage range should be analyzed. When a photocurrent is generated with incident photons, the current has a negative value. The photocurrent at zero bias is called short-circuit current (J_{SC}). As the applied voltage increases, the photocurrent decreases and the point where the photocurrent becomes zero is called the open-circuit voltage (V_{OC}). The V_{OC} is closely related to the HOMO level of donor and LUMO level of acceptor. The maximum power (P_{MAX}) is the value that indicates the obtainable power from the device. The fill factor (FF) is expressed by the following equation below;

$$FF = \frac{P_{MAX}}{J_{SC} \times V_{OC}} \ .$$
(1.1)

The power conversion efficiency (PCE) of OPV means the ration of the
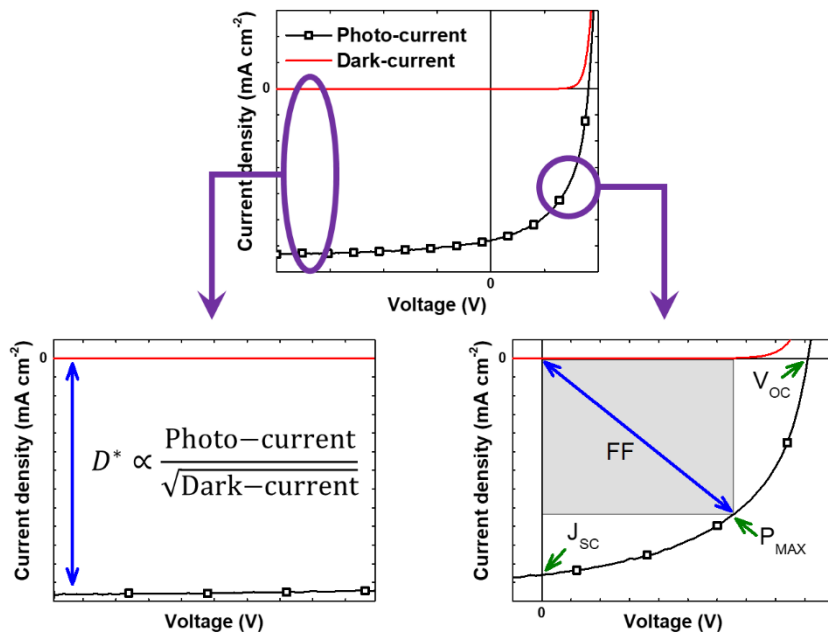
Figure 1.3 Working conditions of organic photovoltaic and organic photodetector.

incident light ($P_{incident}$) energy to electrical energy and can be calculated as follows;

$$PCE = \frac{P_{MAX}}{P_{incident}} = \frac{J_{SC} \times V_{OC} \times FF}{P_{incident}} \ .$$ (1.2)

External quantum efficiency (EQE)

External photon efficiency (EQE) means the ratio of the number of output charge carriers to the number of photons incident at a particular wavelength. It is used equivalently with the Incident photon-to-current efficiency (IPCE) and can be calculated as follows;

$$EQE = \frac{\# \text{ of collected charge carriers}}{\# \text{ of incident photons}} = \frac{I_{photo}/q}{P_{incident}/hv}$$ (1.3)

where I_{photo}, q, h, v indicate the measured photocurrent, the elementary charge, the Planck constant and the frequency of the light, respectively.

Responsivity of OPD

Responsivity means the ratio of output current (photocurrent generated from incident photon) to the input optical power at a particular wavelength. It can be defined as follows;

$$R = \frac{I_{photo}}{P_{incident}}$$ (1.4)

The unit of responsivity is A/W.

Detectivity of OPD

Responsivity and EQE show the response depending on the wavelength, but these do not mean the degree of detection. The degree of detection should include information about the minimum light that the device can detect. The Noise Equivalent Power, NEP, is the minimum light power to generate signal current (i_{signal}) equal to noise current (i_{noise}) with bandwidth (B) of 1 Hz. It can be expressed as;

$$NEP \; [\text{W} \cdot \text{Hz}^{-0.5}] = \frac{i_{signal} (= i_{noise}) \; [\text{A}]}{R \; [\text{A/W}] \cdot \sqrt{B} \; [\text{Hz}^{0.5}]} \qquad (1.5)$$

where R is the responsivity discussed above. Bandwidth means frequency range from DC (0 Hz) to operating frequency. When bandwidth is expanded 100 times, NEP is decreased 10 times and this means that more detecting time makes smaller NEP.

With the consideration of detector area, specific detectivity, D^*, can be described as;

$$D^* = \frac{\sqrt{A}}{NEP} \qquad (1.6)$$

where A is area of detector. The unit of detectivity is cm $\text{Hz}^{1/2}$ W^{-1}.

1.4 Crystallinity control for organic thin films

The crystallinity in organic semiconductor is generally used to mean the concept of grain size, domain size, molecular orientation, molecular packing, and the like. In an organic photoelectric device, the crystallinity greatly affects the opto-electrical properties of the device. In the field of organic light emitting diode research, the direction of the light generated inside is changed according to the direction of the transition dipole moment.[21,22] As the horizontal orientation of the transition dipole moment increases, the photon oscillating in the horizontal direction increases and the light that can be extracted to the outside increases, that is, light extraction efficienty increses. The crystallinity of the organic thin film can be increased through molecular orientation control or crystal control in order to enhance the charge carrier mobility for high performance organic thin film transistor.[8,11,13,23] Enhancement of crystallinity or phase transformation can be one of the ways to improve the light absorption of organic this films. [18,24–27]

The method of controlling the crystallinity of the organic thin film can be roughly classified into three types. A method of changing the process conditions during the formation of the thin film (figure 1.4), a method of inducing crystallization by introducing an additional process after the film formation (figure 1.5a and 1.5b) and an interfacial control which changes the characteristics of the substrate on which the thin film is to be formed (figure 1.5c).

14

Control during film formation

Changing deposition rate can induce the crystallinity enhancement or different crystal structure. For example, slow deposition rate result in triclinic formation of PbPc rather than monoclinic phase which is formed with fast deposition rate.[24,28] Deposition with tilted angle, glancing angle depositon, can control the morphology of not only the thin films with glancing angle depositon but also a film formed onto the film.[29] Applying an electric or magnetic field during the film formation can result crystallinity control.[30,31]

Control after film formation

After film formation, heat treatment[24,32] or solvent treatment[33–35] can change the crystallinity of organic thin film, as shown in figure 1.5a and 1.5b.

Control the interface

An interface modification can control the film formed onto the interface. The use of templating layer, surface treatment such as acid or base, and substrate heating can change the substrate characteristics, leading to different film growth onto the substrate (shown in figure 1.5c).[18,19,36–40]
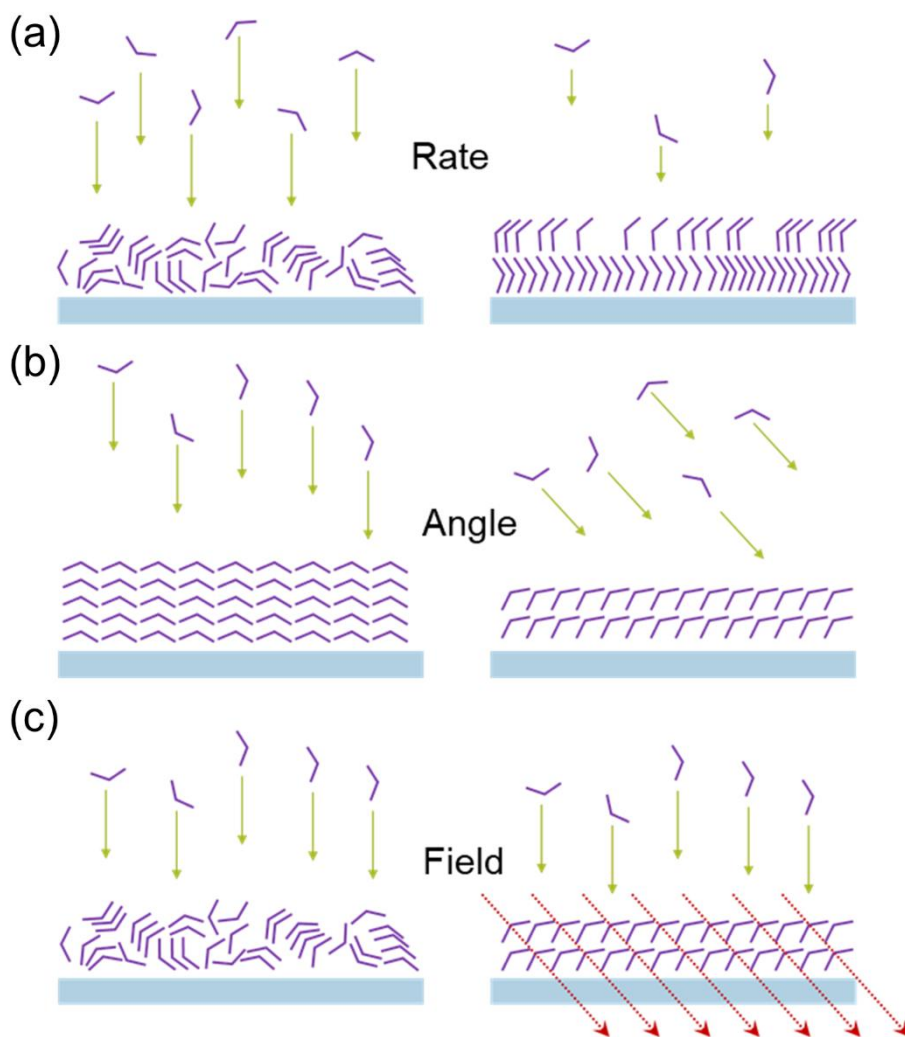
Figure 1.4 Controling structural properties of organic thin films during a film formation with (a) different deposition rate, (b) different deposition angle and (c) applying external field.
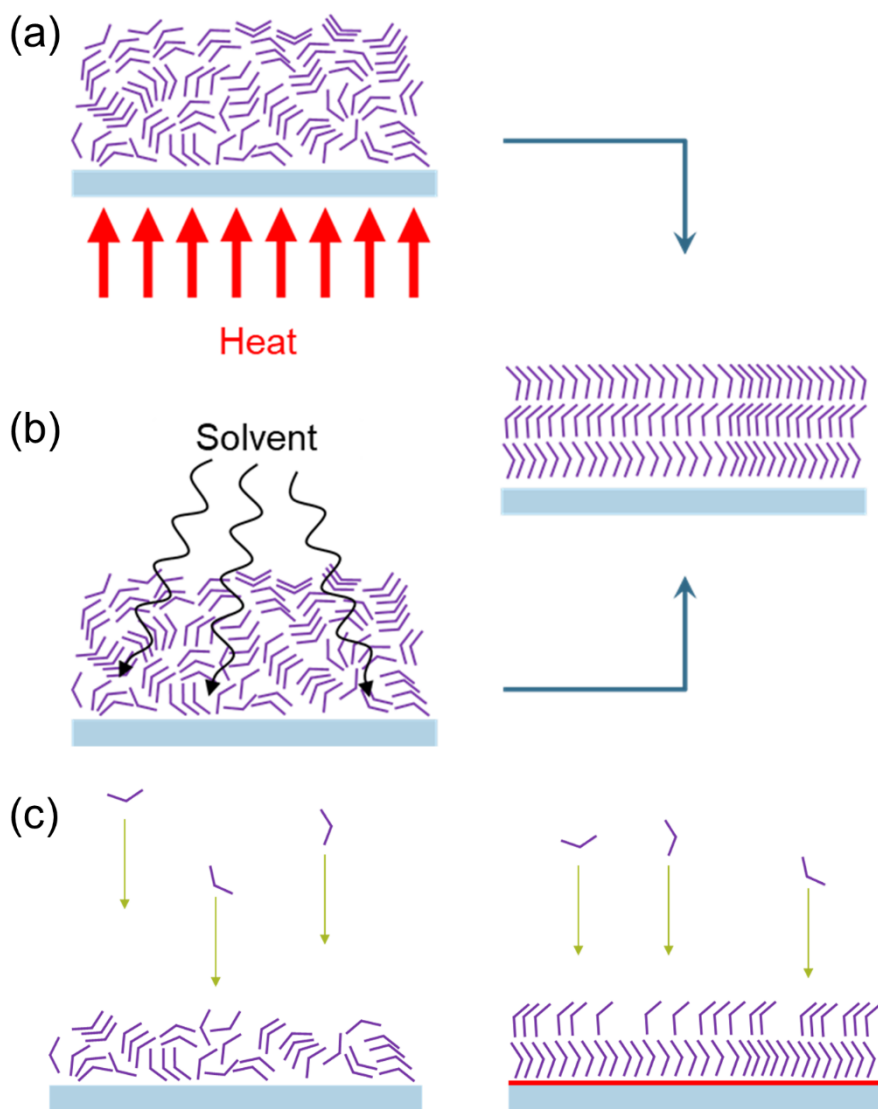
Figure 1.5 Controling structural properties of organic thin films after a film formation with (a) heat and (b) solvent treatment. (c) Controling structural properties of organic thin films with interface modification.

1.5 Introduction to crystallinity control in fullerene-based organic photovoltaic cells

Small-molecule organic photovoltaic cells (OPVs) have been highlighted because of their advantages of ease of processing, low cost, high purity, flexibility, and easiness to control their molecular properties by synthesis.[4,5] For highly efficient OPVs, fullerene derivatives are used as common acceptor materials because of high electron mobility[9] and their energy levels to form charge-transfer states with various donor materials.[41–46] Among them, C_{70} as well as C_{60} is known to form intermolecular charge-transfer excitons between the molecules in solid films. The formation of a charge-transfer exciton results in extra absorption from 400 to 700 nm, leading to more photocurrent generation.[47,48] In addition, the charge-transfer exciton can be dissociated easily by doping a small amount of donor materials, such as 1,1-bis[4-bis(4-methylphenyl)-aminophenyl]cyclohexane (TAPC),[49] tetraphenyldibenzoperiflanthene,[50,51] and tris[4-(5-phenylthiophen-2-yl)phenyl]-amine.[52] With this property of C_{70}, OPVs with low donor concentration have been highlighted showing high short-circuit current density (J_{SC}) and open-circuit voltage (V_{OC}).[49–52] In this system, the electron mobility is high enough to extract the electrons because of the large portion of fullerene, which possesses an n-type property.[53–56] However, the hole mobility is relatively low, which causes a reduction of the fill factor (FF) due to the unbalanced electron and hole mobilities.[57,58] The increase of the hole mobility

Table 1.1 Previous reports on templating layer for organic photovoltaic cells

Templating material	Templated material	Change in physical properties	Reference
ZnPc	PbPc	Increase NIR absorption and hole collection	19
BP2T	ZnPc	Increase crystallinity and absorption	59
CuI	CuPc	Change molecular packing (edge-on → face-on) and enhance absorption	27
6T, VOPc	PbPc	Increase NIR absorption	37
CuI	ZnPc	CuI deposition with angle and enhanced absorption	29
CuI	ZnPc	Change molecular packing (edge-on → face-on) and enhance absorption and diffusion length	25
BP2T	TiOPc	Phase change and obtain NIR absorption	60
CuI	PbPc	Increase crystallinity and NIR absorption	20
CuI	PbPc	Increase NIR absorption and diffusion length	18
Pentacene	PbPc	Increase NIR absorption	36
CuI	ZnPc	Change molecular packing (edge-on → face-on) and enhance absorption	26
CuI	PbPc	Increase crystallinity and NIR absorption	24
CuBr	PbPc	Increase crystallinity and NIR absorption	38
CuCl, CuBr, CuI	PbPc	Increase crystallinity lattice matching	16

is a critical factor in obtaining a higher power conversion efficiency (PCE) with improving FF.

In organic films, the optical and electrical properties are significantly influenced by the molecular orientation, crystal structure, and crystallinity. The transition dipole moment has an intimate relationship with the molecular orientation, and control of the molecular orientation can result in a remarkable increase of the photocurrent coming from the increased absorption coefficient.[16,18,20,26,27,38] The charge mobilities in a molecular film are also influenced by the molecular orientation, crystallinity, and crystal structure. High crystalline films possess low defect density, leading to high charge mobility.[11–13,23] There has been a large effort to increase the crystallinity, especially in planar heterojunction solar cells. Among them, the use of a templating layer has been widely studied as an effective way, as summarized in Table 12.1, and CuI is known as an effective templating material for organic donor materials to improve the PCE combined with controlling the crystal structure and molecular orientation for organic materials.[16,18,26,27,38] Unfortunately, however, there are few reports on control of the crystallinity of fullerene derivatives using a templating layer. Pentacene[13,23] and diindenoperylene[10,12] were reported to increase thec rystallinity of C_{60} for n-type transistors. However, their high highest occupied molecular orbital (HOMO) energy may reduce V_{OC} if adopted in solar cells.

1.6 Introduction to crystallinity control for near-infra red organic photodetector

Organic photodetectors (OPDs) have been researched intensively and offer the advantages of low processing cost, a light weight, substrate flexibility, and applicability to large-area fabrication.[6,7,61,62] Additionally, various organic materials can be combined to produce OPDs with color selectivity or panchromatic characteristics.[63–72] The high external quantum efficiency (EQE) of OPDs in the near-infrared (NIR) region from 800 to 1,000 nm is promising with regards to potentially replacing silicon-based NIR photodetectors.[62,73] In particular, OPDs operating in the range of 930-960 nm are important for daylight applications such somatosensory and iris or face recognition because of the low intensity of solar irradiation, due to H_2O absorption in the atmosphere. Recently, a number of studies on NIR OPDs responding to wavelengths > 800 nm have been reported[17,68,77,69–76]; however, development of OPDs responding at NIR wavelengths > 900 nm with the low dark current density under a reverse bias are highly desired[78–81]. Few small molecular OPDs have been reported to our best knowledge even though a few polymer-based NIR photodetectors have been reported operation at the long wavelength.

To combine OPDs with integrated circuits, the structure of the OPD needs to be modified. OPDs having a conventional structure that absorbs light from the bottom side are not desirable for stacking the device on an integrated

Table 1.2 Previous reports on near-infrared organic photodetectors.

No.	Materials	Process (structure)	EQE @ λ ,V	Detectivity (cm Hz$^{1/2}$/W)	Reference
1	PTT	Solution (BA Normal)	19% @ 850 nm, 0 V 38% @ 850 nm, - 5 V	2.60×10^{10} @ 850, 0 V 7.41×10^{9} @ 850, -5 V	82
2	PDDTT	Solution (BA Normal)	26% @ 800 nm, -0.5 V	2.3×10^{13} @ 800	68
3	2 Zn-metallated porphyrins Psub & Pfused	Solution (BA Normal)	2.1% @ 1090 nm 6.5% @ 1345 nm	1.6×10^{11} @ 1090, 0 V 2.3×10^{10} @ 1350, 0 V	83
4	Psub:PCBM:Bipy = 1:0.1:1	Solution (BA Normal)	3.6% @ 1150 nm, 0V	8.8×10^{11} @ 1150, 0 V	84
	Pfused:PCBM:Bipy = 1:0.75:1		10.5% @ 1400 nm, 0V	8.2×10^{10} @ 1400, 0 V	
	Pfused:Bipy = 1:3		13.5% @ 1385 nm, 0V	2.1×10^{10} @ 1385, 0 V	
5	PDTTP	Solution (BA Normal)	49.6% @ 810 nm, -5 V	2.5×10^{10} @ 810, -1 V 6.7×10^{9} @ 810, -3 V	69
6	SnNcCl$_2$	Vacuum (BA Normal)	3% @ 900nm, 0 V 22% @ 900nm, -6 V	10^{12} @ 900, 0V 2.2×10^{10} @ 900, -3V	70
7	PDDTT	Solution (BA Inverted)	27% @ 800nm, 0 V	2×10^{14} @ 800, 0V	85
8	PTZBTTT-BDT	Solution (BA Normal)	16% @ 800nm, 0 V	1.75×10^{13} @ 800, 0V	75
9	M1 (D-A-D) D: TPT,A: TT	Solution (BA Normal)	7% @ 800nm, -2 V	5.0×10^{11} @ 800, -0.1 V	86
10	DHTBTEZP	Solution (BA Normal)	23.5% @ 800nm, 0V 24.6% @ 865nm, 0V	4.56×10^{12} @ 800, 0V	87
11	PTZBTTT-BDT	Solution (BA Inverted)	18.2% @ 800nm, 0 V	1.02×10^{13} @ 800, 0V	88
12	PbPc	Vacuum (BA Normal)	18.0% @ 900nm, 0 V 33.2% @ 900nm, -6 V	2.34×10^{11} @ 900, 0V	17
13	PbPc	Vacuum (BA Normal)	30.2% @ 890nm	4.2×10^{12} @ 890, 0V	76
14	Cy7-T	Solution (BA Inverted) transparent	13% @ 850 nm, 0 V 23% @ 850 nm, -2 V	3×10^{12} @ 850, -0.1 V 1×10^{12} @ 850, -2 V	89
15	PMDPP3T:PC61BM	Solution (TA Inverted) Transparent	48% @ 850 nm	1.23×10^{13} @ 850, -0.2 V	80
16	CPDT-alt-Bse	Solution (BA Inverted)	4% @ 900 nm, 0 V	1.04×10^{12} @ 900, 0 V	78
17	ZnPc:C60 CT absorption	Vacuum (TA inverted) Microcavity	23% @ 875 nm, 0 V 18% @ 950 nm, 0 V	2.4×10^{12} @ 950, 0 V	90
18	PBTTT:PCBM CT absorption	Solution (TA inverted) Microcavity	23% @ 960 nm, 0 V	8×10^{12} @ 960, 0 V	79
19	PDPP3T: PC70BM with DIO	Solution (BA Normal)	35% @ 900 nm, -5 V 25% @ 900 nm, 0 V	3.34×10^{12} @ 900, -5 V	72
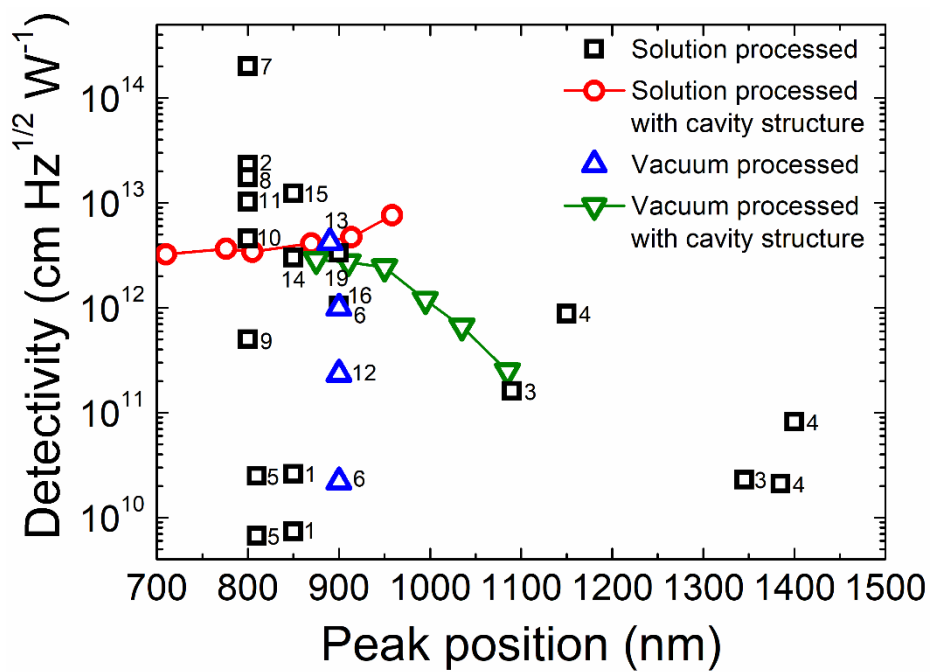
Figure 1.6 Summary for previous reports on near-infrared organic photodetectors.

circuit, because bottom thin-film transistors (TFTs) reduce the aperture ratio and hinder OPD light absorption.[91–94] Instead, a transparent top electrode, i.e., a top-absorbing OPD, is necessary. Despite the research on a bottom hole-collection integrated on Si readout circuitry[95], a bottom electron-collecting electrode is preferred because oxide TFTs having high carrier mobility, a low processing cost and temperature, and film uniformity are basically n-type. Thus, to apply an OPD to an integrated circuit, the OPD should have the following inverted structure: a bottom cathode, an electron extraction layer, a photoactive layer, a hole extraction layer, and a transparent top anode.

Lead phthalocyanine (PbPc) is a good candidate for NIR-absorbing materials. In the monoclinic or amorphous phase, PbPc molecules absorb red light near 740 nm. In contrast, PbPc molecules in a triclinic crystal structure absorb NIR light near 900 nm rather than red light due to alternative molecular packing induced intermolecular interaction[28,96,97]. Therefore, triclinic phase formation is desired to increases the photo-response in the NIR wavelength regime with high-efficiency. Various methods have been developed to form the triclinic phase; the use of a templating layer such as pentacene[36], oxovanadium phthalocyanine (VOPc)[37], sexithiophene (6T)[37], zinc phthalocyanine (ZnPc)[19], copper bromide (CuBr)[38], or copper iodide (CuI)[18], controlling the deposition rate[24,28] or substrate temperature[39,40], or post-thermal annealing of the deposited film[24,32]. In our previous work, we demonstrated the OPDs with oriented PbPc molecules resulting in enhanced responsivity of 35.8 mA/W. However, PbPc loses crystallinity in a blended layer, which is required for bulk-heterojunction
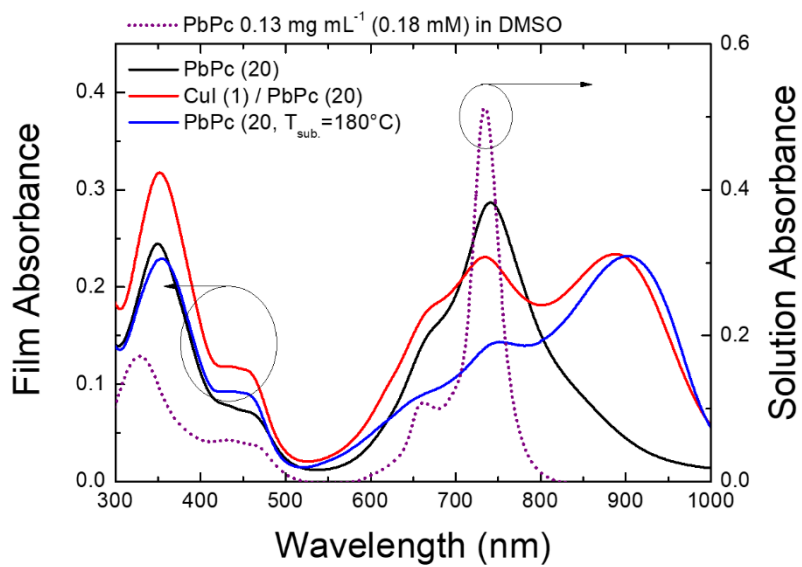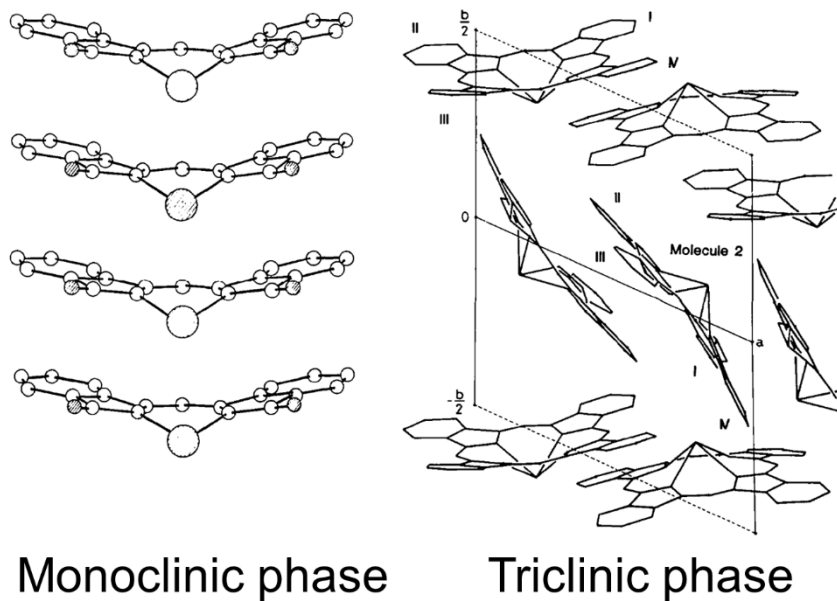
Figure 1.7 Molecular packing structure of PbPc in monoclinic and triclinic phases and absorption spectra of PbPc in various conditions.

(BHJ) structures, resulting in weak NIR absorption in blend films. Several studies have examined the OPV/BHJ combination using PbPc and an acceptor material[98,99]; however, there have been few studies on NIR OPDs.

Chapter 2. Enhancement of fill factor through increase of crystallinity in fullerene based small molecule organic photovoltaic cells

2.1 Introduction

In this study, we report that the crystallinity of C_{70} is improved significantly if CuI is used as the templating layer, leading to remarkable enhancement of hole mobilities in the layers. The grazing-incident X-ray diffraction (GIXRD) patterns show significant enhancement of the crystallinity of a (111)-oriented FCC phase of C_{70} when CuI is inserted as the templating layer on an indium-tin oxide (ITO) substrate. The use of the templating layer also causes an increase of the hole mobility from 8.32×10^{-6} to 3.26×10^{-5} cm^2 V^{-1} s^{-1}. As a result, the use of the templating layer in C_{70}-based solar cells with low donor concentration resulted in a significant improvement of the FF from 0.51 to 0.57 and the PCE from 5.56% to 6.23% under simulated AM 1.5G, 1 sun irradiation.

2.2 Experimental

The ITO-coated glass substrates were cleaned with acetone and isopropyl alcohol and exposed to UV-O_3 for 10 min before use. ReO_3 and CuI were used as interfacial layers and deposited using thermal evaporation onto the substrate at a base pressure of ca. 10^{-7} Torr with a rate of 0.1 Å/s. TAPC and C_{70} were also deposited using thermal evaporation onto the substrate with different rates of 0.1 and 1.9 Å/s in order to form a 5% TAPC-doped C_{70} layer. The exciton blocking layer, bathocuproine (BCP), and aluminum metal cathode were deposited with rates of 1.0 and 4.0 Å/s, respectively. All of the layers were successively evaporated without breaking the vacuum, and all devices were encapsulated in N_2 ambient before photocurrent measurements. The photovoltaic properties of the devices were measured with an AM 1.5G 100 mW/cm^2 solar simulator (300 W Oriel 69911A) light source and a source measurement unit (Keithley 237). The measurement setup was calibrated with a National Renewable Energy Laboratory certified reference silicon solar cell covered with a KG-5 filter before measurement. More than six devices with the cell area of 2×2 mm^2 were averaged to calculate the cell performance. The crystalline structures were investigated by synchrotron X-ray diffraction measurements at the 5A X-ray scattering beamline for materials science at Pohang Light Source II (PLS-II). The X-ray wavelength was 1.072 Å (11.57 keV) at an incident angle of 0.2°.

2.3 Result and discussion

Figure 2.1a shows the GIXRD patterns of the C_{70} films with and without CuI templating layer. The diffraction pattern of C_{70} on Si substrate shows three peaks, which can be assigned as the (111)-oriented ($Q = 7.4$ nm^{-1}), the (220)-oriented ($Q = 12.0$ nm^{-1}), the (311)-oriented ($Q = 14.2$ nm^{-1}) FCC phases of the C_{70}, respectively.[100]. The integrated areas of the peaks are 423, 19 and 96, respectively, and the ratio of the (111)-oriented FCC phase is only 0.64. In contrast, the diffraction pattern of C_{70} with CuI templating layer shows enhanced orientation whit the peaks which can be assigned as the (111)-oriented, the (220)-oriented, the (311)-oriented, and the (222)-oriented ($Q = 15.0$ nm^{-1}) FCC phases of the C_{70} and braod peak which can be assigned as the (101)-oriented HCP phase of C_{70} originating from the stacking fault of the (111)-oriented FCC phase of C_{70}.[101] The ratio of (111)-oriented FCC phase (including the (101)-oriented HCP and the (222)-oriented FCC pahse) is 0.96. The grain size of the (111)-oriented FCC phase aslo increased from 10.8 nm to 17.5 nm. Here, the reason for templating effect is not clear yet, however, possible reason is interaction between fullerene and iodide in CuI. When I_2 molecules diffuse into fullerene crystal, new bonding is observed in raman spectroscopy[102]. In this case, I_2 molecules locate between FCC(111) planes.[103]

Figure 2.1b shows the GIXRD patterns of the C_{70} films doped with 5% TAPC (active layers). The organic films are deposited on the ITO substrate covered with a 1-nm-thick ReO_3 layer for GIXRD samples because active
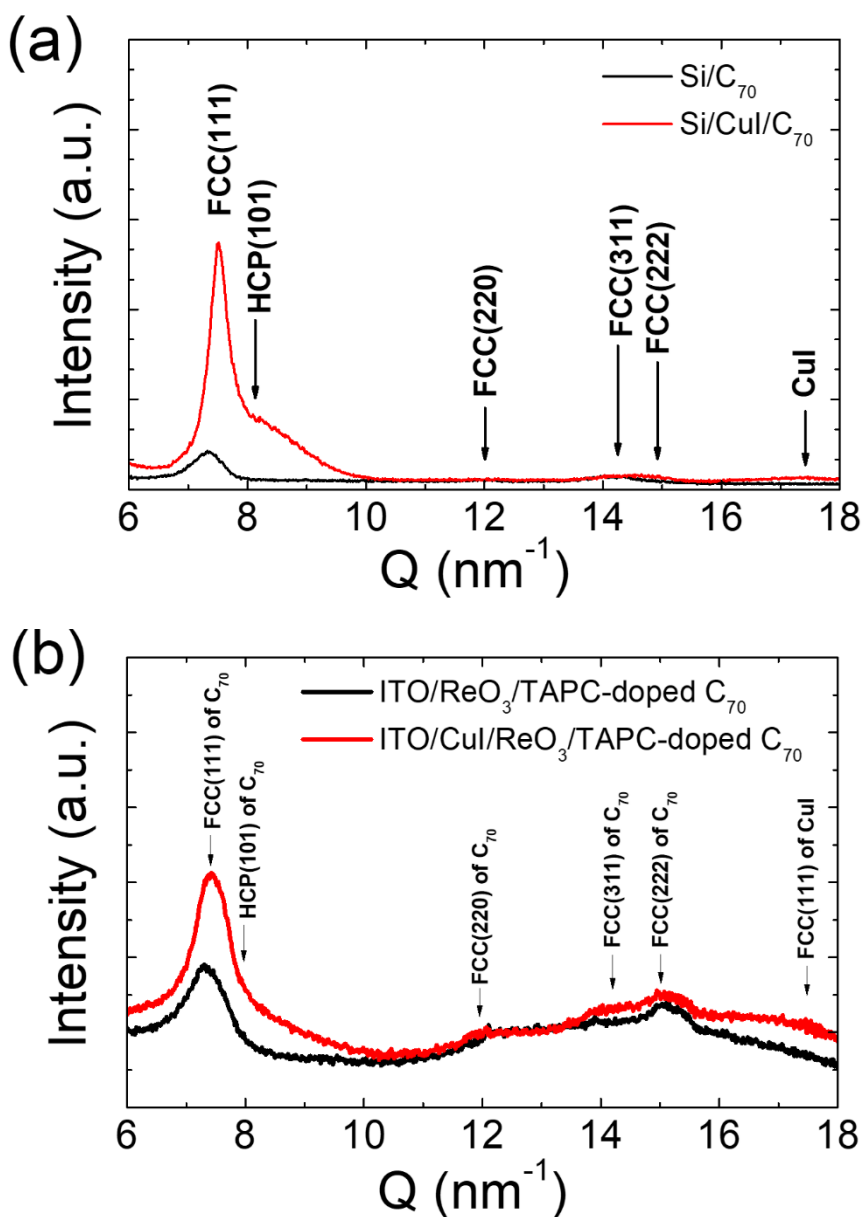
Figure 2.1 GIXRD patterns of organic flms. Film structures are Si / with and without CuI (3 nm) / C_{70} (50 nm) for image (a) and ITO (150 nm) / ReO_3 (1 nm) / with and without CuI (1 nm) / 5% TAPC-doped C_{70} (50 nm) for image (b). An incident angle incident angle was 0.2°.

layers of the solar cells are grown on the substrate. The diffraction pattern of the 50-nm thick C_{70} film doped with 5% TAPC shows four peaks, which can be assigned as the (111)-oriented, the (220)-oriented, the (311)-oriented, and the (222)-oriented FCC phases of the C_{70}, respectively.[100] The (111) and (222) peaks have high peak intensities compared to other peaks. When the 5% TAPC-doped C_{70} film is grown on the 1-nm-thick CuI deposited on a ReO_3/ITO substrate, the intensity of the (111) peak is remarkably increased compared to the film grown on ReO_3, indicating that the crystallinity increases significantly with CuI. The pattern also shows a shoulder at $Q = 8$ nm^{-1} and peak near 17.5 nm^{-1} (the (111)-oriented FCC phase of CuI[104]) which is not shown from the sample without CuI. The shoulder can be assigned as the (101)-oriented HCP phase of C_{70} originating from the stacking fault of the (111)-oriented FCC phase of C_{70}.[101] The peak of the stacking fault is very broad compared to other peaks because of the anisotropic property of C_{70}.[105] Including the stacking fault, the crystallinity of the FCC phase was increased remarkably, especially the (111)-oriented FCC phase. The results clearly indicate that the templating layer significantly improves the crystallinity of the C_{70} film doped with 5% TAPC on the ITO substrate. Interestingly enough, the morphology did not change much eventhough the crystallinity in the grains increased significantly by introducing the CuI layer (Figure 2.2).

Hole mobilities in the active layer were extracted from the current density-voltage (J-V) curves of hole-only devices in the space-charge-limited current (SCLC; Figure 2.3a). The device structures are ITO (150 nm)/ReO_3 (1 nm)/with
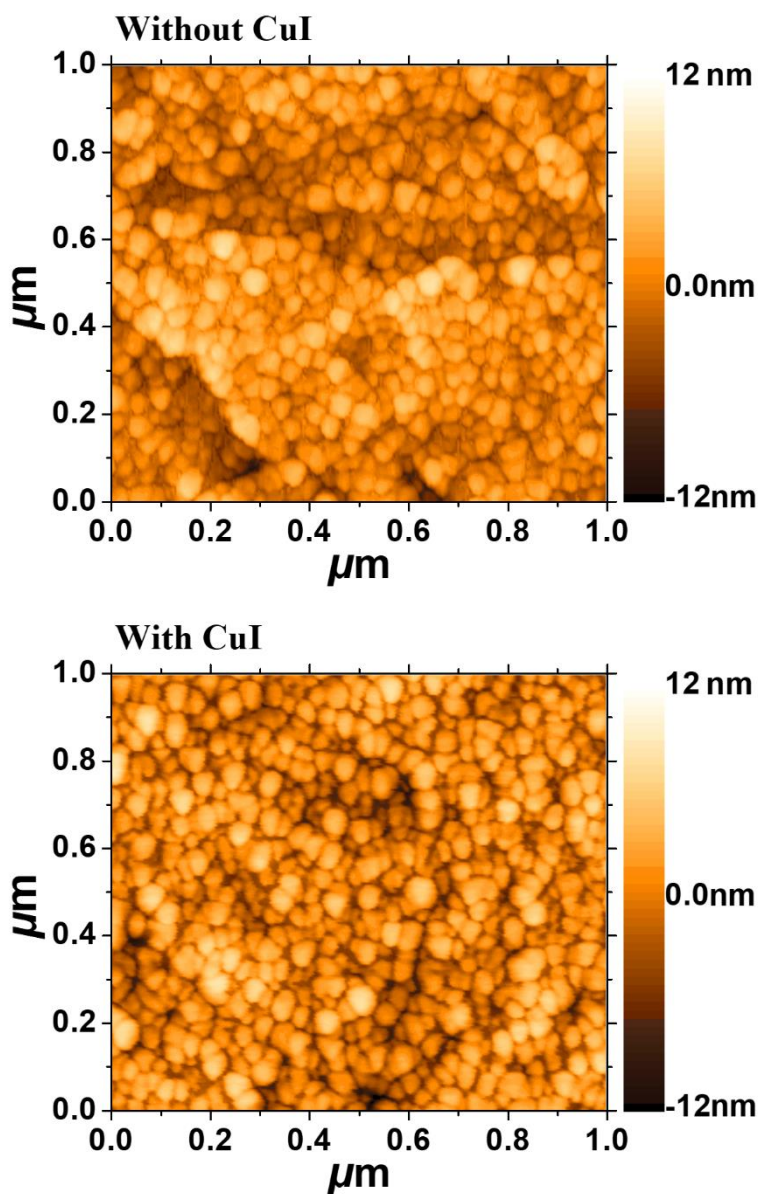
Figure 2.2 AFM images of the 50 nm thick 5% TAPC-doped C_{70} film grown on ITO/ReO$_3$(1 nm) and ITO/ReO$_3$(1 nm)/CuI(1 nm). The size of image is 1 μm×1 μm.

or without CuI (1 nm)/5% TAPC-doped C_{70} (500 nm)/ReO$_3$ (5 nm)/Al (100 nm). The ReO$_3$ layers were used in the devices to form an ohmic contact for hole injection at the anode side and to block electron injection at the cathode side. The built-in potential in the device was expected to be negligible because of the ReO$_3$ layers. In contrast, the built-in potential in the active layer cannot be negligible when the 1-nm-thick CuI layer was inserted between ReO$_3$ and the active layer because CuI has a different work function from ReO$_3$, leading to modification of the energy level alignment. The built-in potential of the device with the CuI layer was estimated from the difference of the built-in potentials of the devices of ITO (150 nm)/ReO$_3$ (1 nm)/with or without CuI (1 nm)/C_{70} (60 nm)/BCP (8 nm)/Al (100 nm). The built-in potentials of the devices with and without the CuI layer were calculated as 0.986 and 0.763, respectively, from analysis of the capacitance-voltage characteristics using the Mott-Schottky relationship shown in Figure 2.3b.[106,107] On the basis of measurements, the hole-only device with the CuI layer was assumed to have a built-in potential of -0.22 V. With consideration of the built-in field, hole mobilities in the active layer from SCLC fitting increased from 8.32×10^{-6} to 3.26×10^{-5} cm^2 V^{-1} s^{-1} when the 1 nm thick CuI layer was inserted between ReO$_3$ and the active layer. The increased hole mobility was consistent with enhancement in the crystallinity of the TAPC-doped C_{70} film when deposited on CuI. The electron mobility also increased from 3.4×10^{-5} to 5.3×10^{-5} cm^2 V^{-1} s^{-1} upon insertion of the CuI layer, which was measured by the time-of-flight method using the structures of ITO (150 nm)/with or without CuI (1 nm)/5% TAPC-doped C_{70}
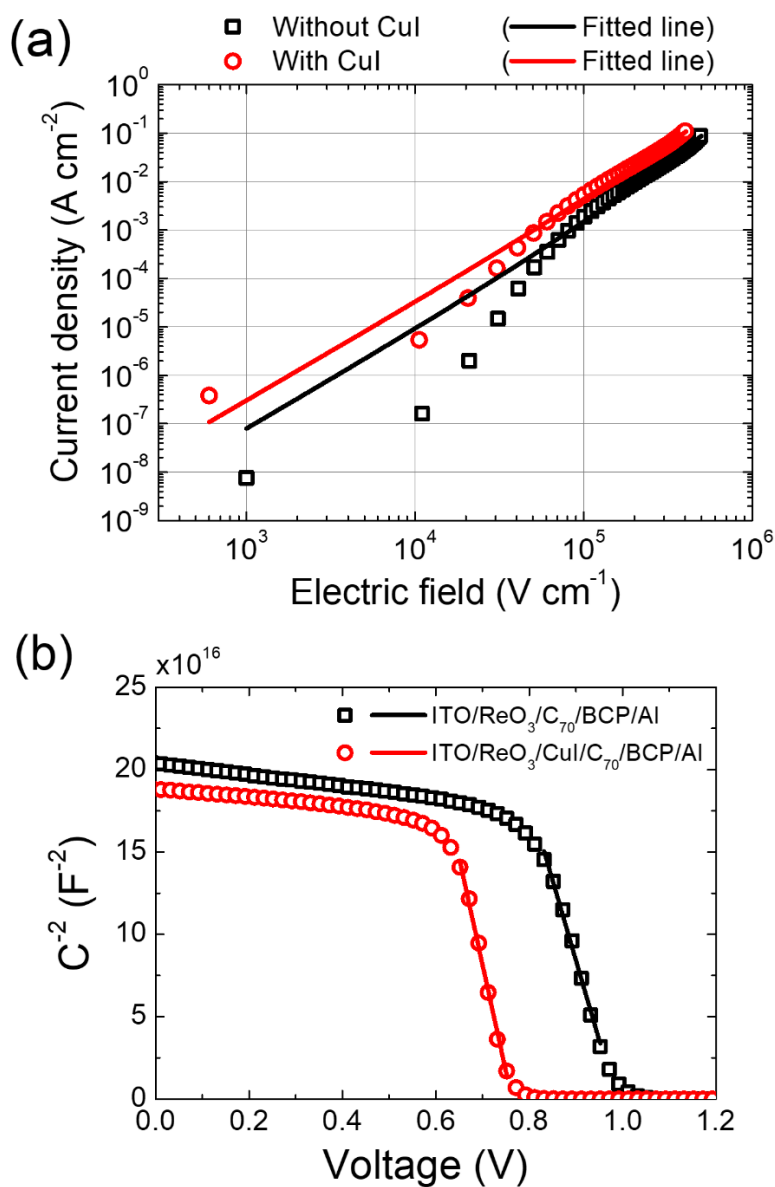
Figure 2.3 (a) Current densities against the applied voltage for hole only devices of 5% TAPC-doped C_{70} film to extract hole mobilities. Device structures are ITO (150 nm)/ReO$_3$ (1 nm)/with or without CuI (1 nm)/5% TAPC-doped C_{70} (500 nm)/ReO$_3$ (5 nm)/Al (100 nm). The open symbols are experimental J-V characteristics for the single carrier devices, while the solid lines are fits using the SCLC model. (b) Capacitance-voltage characteristics of Schottky solar cells. Solid lines represent Mott-Schottky plot.
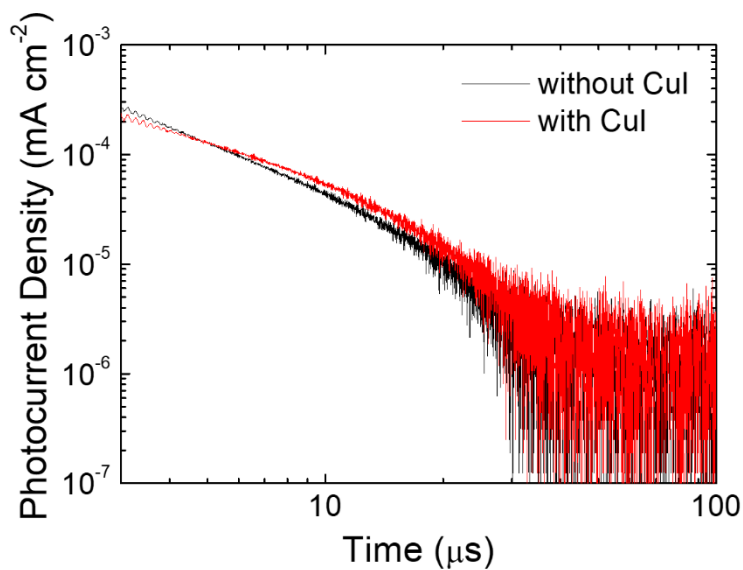
Figure 2.4 Transient photocurrent profiles measured at 298 K and for an electric field of 2×10^5 V/cm. The device structures are: ITO (150 nm)/ with or without CuI (1 nm)/5% TAPC doped C_{70} (1000 nm)/Al (100 nm). The electron mobility increases with the introduction of CuI layer from 3.35×10^{-5} cm^2 V^{-1} s^{-1} to 5.29×10^{-5} cm^2 V^{-1} s^{-1}.

(1000 nm)/Al (100 nm) shown in Figure 2.4.

Figure 2.5a shows the J-V characteristics of the OPV cells with the structure of ITO (150 nm)/ReO$_3$ (1 nm)/with or without CuI (1 nm)/5% TAPC-doped C$_{70}$ (60 nm)/BCP (8 nm)/Al (100 nm) in the dark and under illumination of an AM 1.5G 100 mW/cm^2 solar simulated light source. Table 2.1 summarizes the solar cell performance of J$_{SC}$, V$_{OC}$, FF, PCE, and the series resistance (R$_S$) obtained by fitting the dark J-V curves with the Shockley diode equation. The OPV cells show the same V$_{OC}$ value of 0.91 V, because it was determined by the HOMO of TAPC and the lowest unoccupied molecular orbital (LUMO) of C$_{70}$. J$_{SC}$ of two devices also show the same value of 12.0 mA/cm^2 with the same absorption spectra (shown in Figure 2.6). This value is close to the calculated photocurrent using the transfer matrix method and the refractive indices measured by variable-angle ellipsometry, as shown in Figure 2.7. The very good match between the experimental and calculated J$_{SC}$ values indicates that the 1-nm-thick ReO$_3$ layer acts as an efficient hole extraction layer because of its high work function, leading to a large built-in field distributed in the device at shortcircuit conditions. In contrast, FF increases from 51.2% to 57.1% by insertion of the CuI templating layer. It can be understood based on the electron and hole mobilities. In spite of the high electron mobility of the film, a low hole mobility of the film results in an accumulation of hole carriers in the film, leading to bimolecular recombination and reduced FF. However, the use of the CuI layer enhances the hole mobility, improves hole extraction, and reduces bimolecular recombination in the device, leading to an increase of the FF and

36

PCE of the solar cells with low donor concentration.

The incident photon-to-electron conversion efficiencies (IPCEs) of the OPVs with and without the CuI templating layer are shown in Figure 2.5b. The IPCE of the device with CuI is slightly higher than that of the device without CuI in the range from 480 to 700 nm. This is due to enhanced charge extraction caused by an increase in the hole mobility. The IPCE data were used to calculate J_{SC} using the AM 1.5G solar spectrum, and the calculated J_{SC} values of the OPV cells with and without CuI layer were 11.7 and 11.5 mA/cm^2, resulting in the corrected PCEs of 6.10% and 5.36%.
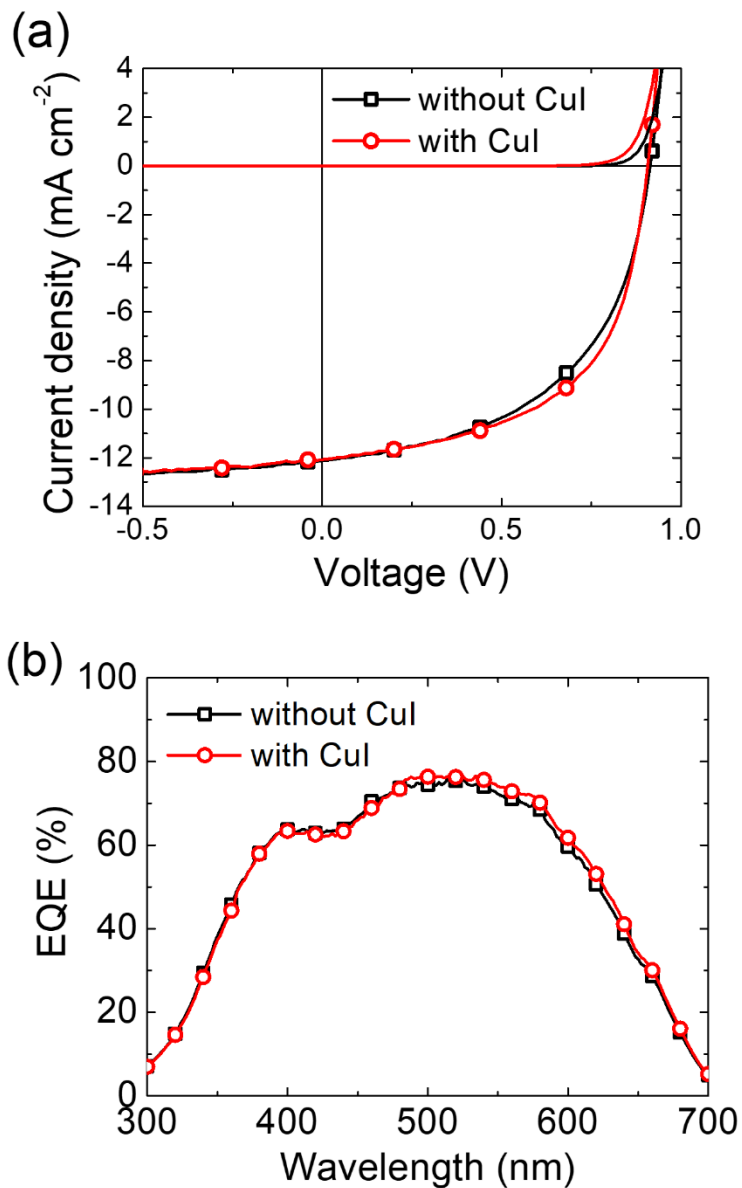
Figure 2.5 (a) The J-V characteristics with and without the CuI templating layer under AM 1.5G illumination. The device structures are ITO/ReO$_3$ (1 nm)/with or without CuI (1 nm)/5% TAPC-doped C$_{70}$ (60 nm)/BCP (8 nm)/Al (100 nm). (b) The IPCE data for the devices.

Table 2.1 The solar cell performance with and without the CuI templating layer. Series resistance (R_S), ideality factor (n) and dark saturation current density (J_S) are obtained by fitting the dark J-V curve with the Shockley diode equation.

	PCE (%)	J_{SC} (mA/cm^2)	V_{OC} (V)	FF (%)	R_S (Ω cm^2)	n	J_S (mA/cm^2)
without CuI	5.59±0.33	12.0±0.2	0.91±0.01	51.2±2.5	2.17	1.51	6.59×10^{-11}
with CuI	6.23±0.04	12.0±0.2	0.91±0.02	57.1±0.8	2.08	1.47	5.51×10^{-11}
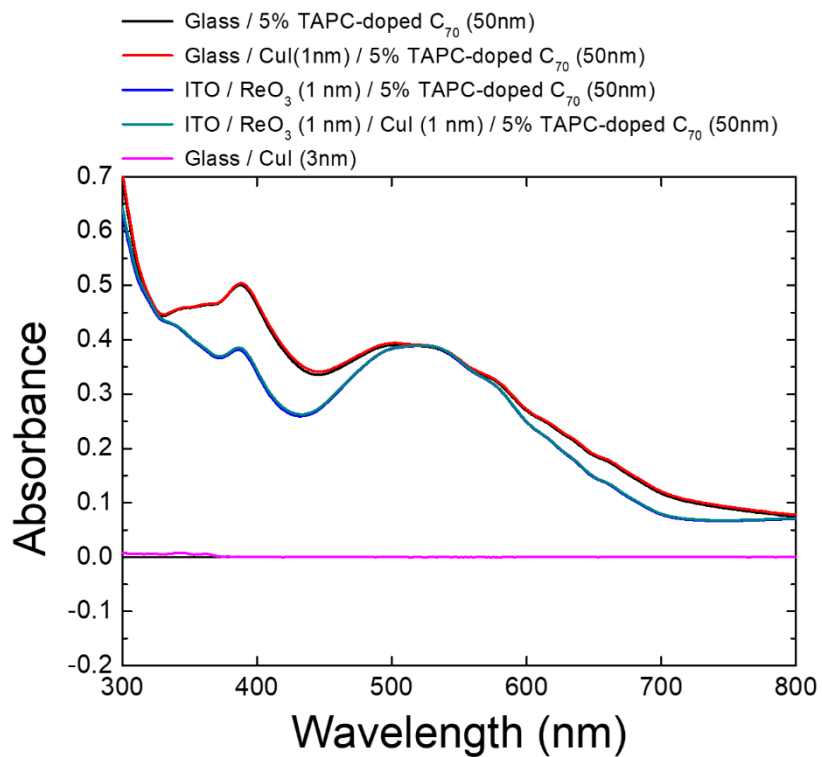
Figure 2.6 Absorption spectra of organic films. It is shown that optical properties of fullerene films remain with inserting CuI templating layer.
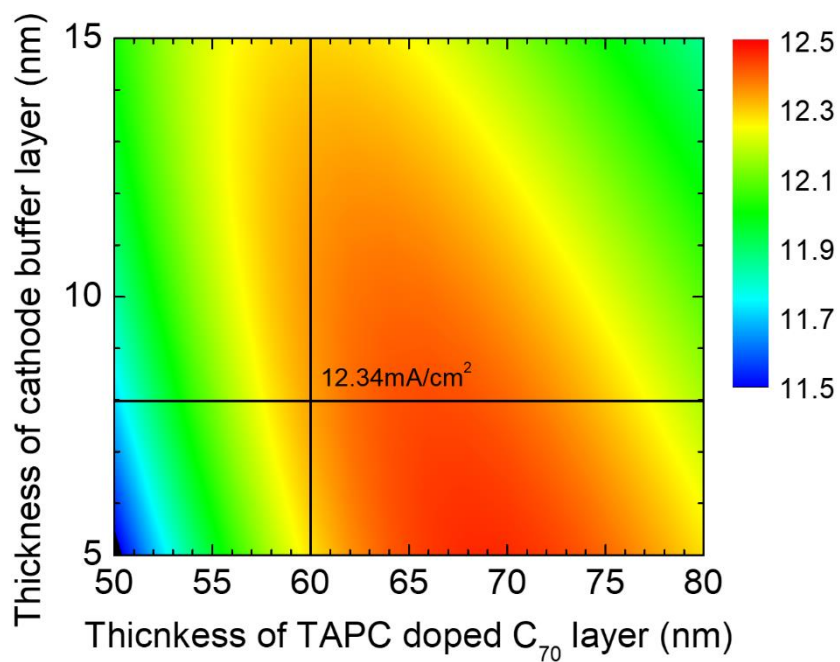
Figure 2.7 Calculated J_{SC} of ITO/5% TAPC-doped C_{70}/BCP (cathode buffer layer)/Al (100 nm) by transfer matrix method. The 1 nm thick hole extraction layer can be negligible because the calculated J_{SC} with and without 1 nm thick ReO$_3$ are 12.61 mA/cm^2 and 12.34 mA/cm^2 respectively and an error is less than 2%.

2.4 Conclusion

The use of CuI as the templating layer in a C_{70}-based low-donor-concentration organic solar cell improves the FF significantly from 0.51 to 0.57 without any change in J_{SC} and V_{OC} to increase the PCE from 5.59% to 6.23%. It turned out that the improvement comes from the increased crystallinity of C_{70} in the active layer and from an increase in the hole mobility to get better charge extraction and less electron-hole recombination in the active layer. This result clearly demonstrates that not only the crystallinity of the donor materials but also the crystallinity of fullerene derivatives is important in organic solar cells especially in low-donorconcentration organic solar cells, and the use of CuI as a templating layer is effective to increase the crystallinity of fullerene derivatives as well as the donor materials.

Chapter 3. Inverted near-infrared organic photodetector with oriented lead (II) phthalocyanine molecules via substrate heating

3.1 Introduction

Here, we develop inverted OPDs exhibiting enhanced responsivities in the NIR region by heating the substrate during deposition of PbPc. PbPc molecules deposited onto a C_{60} layer at room temperature form the monoclinic phase, but if the substrate is heated the triclinic phase is formed. Using 1,4,5,8,9,11-hexaazatriphenylenehexacarbonitrile (HATCN), a buffer protecting the organic layer during sputtering[64], OPDs prepared on heated substrates exhibited a responsivity of 35.8 mA/W at 960 nm, whereas the figure for OPDs prepared without substrate heating was 8.4 mA/W. The external quantum efficiency (EQE) also increased from 0.9 to 4.4% with substrate heating.

3.2 Experimental

The inverted OPDs have the following structure: Glass/Cr (10 nm)/Ag (200 nm)/C_{60} (60 nm)/PbPc (60 nm)/HATCN (50 nm)/IZO (150 nm). The glass substrate was successively cleaned with detergent solution, acetone, and isopropyl alcohol to remove particles and organic materials. A 10-nm-thick Cr layer was used as an adhesion layer for the Ag bottom electrode and was deposited onto the glass substrate, via thermal evaporation, at a rate of 0.1 Å/s. A 200-nm-thick Ag bottom electrode was also deposited using thermal evaporation, at a rate of 0.5 Å/s. C_{60} served as the acceptor material and was deposited via thermal evaporation onto the Ag bottom electrode at a rate of 0.5 Å/s. PbPc served as the donor material absorbing NIR light and was deposited at 0.2 Å/s, both with and without substrate heating. The substrate was heated to 180°C. HATCN served not only as a hole-extraction layer but also as a buffer protecting the organic layers during formation of the IZO top electrode via sputtering.[64] The HATCN deposition rate was 0.2 Å/s. All the metal and organic layers were deposited at a base pressure $< 5 \times 10^{-7}$ Torr, and the substrate was then transferred through a load-lock to another chamber, where the IZO top electrode was formed on top of the HATCN layer using a sputtering process under a gas flow rate of 30 standard cubic centimeters per minute (sccm) for Ar and 0.6 sccm for O_2, and a working pressure of 2.7 mTorr. The active area was 2×2 mm^2, as delimited by the Ag bottom and IZO top electrodes. After fabrication, the devices were encapsulated in an N_2 atmosphere prior to measurements. Ultraviolet-visible (UV-Vis) absorbance spectra were recorded

by a VARIAN Cary 5000 UV-Vis spectrophotometer. Current density-voltage characteristics were measured under an AM 1.5G solar simulator (Oriel), or in the dark and recorded using a Keithley 237 source measurement unit. Before measurement, the light intensity was calibrated with the aid of a National Renewable Energy Laboratory-certified reference silicon solar cell fitted with a KG-5 filter. The EQE was measured using a 1,000-W Xe lamp (Oriel) combined with a calibrated monochromator (Acton Research). The intensity of monochromatic light was calibrated with the aid of a silicon photodiode (Newport). Crystalline structure was explored via synchrotron X-ray diffraction at the 5A X-ray scattering beamline for materials science (the Pohang Light Source II; PLS-II). The X-ray wavelength was 1.072 Å (11.57 keV) at an incident angle of 0.15°.

3.3 Results and Discussion

Figure 3.1 compares the absorbance spectra of organic films deposited on glass substrates with and without substrate heating. The films had the following structure: Glass/C_{60} (60 nm)/PbPc (60 nm)/HATCN (50 nm), i.e., the same as the device structure without the bottom and top electrodes. Both samples exhibited NIR absorption with two peaks at wavelengths near 700 and 900 nm. However, the film deposited with substrate heating exhibited higher absorption in the NIR, and lower absorption in the red. Thus, the proportion of the monoclinic phase (absorption peak at 740 nm) decreased, and that of the triclinic phase (absorption peak at 900 nm) increased, when the PbPc film was deposited with substrate heating. In addition, heating shifted the NIR absorption peak from 900 nm to 920 nm.

Figures 3.2a and 3.2b show the EQE and responsivity spectra of NIR OPDs fabricated without and with substrate heating. The substrate heating generated the absorption peak near 960 nm attributable to triclinic absorption. These were lacking when heating was omitted. The EQE and responsivity for triclinic phase (960 nm) is red-shifted by 40 nm compared to the absorption of thin films (920 nm) due to cavity effect as described in Figure 3.3. Notably, an absorption peak at 900−1,000 nm was observed in the film fabricated without heating (black line in Figure 3.1), but not in the EQE or responsivity spectrum (black lines in Figure 3.2). The differences are attributable to different initial growth modes of the PbPc layer with and without substrate heating. When PbPc
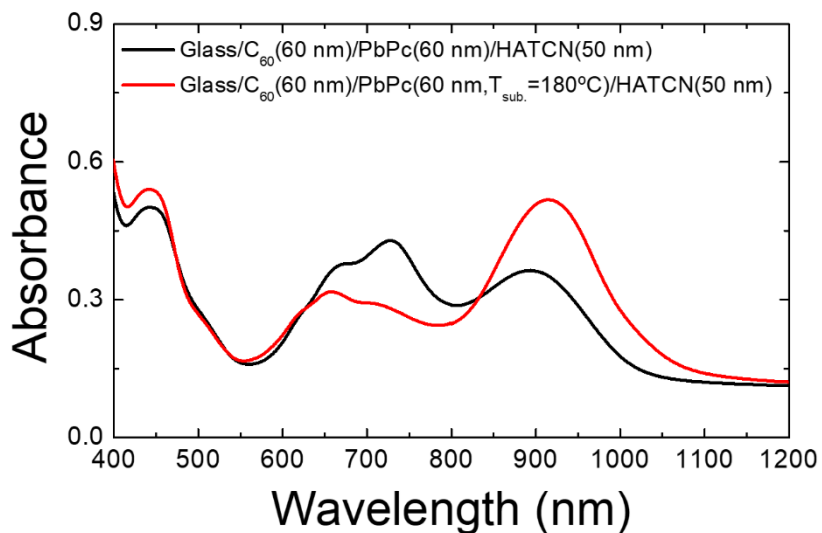
Figure 3.1 Near-infrared (NIR) absorbance spectra of organic films of inverted organic photodetectors (OPDs) on a glass substrate. The film structures were Glass / C_{60} (60 nm) / lead (II) phthalocyanine (PbPc; 60 nm) / 1,4,5,8,9,11-hexaazatriphenylenehexacarbonitrile (HATCN; 50 nm) (black line) and Glass / C_{60} (60 nm) / PbPc (60 nm, with substrate heating) / HATCN (50 nm) (red line).
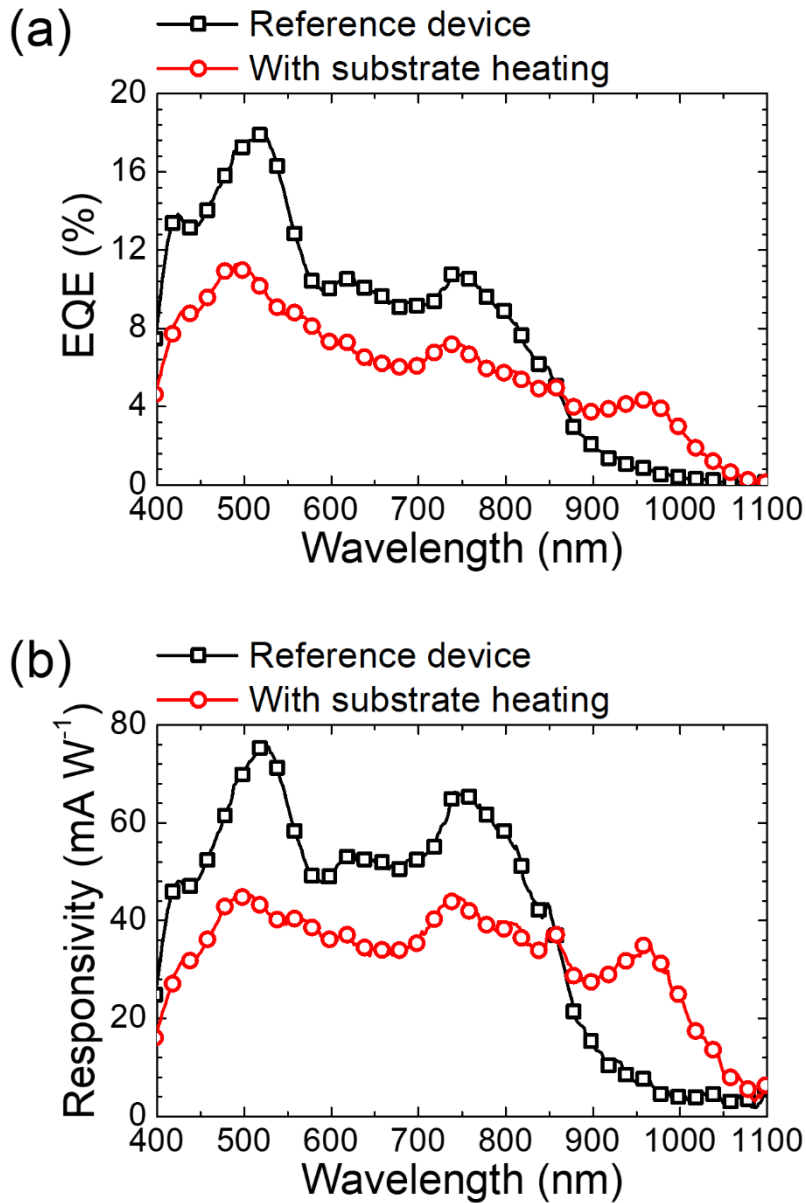
Figure 3.2 (a) External quantum efficiency (EQE) spectra and (b) the responsivity spectra of the NIR OPDs. Black: no substrate heating; red: substrate heating. The device structures were Ag (200 nm) / C_{60} (60 nm) / PbPc (60 nm, with and without substrate heating) / HATCN (50 nm) / IZO (150 nm).

is deposited onto an ITO or glass substrate at room temperature, the monoclinic phase is initially formed and the crystal structure changes to triclinic as the thickness of the PbPc layer increases, enhancing absorption in the red and NIR.[24,28] Thus, PbPc near the C_{60} substrate is monoclinic in the inverted structure grown without heating the substrate. As excitons formed within the diffusion length from the C_{60}/PbPc interface contribute to the photocurrent, the excitons formed in the monoclinic phases located near the interface mostly contribute to the photocurrent, but excitons formed at the triclinic phase located far from the interface do not contribute to the photocurrent when the film was grown at room temperature. However, an absorption peak in the NIR would be expected because the entire PbPc layer contributes to absorption, including the triclinic phase far from the interface. In contrast, the PbPc molecules are in triclinic phase *ab initio* when deposited on a heated C_{60} substrate, creating a spectral response in the NIR.

The initial growth mode of PbPc molecules on C_{60} was further studied by depositing 10-nm-thick PbPc layers with and without substrate heating. We assumed that the exciton diffusion length of the PbPc layer extended 10 nm from the C_{60}/PbPc interface. Figure 3.4a shows the absorbance spectra of the two samples. PbPc film deposited at ambient temperature had an absorption peak at 735 nm and another weak peak at 900 nm, indicating that the monoclinic phase predominated. In contrast, the PbPc layer deposited on the heated substrate exhibited a stronger absorption peak at 920 nm and a weaker peak at 735 nm, confirming that the initial growth mode of the PbPc layer had changed
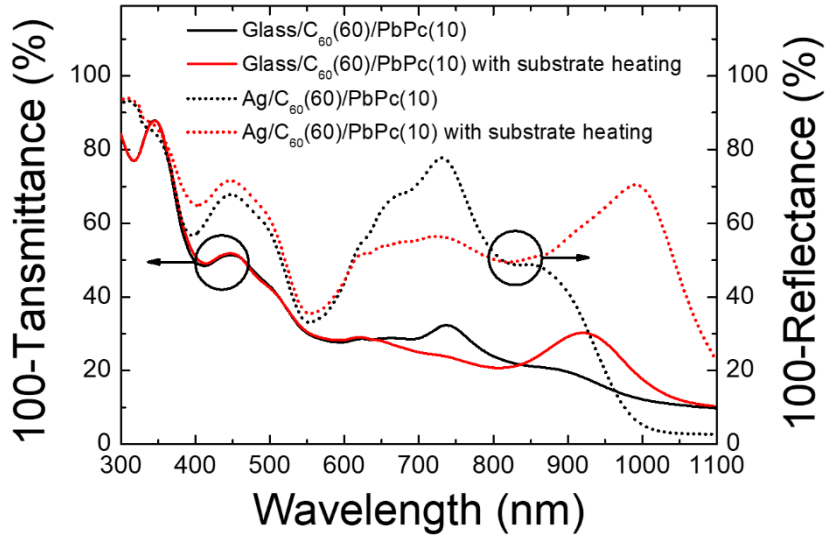
Figure 3.3 The attenuance spectra obtained from transmittance and reflectance. Attenuance from transmittance has peak at 920nm and attenuance from reflectance has peak at 990 nm. This is due to the reflection of Ag and the different refractive index at interfaces, which results in the red-shift of the absorption/EQE peak by cavity effects in the fabricated device.

from the monoclinic to the triclinic phase.

The crystal structure was further studied by grazing incident angle X-ray diffraction (GIXRD) with an incident angle of 0.15°. The four GIXRD patterns (black, red, blue, and green solid lines in Figure 3.4b) are those of Ag (200 nm) / C_{60} (60 nm) and Ag (200 nm) / C_{60} (60 nm) annealed at 180°C for 45 min in a vacuum chamber, Ag (200 nm) / C_{60} (60 nm) / PbPc (10 nm) prepared without substrate heating, and Ag (200 nm) / C_{60} (60 nm) / PbPc (10 nm) prepared with substrate heating, respectively. The black and red lines exhibit three peaks from the C_{60} layer: the (111)-oriented ($Q = 7.69$ nm^{-1}), the (220)-oriented ($Q = 12.55$ nm^{-1}), and the (311)-oriented ($Q = 14.72$ nm^{-1}) FCC phases.[108] As the glass transition temperature of C_{60} is below the ambient temperature, annealing at 180°C did not change the crystal structure of the C_{60} FCC phase.[109] When the PbPc film was present, four additional peaks appeared near $Q = 8.9, 9.2, 11.8,$ and 15.9 nm^{-1}. Using the lattice parameters of the PbPc monoclinic phase[110] (space group = $P2_1/b$, a = b = 2.548 nm, $\gamma = 90°$) and the triclinic phase[111] (space group = $P\bar{1}$, a = 1.313 nm, b = 1.613 nm, c = 1.289 nm, $\alpha = 94.22°$, $\beta = 96.20°$, $\gamma = 114.19°$), the peaks can be assigned as combinations of the monoclinic and triclinic phases. The peak near $Q = 8.9$ nm^{-1} and shoulder near $Q = 9.2$ nm^{-1} were observed in PbPc films deposited without substrate heating, indicating that formation of the (320)-oriented PbPc monoclinic phase ($Q = 8.89$ nm^{-1}) was dominant and the ($1\bar{2}1$)-oriented PbPc triclinic phase ($Q = 9.23$ nm^{-1}) also formed, as shown in figure 3.4a.[28,39,40] The peaks near $Q = 9.2,$

11.8, and 15.9 nm^{-1} were evident in the PbPc film deposited on the heated C_{60} substrate. The peak near Q = 9.2 nm^{-1} is attributable to the $(1\bar{2}1)$-oriented PbPc triclinic phase (Q = 9.23 nm^{-1}). The peak near 11.8 nm^{-1} is a combination of three diffraction peaks: the $(11\bar{2})$-oriented PbPc triclinic phase (Q = 11.70 nm^{-1}), the $(1\bar{3}0)$-oriented PbPc triclinic phase (Q = 11.72 nm^{-1}), and the $(2\bar{2}1)$-oriented PbPc triclinic phase (Q = 11.80 nm^{-1}). The peak near 15.9 nm^{-1} is a combination of two diffraction peaks, the $(3\bar{3}0)$-oriented PbPc triclinic phase (Q = 15.73 nm^{-1}) and the $(1\bar{1}3)$-oriented PbPc triclinic phase (Q = 15.97 nm^{-1}). Thus, GIXRD clearly showed that the initial growth mode was triclinic rather than monoclinic when PbPc molecules were deposited on a heated C_{60} substrate. The GIXRD patterns are consistent with the absorbance spectra of Figure 3.4a.

Figure 3.6 shows cartoons of PbPc films on the C_{60} substrate. Without substrate heating, the PbPc film initially formed the monoclinic phase, followed by the triclinic phase with increasing film thickness. Although NIR absorption by a 60-nm-thick PbPc film grown without substrate heating is evident, the crystal structure within the exciton diffusion length from the C_{60} layer is monoclinic; therefore, excitons generated via NIR absorption cannot reach the donor-acceptor interface. On the other hand, the PbPc film formed with substrate heating forms the triclinic phase on the C_{60} layer; excitons generated by NIR absorption can contribute to the EQE and responsivity in the NIR region.
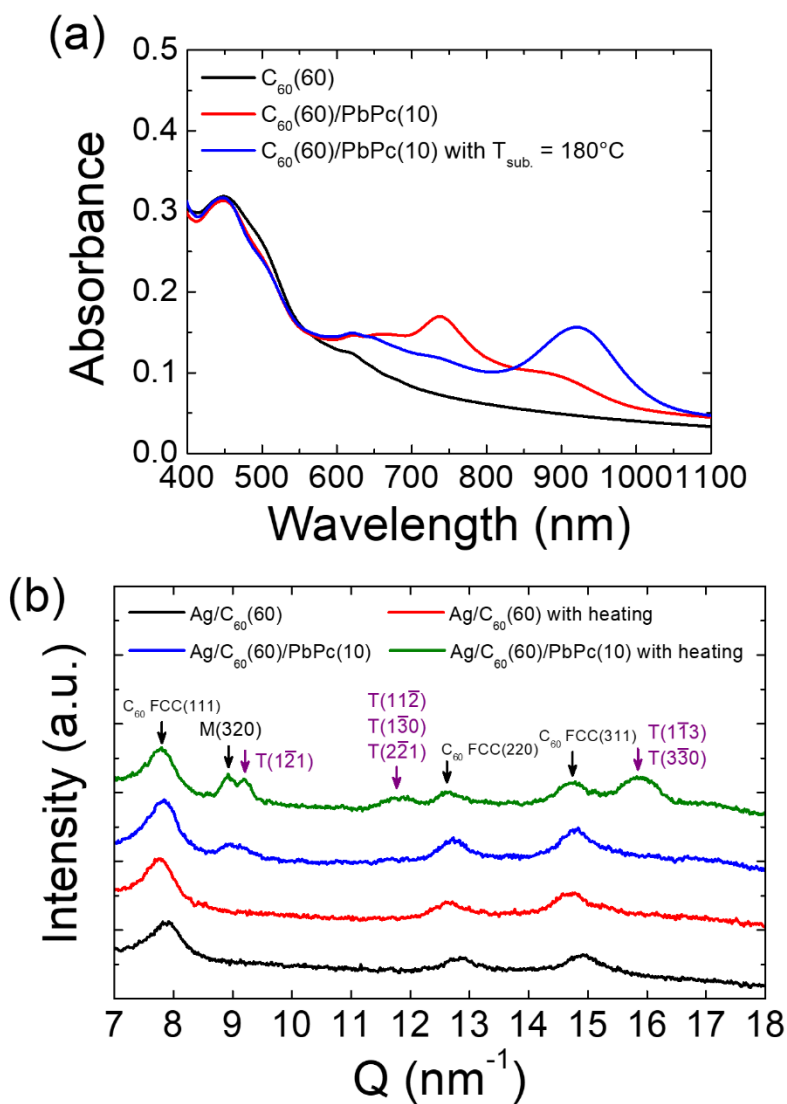
Figure 3.4 Absorbance spectra of 10-nm-thick PbPc films on C_{60} layers. A thin PbPc layer prepared without substrate heating exhibited an absorption peak at 735 nm, whereas a layer prepared with substrate heating exhibited an absorption peak at 920 nm. The peaks at 735 nm and 920 nm indicate formation of the monoclinic and triclinic phase, respectively. (b) Grazing incident angle X-ray diffraction (GIXRD) patterns of organic films. The black, red, blue, and green lines are the GIXRD patterns of Ag/C_{60} (60 nm), Ag/C_{60} (60 nm) with annealing (180°C, 40 min), Ag / C_{60} (60 nm) / PbPc (10 nm), and Ag / C_{60} (60 nm) / PbPc (10 nm) with heating of the substrate (180°C), respectively. The incident angle is 0.15°.
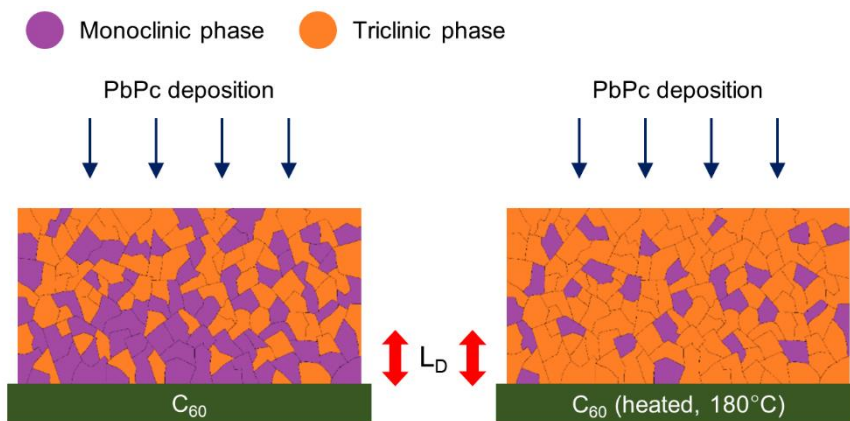
Figure 3.5 Cartoons of PbPc films on C_{60} substrates with and without substrate heating. The violet and orange colors indicate the monoclinic and triclinic phases, respectively. Red arrows: diffusion lengths of photogenerated excitons.

Figure 3.7 compares the dark current and photocurrent densities of the NIR OPDs under AM 1.5G illumination. The photocurrent densities measured under 940 nm light source are also compared in Figure 3.8 The dark current density after substrate heating was higher than that in the absence of heating, attributable to the surface morphology of the PbPc layer deposited during heating. The surface morphology of a Glass / Cr (10 nm) / Ag (200 nm) / C_{60} (60 nm) / PbPc (60 nm) layer, as revealed by atomic force microscopy (AFM), is shown in Figure 3.9a. The film has an R_{rms} of 4.0 nm and an R_{pv} of 40.0 nm when deposited without substrate heating; both were less than the film thickness. However, with substrate heating, the surface morphology changed dramatically (Figure 3.9b); the R_{rms} and R_{pv} values are 18.3 and 181.9 nm, respectively. The high R_{pv} explains the higher dark current density.[112] In addition, the interface between C_{60} and HATCN permits high leakage current flow when substrate heating is employed. Although the thickness of the PbPc layer is only 60 nm, the valley depth is 58.4 nm; contacts between C_{60} and HATCN are thus possible. To understand the effect of this interface, we fabricated devices without PbPc: Glass / Cr (10 nm) / Ag (200 nm) / C_{60} (60 nm) / HATCN (50 nm) / IZO (150 nm). The dark current density of the device without PbPc is shown in Figure 3.10. No diode characteristics are evident, indicating that formation of an interface between C_{60} and HATCN increased the dark current density in the reverse bias region. The open-circuit voltage (V_{OC}) of the device prepared with substrate heating was also reduced. The reduction of V_{OC} is discussed below using the Shockley diode equation:

$$V_{oc} = \frac{nkT}{q} \ln\left(\frac{J_{sc}}{J_s}\right) \qquad (3.1)$$

where n is the ideality factor, k is the Boltzmann constant, T is the temperature, q is the elementary charge, J_{SC} is the short-circuit current density, and J_S is the dark saturation current density. The diode parameters are extracted from the dark current density-voltage curves using the above equation and summarized in Table 3.1.[113] With substrate heating, J_S and n change from 2.81×10^{-9} to 6.66×10^{-6} mA/cm^2 and from 1.81 to 1.79, respectively. The V_{OC} values calculated using equation (1) are 0.533 V for the device without substrate heating and 0.330 V for that with substrate heating. Such reduction in the calculated V_{OC} is consistent with the change in measured V_{OC}. It would be very useful to reduce roughness without sacrificing responsivity in the 900−1,000 nm region.
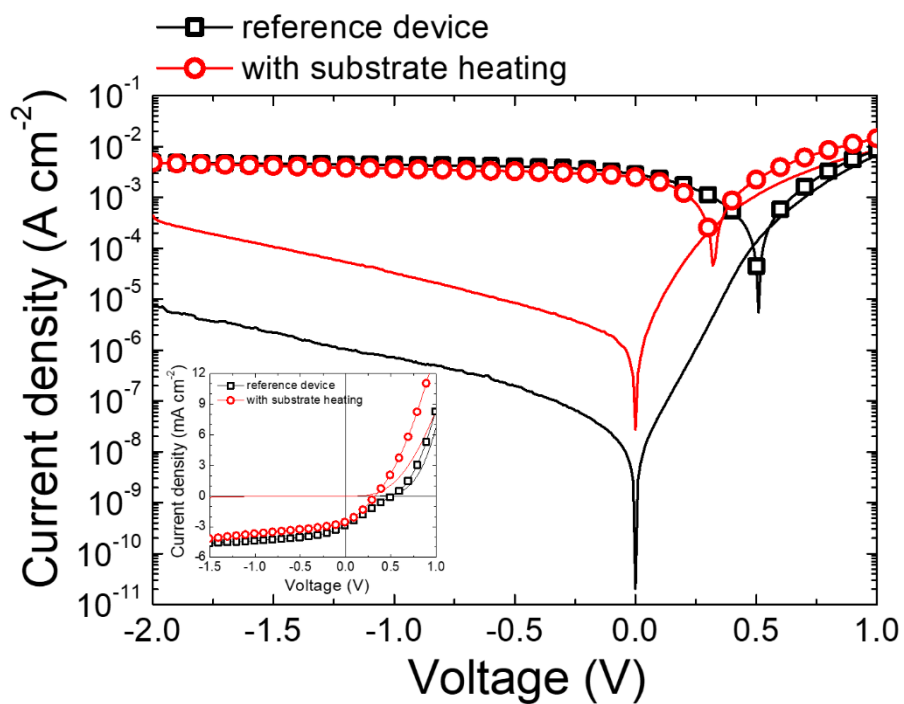
Figure 3.6 The dark current densities of NIR OPDs and photocurrent densities under AM 1.5G illumination. Black: no substrate heating; red: with substrate heating. The device structures are Ag (200 nm) / C_{60} (60 nm) / PbPc (60 nm, with and without substrate heating) / HATCN (50 nm) / IZO (150). The insert shows the linear nature of the current-voltage (J-V) curves.
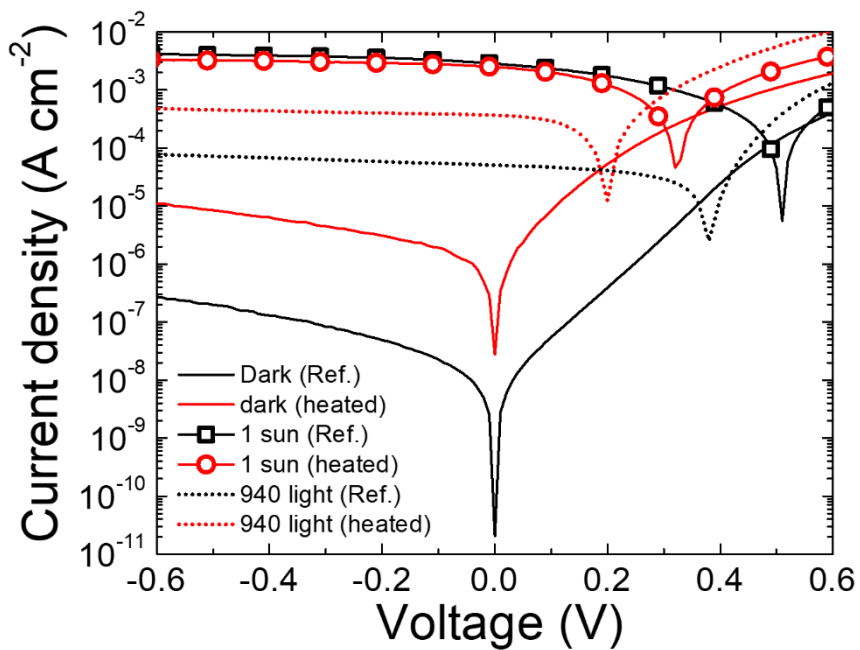
Figure 3.7 The dark current densities and photocurrent densities under AM 1.5G illumination and 940 nm illumination (5.5 mW/cm^2) of the NIR OPDs. Black: no substrate heating; red: with substrate heating. The device structures are Ag (200 nm) / C$_{60}$ (60 nm) / PbPc (60 nm, with and without substrate heating) / HATCN (50 nm) / IZO (150).
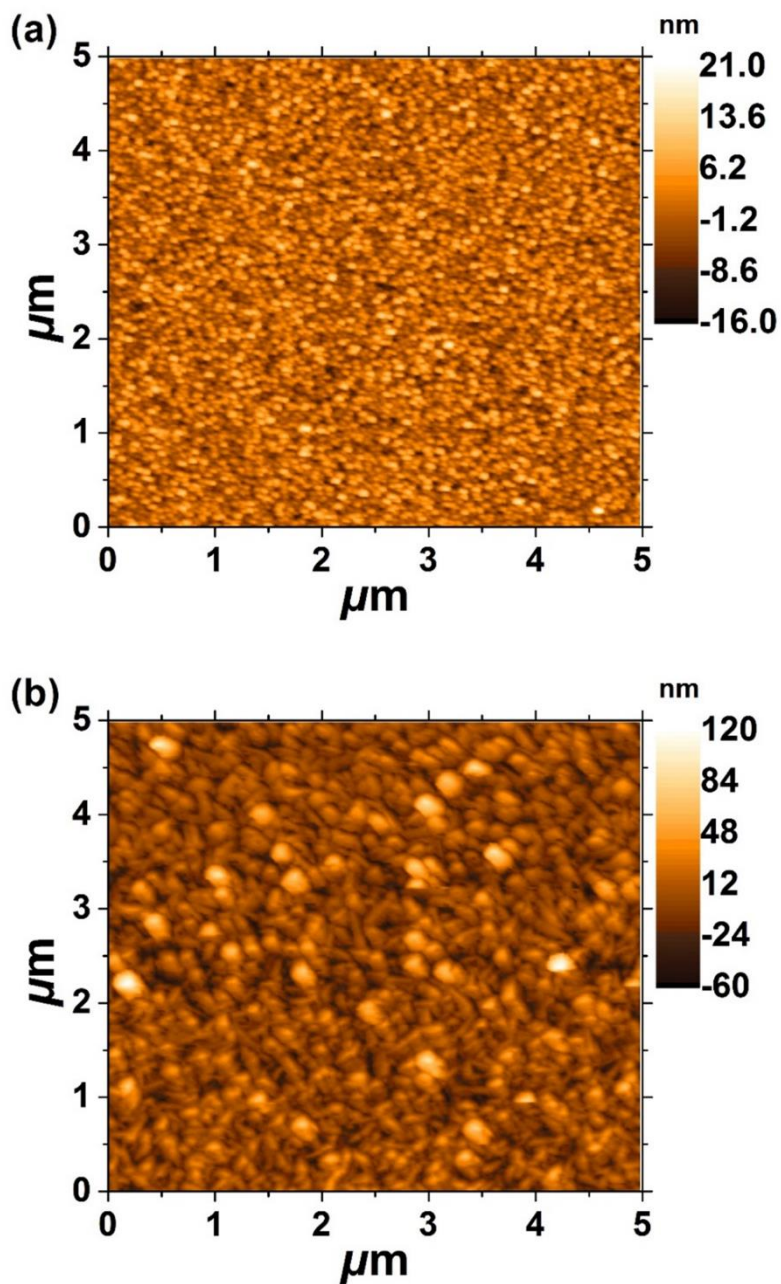
Figure 3.8 Atomic force microscopy (AFM) images of 60-nm-thick PbPc films grown on Glass / Cr (10 nm) / Ag (200 nm) / C_{60} (60 nm) (a) without substrate heating and (b) with substrate heating. Dimensions: 5×5 μm.
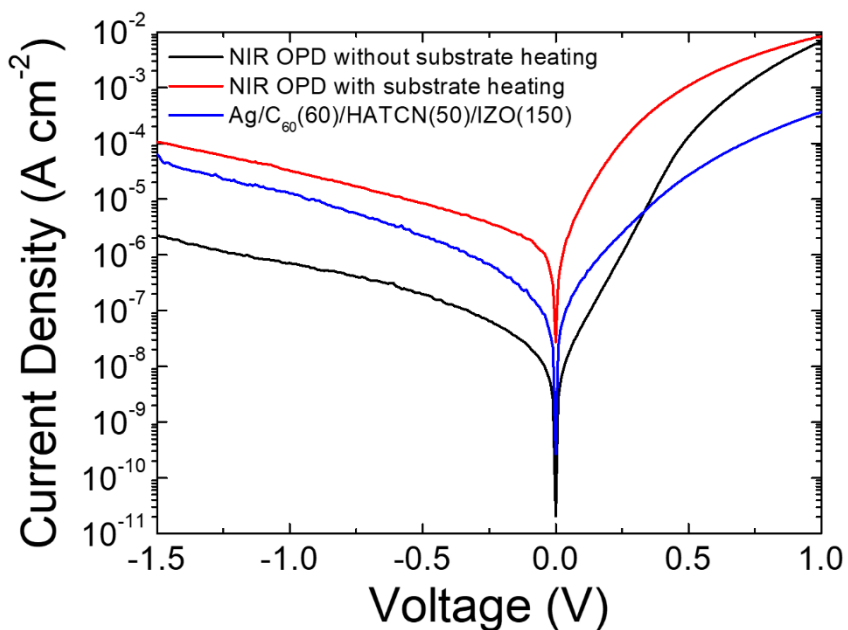
Figure 3.9 The dark current densities of NIR OPDs and devices without PbPc layers. The black, red, and blue lines represent NIR OPDs created without substrate heating, with such heating, and a device without the PbPc layer, respectively. The latter device does not exhibit a diode characteristic, indicating that formation of the interface between C_{60} and HATCN increases the dark current density in the reverse bias region.

Table 3.1 Organic photodetector parameters with and without substrate heating. Series resistance (R_S) values, ideality factors (n), and dark saturation current densities (J_S values) were obtained by fitting the dark current-voltage (J-V) curve to the Shockley diode equation. Open circuit voltages (V_{OC} values) were calculated using the parameters in the Table and the Shockley diode equation.

	V_{OC} (V)	J_{SC} (mA/cm^2)	R_S (Ωcm^2)	n	J_S (mA/cm^2)	Cal. V_{OC} (V)	EQE [b] (%)	Responsivity [b] (mA/W)
Reference device	0.501	2.851	13.0	1.81	2.81×10^{-9}	0.533	4.39	8.41
with substrate heating	0.326	2.504	44.3	1.79	6.66×10^{-6}	0.330	0.913	35.8

a) The values of J_S, R_S, and n were extracted from dark current density-voltage curves using the Shockley diode equation.

b) The data were obtained at 960 nm under zero bias.

3.4 Conclusion

We fabricated PbPc-based inverted OPDs detecting NIR light longer than 900 nm. PbPc molecules deposited on heated C_{60} substrates were in the triclinic, not monoclinic, phase at the interface, dramatically increasing the responsivity from 8.4 to 35.8 mA/W and the EQE from 0.9 to 4.4% at 960 nm compared to monoclinic PbPc. Although the dark current density of NIR OPDs prepared with substrate heating increased because of a change in surface morphology, our method is easy (a vacuum process) and affords good responsivity. It would be very useful to develop a method to reduce the dark current without sacrificing responsivity at 940 nm.

Chapter 4. Control of crystallinity in PbPc:C$_{60}$ blend film and application for inverted near-infrared organic photodetector

4.1 Introduction

Here, we report on the controlled crystallinity of PbPc in a PbPc:C$_{60}$ blended layer for NIR absorption. To form the triclinic phase in the layer, the substrate was heated during fabrication and C$_{60}$ was used as an electron extraction layer between the cathode and photoactive layer, as well as a templating layer. This configuration showed enhanced NIR absorption and a dramatic change in film morphology. These changes were confirmed by X-ray diffraction (XRD) measurements. Using a 1,4,5,8,9,11-hexaazatriphenylene-hexacarbonitrile (HATCN) as a buffer to protect the organic layer during sputtering, OPDs with enhanced NIR absorption exhibited a responsivity of 244 mA/W and an EQE of 31.1% at a reverse bias of −3 V at 970 nm. As a result, the detectivity of the OPDs increased to 9.01×10^{12} cm Hz$^{1/2}$/W and 1.36×10^{11} cm Hz$^{1/2}$/W under zero and reverse bias of −3 V, respectively.

4.2 Experimental

Film fabrication

The organic films used for measuring optical and structural properties had the following structures: (i) substrate / PbPc:C_{60} (2.5:1, 250 nm) and (ii) substrate / C_{60} (40 nm) / PbPc:C_{60} (2.5:1 volume ratio, 250 nm). A fused silica substrate was used to obtain the optical properties of the organic films. A silicon substrate was used to investigate the structural properties. All of the substrates were cleaned with a piranha treatment before use. C_{60} served not only as the templating material, but also as the acceptor material, and was deposited via thermal evaporation onto the substrate at a rate of 0.5 Å/s. PbPc served as the donor material for NIR light absorption and was co-deposited at a rate of 0.143 Å/s with C_{60} at a rate of 0.057 Å/s, both with and without substrate heating. In the case of substrate heating, the substrate was heated to 180°C.

Device fabrication

The inverted OPDs had the following structure: indium tin oxide (ITO, 70 nm) / C_{60} (40 nm) / PbPc:C_{60} (2.5:1, 250 nm) / PbPc (40 nm) / HATCN (50 nm) / indium zinc oxide (IZO, 10 nm). The ITO substrate was successively cleaned with detergent solution, acetone, and isopropyl alcohol to remove particles and organic materials. A neat C_{60} layer and mixed layer were fabricated under the same conditions as the films discussed above. A neat PbPc layer was deposited at a rate of 1.0 Å/s to prevent the formation of an interface between C_{60} and HATCN, which would increase the dark current density in the

reverse bias region. HATCN served not only as a hole-extraction layer, but also as a buffer to protect the organic layers during formation of the IZO top electrode via sputtering.[64] The HATCN deposition rate was 0.2 Å/s. All of the organic layers were deposited at a base pressure $< 1 \times 10^{-7}$ Torr. The substrate was then transferred through a load-lock to another chamber, where the IZO top electrode was formed on top of the HATCN layer using a sputtering process. Sputtering took place under gas flow rates of 30 sccm for Ar and 0.6 sccm for O_2, and a working pressure of 1.9 mTorr. After fabrication, the devices were encapsulated in an N_2 atmosphere before measurements.

Characterization of films and devices

Ultraviolet-visible (UV-Vis) absorption spectra were recorded by a Varian Cary 5000 UV-Vis spectrophotometer. Field-emission scanning electron microscopy (FE-SEM, Carl Zeiss Auriga) was used to observe the microstructures of the organic films. The crystalline structure was explored via synchrotron XRD with a MAR CCD (sample-to-detector distance: 215 mm) at the 3C X-ray scattering beamline for materials science (Pohang Light Source II; PLS-II). The X-ray wavelength was 1.23 Å (10.07 keV). Current density-voltage (*J-V*) characteristics were measured under dark conditions using a Keithley 237 source measurement unit. The EQE was measured using a 1,000-W Xe lamp (Oriel) combined with a calibrated monochromator (Acton Research). The intensity of monochromatic light was calibrated with the aid of a silicon photodiode (Newport).

4.3 Results and Discussion

Figure 4.1 shows the absorption spectra of organic films fabricated on fused silica substrates. The four films examined had the following structures: (i) fused silica / PbPc:C_{60} (2.5:1, 250 nm with substrate temperature ($T_{sub.}$) = room temperature (RT)) for film 1, (ii) fused silica / C_{60} (40 nm) / PbPc:C_{60} (2.5:1, 250 nm with $T_{sub.}$ = RT) for film 2, (iii) fused silica / PbPc:C_{60} (2.5:1, 250 nm with $T_{sub.}$ = 180°C) for film 3, and (iv) fused silica / C_{60} (40 nm) / PbPc:C_{60} (2.5:1, 250 nm with $T_{sub.}$ = 180°C) for film 4. Despite the large portion of PbPc in the film, only film 4 showed the triclinic phase formation, which is responsible for NIR absorption as discussed earlier. Thus, if PbPc molecules are co-deposited with C_{60} molecules, the PbPc molecules cannot form the triclinic phase, despite the increase in film thickness if the substrate is not heated. Film 3, fabricated with substrate heating during co-deposition of a PbPc:C_{60} mixed layer, showed lower absorption for red wavelengths and increased absorption in the NIR range; however, the absorption spectra changed only slightly, and no absorption peak was observed in the NIR region. Film 4 was the only film to show a clear absorption peak in the NIR region, in which the C_{60} substrate was heated. When PbPc molecules are deposited onto a heated substrate up to 180°C, they form a triclinic phase leading to absorption near 900 nm; however, film 4 showed an absorption peak at 950 nm, longer than that of the intrinsic PbPc layer. The reason why the blend film in this study shows the longer wavelength than the pure triclinic phase on a C_{60} layer is not clear at this moment. However, we speculate that the difference originates from
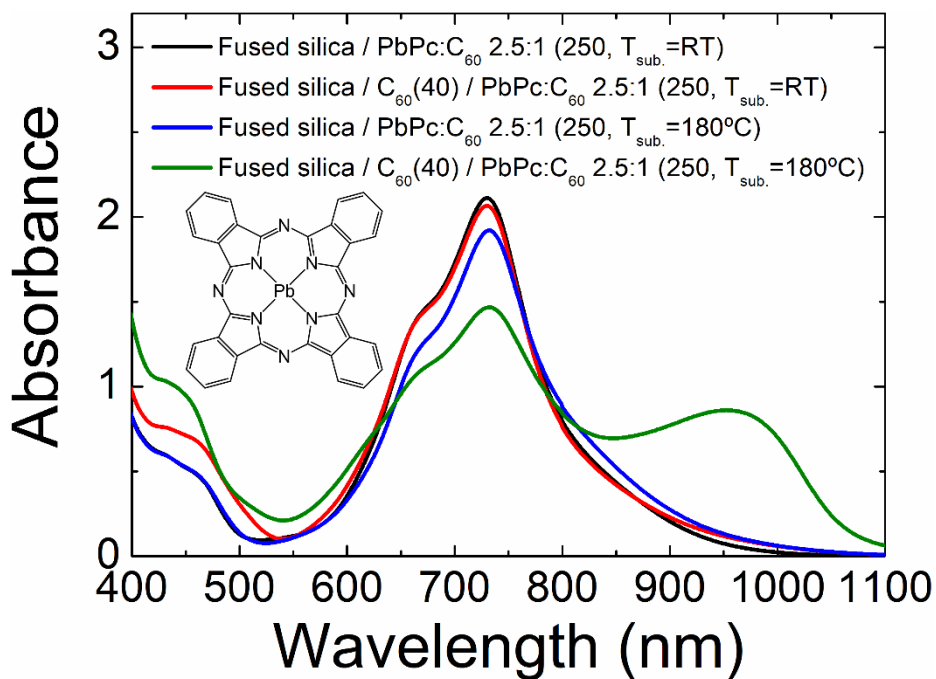
Figure 4.1 Absorption spectra of organic films on fused silica substrate. The film structures are fused silica / PbPc:C_{60} (2.5:1, 250 nm with $T_{sub.}$ = RT) for the black line, fused silica / C_{60} (40 nm) / PbPc:C_{60} (2.5:1, 250 nm with $T_{sub.}$ = RT) for the red line, fused silica / PbPc:C_{60} (2.5:1, 250 nm with $T_{sub.}$ = 180°C) for the blue line, and fused silica / C_{60} (40 nm) / PbPc:C_{60} (2.5:1, 250 nm with $T_{sub.}$ = 180°C) for the green line. Only one film formed on the heated C_{60} substrate showed a strong absorption peak at 950 nm. The insert shows the molecular structure of lead phthalocyanine.

the difference in orientation of the triclinic phase inducing different intermolecular interaction with the polarization of the incoming light.

Figure 4.2, 4.3 and 4.4 show top and cross-sectional FE-SEM images of organic films deposited on a silicon substrate. The structures of the films were the same as those of the absorbing films, except for the substrate. A polished silicon substrate was used to minimize the effect of the substrate on film growth. The organic films fabricated at ambient temperature have a flat surface. No crystalline structure or grain boundary was observed in FE-SEM images (figure 4.2a and 4.2b), implying that when PbPc and C_{60} molecules are co-deposited, they are easily blended to create an amorphous phase. In contrast, the PbPc:C_{60} blend film fabricated on a heated silicon substrate exhibited crystalline structure in several places, as shown in figure 4.3a and 4.3b. The crystalline structure exhibited in figure 4.3b consisted of several grains. The thickness of the film obtained from a cross-sectional FE-SEM image (figure 4.3a) was 285 nm, thicker than that shown in figure 4.2a (255 nm). Substrate heating-induced crystallization led to a volume expansion of 12% because of the porous structure. When the PbPc:C_{60} mixed layer was deposited onto the heated C_{60} layer, which was pre-deposited on the silicon substrate, dramatic changes occurred, as shown in figure 4.4a and 4.4b. Crystallization was observed over the surface, in addition to significant volume expansion again due to the porous structure. The film thickness in the cross-sectional FE-SEM image of figure 4.4a was 350 nm. With consideration of a 40-nm-thick C_{60} layer, the thickness of the PbPc:C_{60} mixed film expanded from 255 nm to 310 nm, implying a
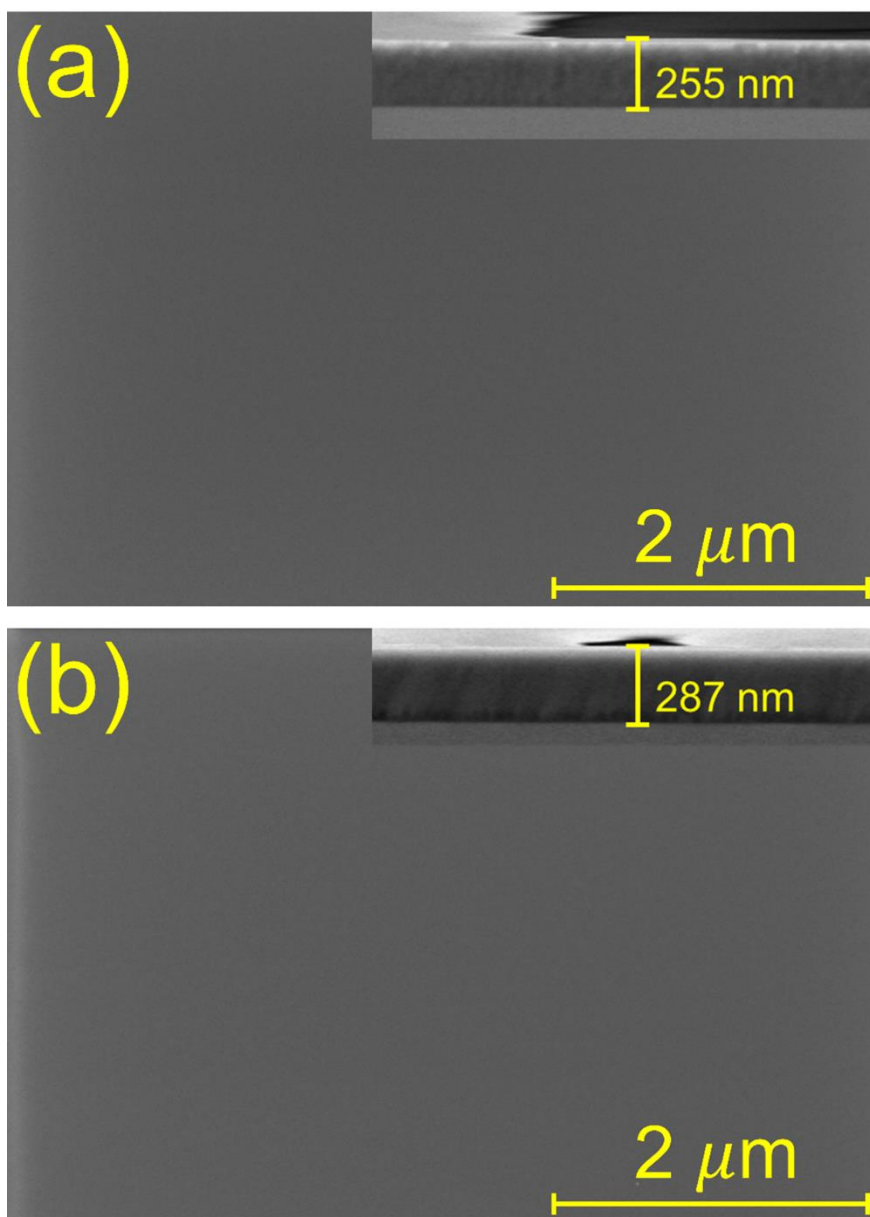
Figure 4.2 Field-emission scanning electron microscopy (FE-SEM) images of the organic films on silica (Si) substrate. The film structures are Si / PbPc:C_{60} (2.5:1, 250 nm with $T_{sub.}$ = RT) for image (a), Si / C_{60} (40 nm) / PbPc:C_{60} (2.5:1, 250 nm with $T_{sub.}$ = RT) for image (b). FE-SEM image without heating shows a flat surface. Inset images show the cross-section of the organic thin film on a Si substrate.
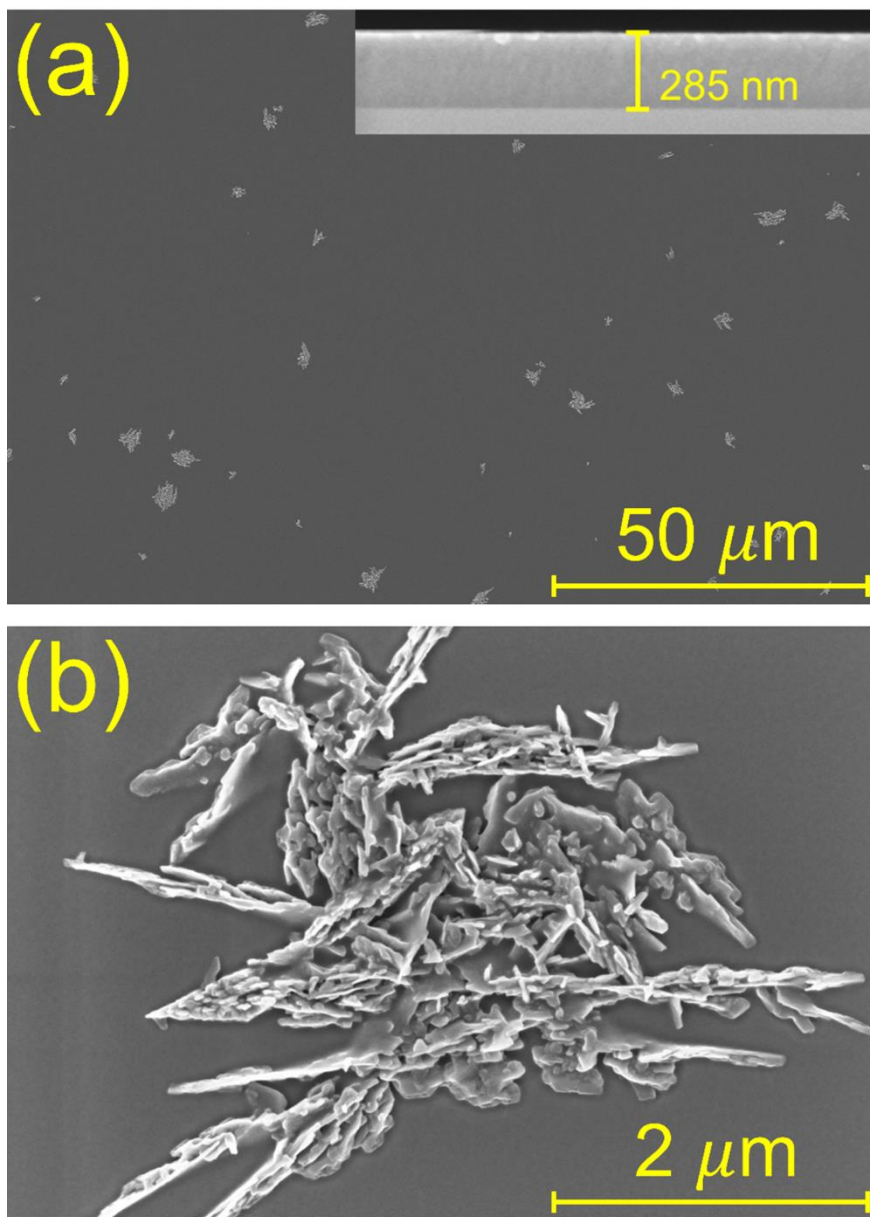
Figure 4.3 Field-emission scanning electron microscopy (FE-SEM) images of the organic films on silica (Si) substrate. The film structure is Si / PbPc:C_{60} (2.5:1, 250 nm with $T_{sub.}$ = 180°C). Some crystalline structure was found in the PbPc:C_{60} blend film deposited onto a heated Si substrate. Inset image shows the cross-section of the organic thin film on a Si substrate.
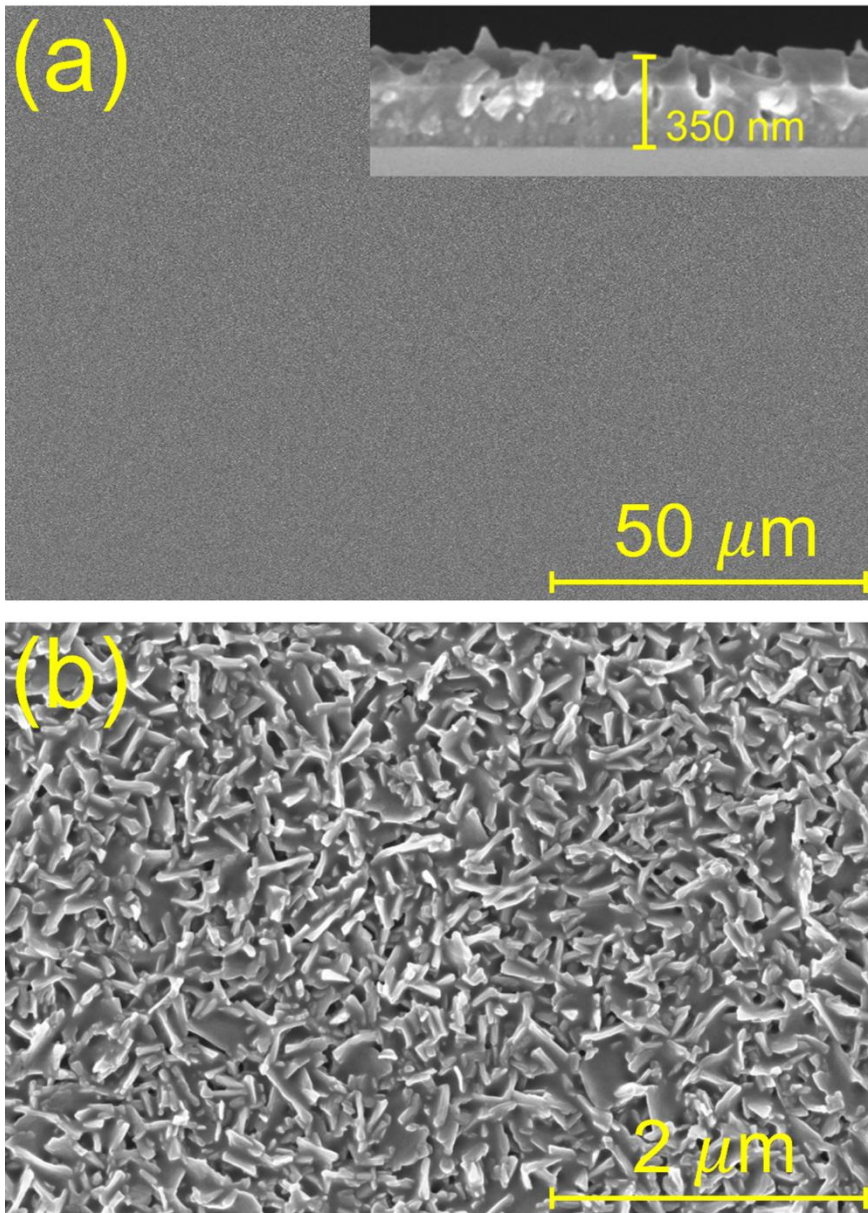
Figure 4.4 Field-emission scanning electron microscopy (FE-SEM) images of the organic films on silica (Si) substrate. The film structure is Si / C_{60} (40 nm) / PbPc:C_{60} (2.5:1, 250 nm with $T_{sub.} = 180°C$). The film deposited onto a heated C_{60} substrate shows a rough surface. Inset image shows the cross-section of the organic thin film on a Si substrate.
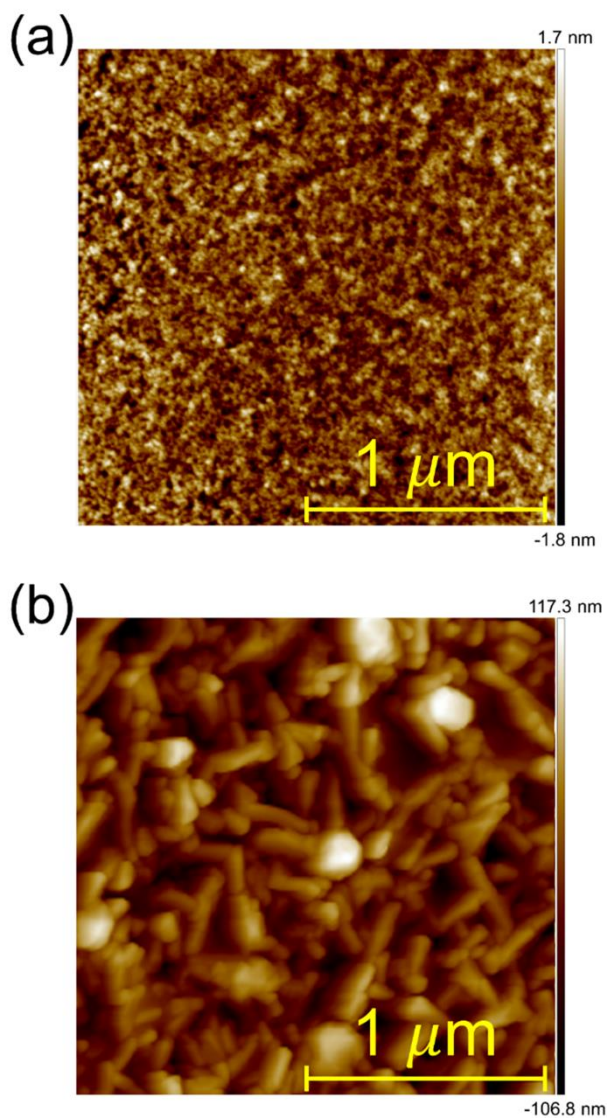
Figure 4.5 Atomic force microscopy (AFM) images of organic films. The film structures are Si / C_{60} (40 nm) / PbPc:C_{60} (2.5:1, 250 nm with $T_{sub.}$ = RT) for image (a) and Si / C_{60} (40 nm) / PbPc:C_{60} (2.5:1, 250 nm with $T_{sub.}$ = 180°C) for image (b). With substrate heating, R_q(R_{rms}) increased from 0.5 nm to 31.6 nm and R_a increased from 0.4 nm to 25.1 nm.

volume expansion of 22%. This crystallization is consistent with the changes in the absorption spectra (figure 4.1). Figure 4.5 shows the Atomic force microscopy (AFM) images of organic films with the structure of Si / C_{60} (40 nm) / PbPc:C_{60} (2.5:1, 250 nm with $T_{sub.}$ = RT and 180°C). With substrate heating, R_q(R_{rms}) increased from 0.5 nm to 31.6 nm and R_a increased from 0.4 nm to 25.1 nm. In the OPDs, PbPc (40 nm) and HATCN (50 nm) are deposited onto the mixed layer. Thus, it is difficult to form the smooth interface between C_{60} and HATCN which may increase the dark current density[114].

Grazing incidence X-ray diffraction (GIXRD) was used to investigate the origin of the surface morphology changes. The four solid lines shown in figure 4.6, black, red, blue, and green, represent the GIXRD patterns of Si / PbPc:C_{60} (2.5:1, 250 nm with $T_{sub.}$ = RT), Si / C_{60} (40 nm) / PbPc:C_{60} (2.5:1, 250 nm with $T_{sub.}$ = RT), Si / PbPc:C_{60} (2.5:1, 250 nm with $T_{sub.}$ = 180°C), and Si / C_{60} (40 nm) / PbPc:C_{60} (2.5:1, 250 nm with $T_{sub.}$ = 180°C), respectively; the structures of these films were the same as those of FE-SEM samples. The black and red lines showed two broad diffraction peaks near Q = 5.5 and 14.5 nm^{-1}, which were assigned to the (120)-oriented PbPc monoclinic phase (Q = 5.51 nm^{-1}) and the combination of the (530)-oriented PbPc monoclinic phase (Q = 14.38 nm^{-1}) and the (311)-oriented face-centered cubic (FCC) phases (Q = 14.72 nm^{-1}).[108,110] The peak near Q = 7.7 nm^{-1} was observed in the red line and represents the (111)-oriented FCC phases (Q = 7.69 nm^{-1}) attributable to the intrinsic C_{60} layer. The blue line showed a strong diffraction peak near Q = 5.1 nm^{-1} representing the (200)-oriented PbPc monoclinic phase (Q = 4.93 nm^{-1})
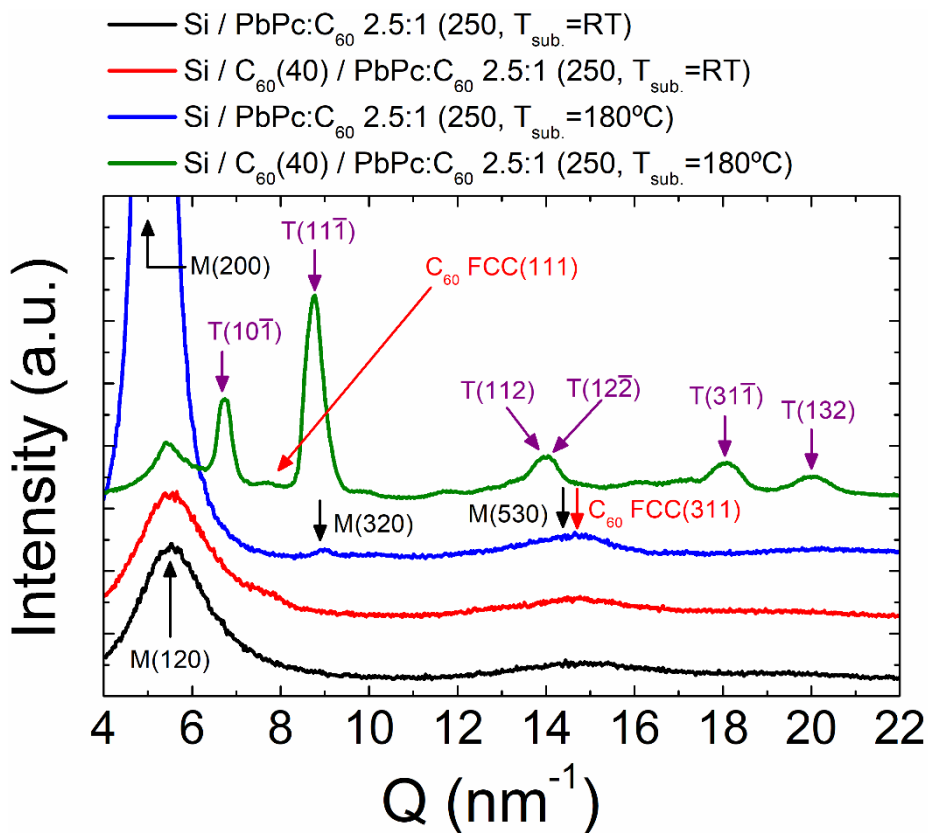
Figure 4.6 Grazing incidence X-ray diffraction (GIXRD) patterns of the organic films. The film structures are Si / PbPc:C_{60} (2.5:1, 250 nm with $T_{sub.}$ = RT) for the black line, Si / C_{60} (40 nm) / PbPc:C_{60} (2.5:1, 250 nm with $T_{sub.}$ = RT) for the red line, Si / PbPc:C_{60} (2.5:1, 250 nm with $T_{sub.}$ = 180°C) for the blue line, and Si / C_{60} (40 nm) / PbPc:C_{60} (2.5:1, 250 nm with $T_{sub.}$ = 180°C) for the green line. Black, purple and red arrows indicate PbPc monoclinic phase, PbPc triclinic phase and C_{60} face-centered cubic (FCC) phase, respectively.

Table 4.1 Calculated XRD peak position and corresponding planes using lattice parameters of the PbPc monoclinic phase, triclinic phase, and C_{60} face-centered cubic phase. The lattice parameters of the PbPc monoclinic phase (space group = $\mathbf{P2_1/b}$; a = b = 2.548 nm; $\mathbf{\gamma}$ = 90°) and the triclinic phase (space group = $\mathbf{P\bar{1}}$; a = 1.313 nm, b = 1.613 nm, c = 1.289 nm; $\mathbf{\alpha}$ = 94.22°, $\mathbf{\beta}$ = 96.20°, $\mathbf{\gamma}$ = 114.19°) are used.[108,110,111]

Peak positon (nm^{-1})	Phase	Reflection plane
4.93	Monoclinic	(200)
5.31	Triclinic	(100)
5.51	Monoclinic	(120)
6.68	Triclinic	(10$\bar{1}$)
7.69	FCC (C_{60})	(111)
8.77	Triclinic	(11$\bar{1}$)
8.89	Monoclinic	(320)
9.63	Triclinic	(2$\bar{1}$0)
10.2	Triclinic	(111)
11.7	Triclinic	(11$\bar{2}$)
11.72	Triclinic	(1$\bar{3}$0)
13.15	Triclinic	(21$\bar{1}$)
13.28	Monoclinic	(520)
13.82	Triclinic	(112)
14.17	Triclinic	(12$\bar{2}$)
14.38	Monoclinic	(530)
14.75	FCC (C_{60})	(311)
15.97	Triclinic	(1$\bar{1}$3)
16.17	Triclinic	(22$\bar{1}$)
18.03	Triclinic	(31$\bar{1}$)
20	Triclinic	(132)

and a weak diffraction peak near $Q = 8.9$ nm^{-1} representing the (320)-oriented PbPc monoclinic phase ($Q = 8.89$ nm^{-1}) and $Q = 14.5$ nm^{-1}. All of the peaks indicated the formation of a monoclinic crystalline structure, which was enhanced by substrate heating. In contrast, the green line exhibited six clear diffraction peaks near $Q = 5.5$, 6.7, 8.8, 14.0, 18.0, and 20.0 nm^{-1} attributable to the (120)-oriented PbPc monoclinic phase ($Q = 5.51$ nm^{-1}), the $(10\bar{1})$-oriented PbPc triclinic phase ($Q = 6.68$ nm^{-1}), the $(11\bar{1})$-oriented PbPc triclinic phase ($Q = 8.77$ nm^{-1}), the combination of the (112)-oriented PbPc triclinic phase ($Q = 13.82$ nm^{-1}) and the $(12\bar{2})$-oriented PbPc triclinic phase ($Q = 14.17$ nm^{-1}), the $(31\bar{1})$-oriented PbPc triclinic phase ($Q = 18.03$ nm^{-1}), and the (132)-oriented PbPc triclinic phase ($Q = 20.00$ nm^{-1}), respectively.[111] Table 4.1 lists the calculated XRD peak positions and corresponding planes using the lattice parameters of the PbPc monoclinic phase, triclinic phase, and C_{60} FCC phase.[108,110,111] In addition, the GIXRD patterns of the mixed film are different from that of neat PbPc films on C_{60} substrate, as shown in previous chapter. In the neat film of PbPc deposited onto heated C_{60} substrate, the $(1\bar{2}1)$, $(11\bar{2})$, $(1\bar{3}0)$, $(2\bar{2}1)$, $(3\bar{3}0)$ and $(1\bar{1}3)$ -oriented PbPc triclinic phases were observed.[114] in contrite, PbPc triclinic phase in minxed layer showed the GIXRD pattern with peaks from the $(10\bar{1})$, $(11\bar{1})$, (112), $(12\bar{2})$, $(31\bar{1})$ and (132) -oriented PbPc triclinic phases, indicating that the orientation of triclinic phases in the mixed layer is different from that in intrinsic layer. Thus, the possible reason for red-shift in absorption is coming from the change in molecular interaction in triclinic phases with different orientation. The

GIXRDpatterns clearly indicated triclinic phase formation only with a heated C_{60} layer; these patterns were consistent with absorption spectra (figure 4.1) and FE-SEM measurements (figure 4.2, 4.3 and 4.4).

Figure 4.7a shows the *J-V* characteristics of NIR OPDs with the structure of ITO (70 nm) / C_{60} (40 nm) / PbPc:C_{60} (2.5:1, 250 nm) / PbPc (40 nm) / HATCN (50 nm) / IZO (10 nm) in the dark and under 940 nm illumination (6.6 mW/cm^2). The black color indicates the device without substrate heating and the red color with substrate heating. The thickness of the IZO top electrode was only 10 nm, to minimize sputtering damage by minimizing the exposure time of the organic material to the plasma. However, if the thickness of the top IZO electrode is too thin, the electrode will not cover all of the organic material, and the device characteristics will not be observed. The OPDs with substrate heating during deposition of the PbPc:C_{60} blend layer showed a higher dark current density in the reverse bias region during OPD operation. The reason for the increase in the dark current density was not clear; however, the rough surface induced by crystallization in the PbPc:C_{60} blend layer may have been a contributing factor, as shown in figure 4.4.[112] The photo current densities under 940 nm light source show dramatic enhancement from 1.29×10^{-5} to 1.67×10^{-4} A/cm^2, from 4.36×10^{-5} to 7.91×10^{-4} A/cm^2 and from 9.43×10^{-5} to 1.38×10^{-3} A/cm^2 at 0 V, −1 V and −3 V, respectively (summarized in Table 4.2).

Figure 4.7b shows the EQE spectra of NIR OPDs fabricated without and with substrate heating under zero and reverse biases of −1 V and −3 V. Reverse

bias as well as zero bias were used in the measurements because OPDs are normally operated in reverse bias for efficient and rapid extraction of generated charges. Maximum EQE was observed at 970 nm with values of 6.3% at 0 V, 26.6% at −1 V and 31.1% at −3 V, which is 20 nm red-shifted from absorption peak due to an interference effect. In contrast, the EQE values of non-heated OPD are only 0.13% at 0 V, 0.43% at −1 V and 0.94% at −3 V. The change in EQE spectra implies that substrate heating during device fabrication induced the NIR response attributable to triclinic absorption, whereas no NIR response was observed in the device without substrate heating. These spectral responses are consistent with absorption spectra, FE-SEM, and GIXRD findings as discussed above. The responsivity (R) and the detectivity (D^*) spectra in Figure 4.8a and 4.8b were calculated from the expressions of $R = I_{photo}/P_{light}$ and $D^* = R/(2qJ_d)^{1/2}$, respectively, where I_{photo} is the photo-current from the device, P_{light} is the incident optical power at each wavelength, q is the absolute value of electron charge (1.6×10^{-19} C) and J_d is the dark current density at the applied voltage, respectively. The values of responsivity dramatically increased with substrate heating from 0.99 to 49.2 mA/W, 3.4 to 208 mA/W and from 7.3 to 244 mA/W at 0 V, −1 V and −3 V, respectively. With the low dark current density, the values of detectivity also increased from 2.14×10^{11} to 9.01×10^{12} cm Hz$^{1/2}$/W, from 5.34×10^9 to 2.35×10^{11} cm Hz$^{1/2}$/W from 6.52×10^9 to 1.36×10^{11} cm Hz$^{1/2}$/W at 0 V, −1 V and −3 V, respectively. These results are one of the highest EQE and detectivity values in vacuum processed inverted NIR OPDs to our best knowledge.[17,61,75,78–80,62,68–74]
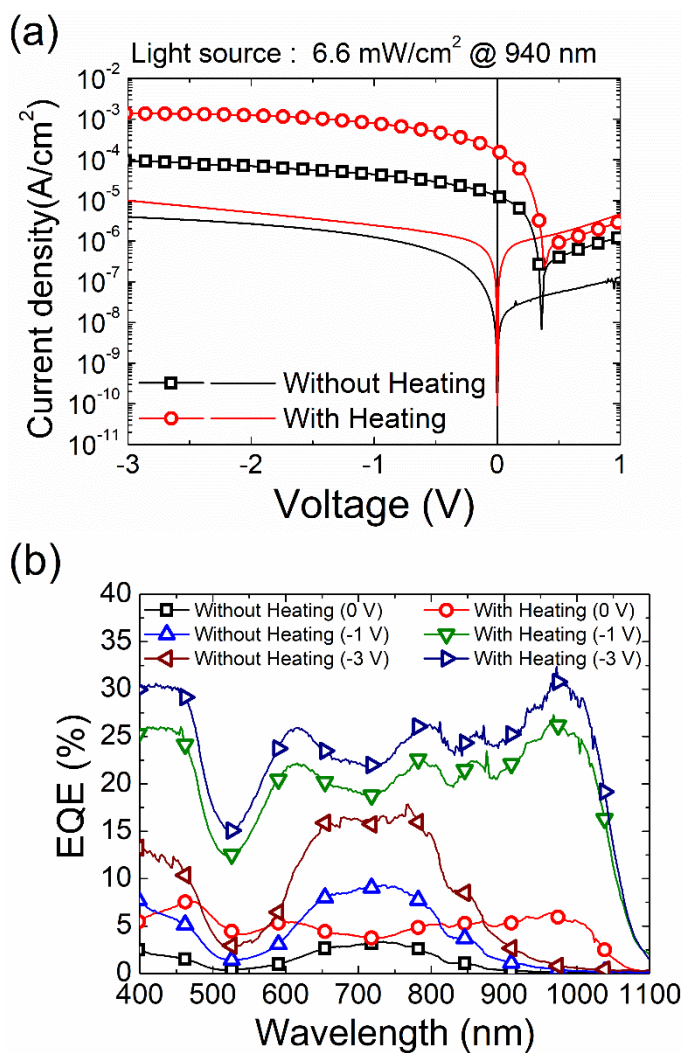
Figure 4.7 (a) Dark current densities and photocurrent densities under 940 nm illumination (6.6 mW/cm^2) of the near-infrared (NIR) organic photodetectors (OPDs). The black color indicates the device without substrate heating and the red color indicates the device with substrate heating. The device structures are indium tin oxide (ITO, 70 nm) / C$_{60}$ (40 nm) / PbPc:C$_{60}$ (2.5:1, 250 nm) / PbPc (40 nm) / 1,4,5,8,9,11-hexaazatriphenylenehexacarbonitrile (HATCN, 50 nm) / indium zinc oxide (IZO, 10 nm). (b) External quantum efficiency for the devices from (a).
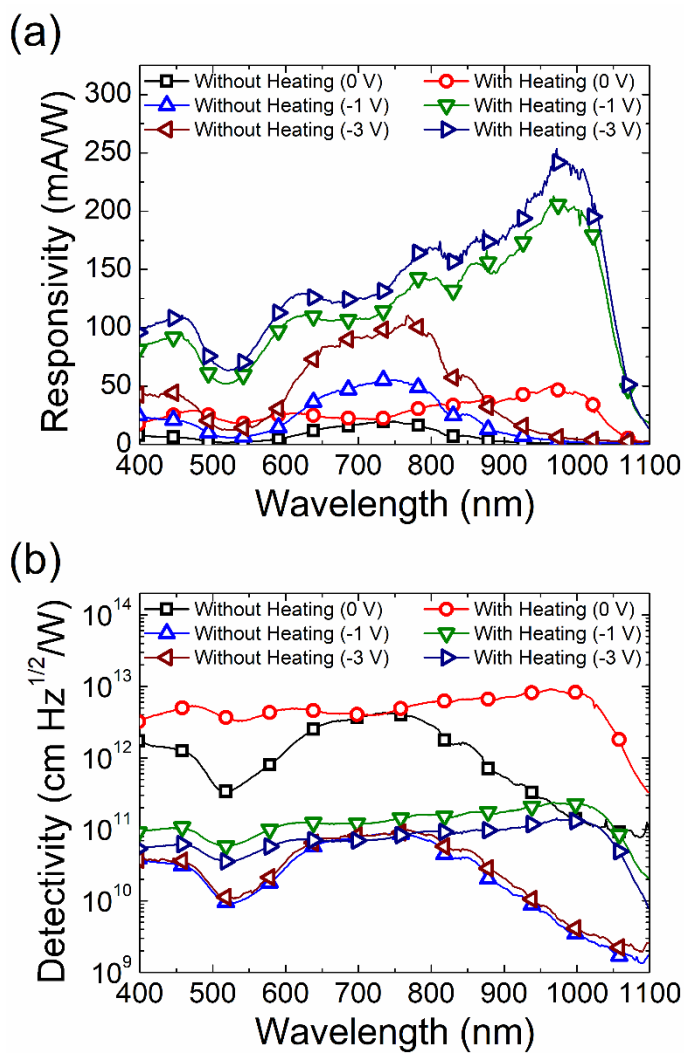
Figure 4.8 (a) The responsivity spectra, and (b) the detectivity spectra for the NIR OPDs. The device structures are indium tin oxide (ITO, 70 nm) / C_{60} (40 nm) / PbPc:C_{60} (2.5:1, 250 nm) / PbPc (40 nm) / 1,4,5,8,9,11-hexaazatriphenylene-hexacarbonitrile (HATCN, 50 nm) / indium zinc oxide (IZO, 10 nm).

Table 4.2 Organic photodetector parameters with and without substrate heating. The photocurrent densities were measured under 940 nm illumination (6.6 mW/cm²). EQE data were obtained at 970 nm at 0 V, −1 V and −3 V. Responsivity and detectivity were calculated from dark current density and EQE values.

	With substrate heating			Without substrate heating		
Voltage	0 V	−1 V	−3 V	0 V	−1 V	−3 V
Photo current density (A/cm^2)	1.29×10^{-5}	4.36×10^{-5}	9.43×10^{-5}	1.67×10^{-4}	7.91×10^{-4}	1.38×10^{-3}
Dark current density (A/cm^2)	6.7×10^{-11}	1.26×10^{-6}	3.94×10^{-6}	9.3×10^{-11}	2.45×10^{-6}	9.97×10^{-6}
EQE (%)	0.13	0.43	0.94	6.3	26.6	31.1
Responsivity (mA/W)	0.99	3.4	7.3	49.2	208	244
Detectivity (cm Hz$^{1/2}$/W)	2.14×10^{11}	5.34×10^{9}	6.52×10^{9}	9.01×10^{12}	2.35×10^{11}	1.36×10^{11}

4.4 Conclusion

We controlled the crystallinity of the PbPc in PbPc:C_{60} blend film to obtain NIR absorption. Heating the templating layer of C_{60} facilitated crystallinity of the blend layer and ultimately NIR absorption at 950 nm. However, neither the use of a templating layer without heating nor substrate heating without the templating layer induced NIR absorption in the blend layer. FE-SEM images and GIXRD patterns indicated that only the blend layer deposited onto a heated C_{60} layer showed crystallinity to induce NIR absorption. As such, we demonstrated NIR light detection up to 1,100 nm with an EQE of 31.1% and responsivity of 244 mA/W, at a reverse bias of −3 V and 970 nm. The detectivity of the OPDs also increased to 9.01×10^{12} cm $Hz^{1/2}$/W and 1.36×10^{11} cm $Hz^{1/2}$/W under zero bias and reversei bias of −3 V, respectively.

Chapter 5. Analysis of dark current density with theoretical model in PbPc-based near-infrared organic photodetectors

5.1 Introduction

Generally, OPDs are operated in reverse bias condition which can supply an electric field in the device, leading to efficient and rapid extraction of generated charges. However, the most researches have focused on the detectivity at zero bias, not reverse bias used for practical operation as shown in table 1.2 and figure 5.1a. The reason why many papers report detectivity at zero bias is higher electric field makes higher dark current density and lower detectivity of the OPDs, as shown in figure 5.1b. Suppressing the dark current density is required for higher detectivity in reverse bias region. HATCN buffer layer is used to prevent plasma damage during sputtering and N,N'-di(1-naphthyl)-N,N'-diphenyl-(1,1'-biphenyl)-4,4'-diamine (NPB) buffer layer is used to increase injection barrier. The analysis of dark current density is performed with theorical model.
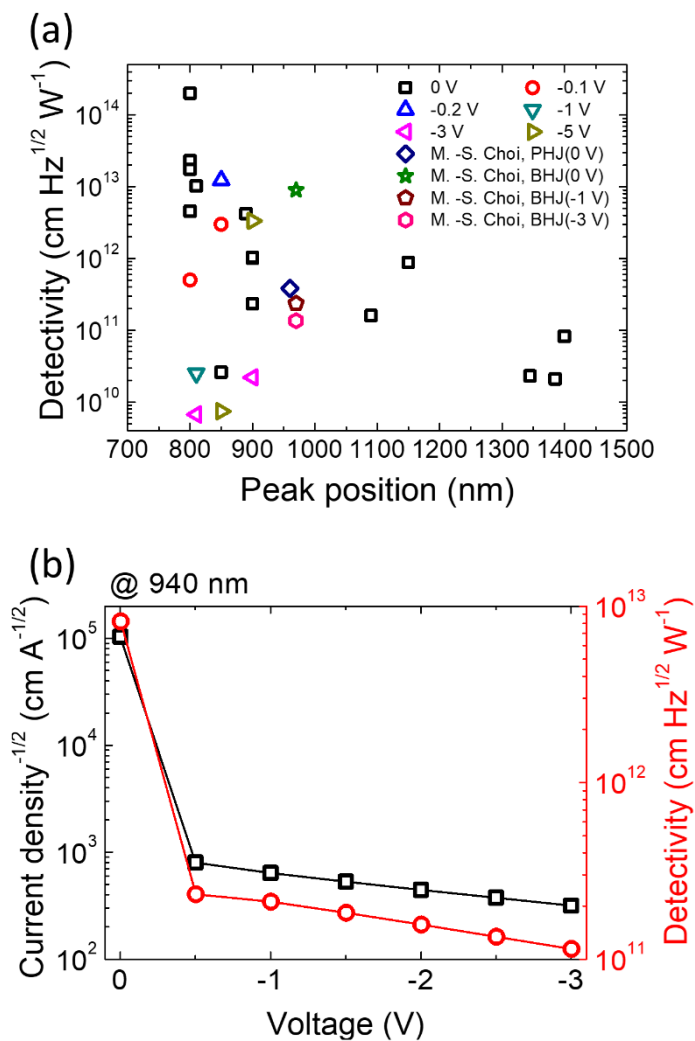
Figure 5.1 (a) Summary for previous reports on near-infrared organic photodetectors (discussed in the chapter 1). The legends indicate the operating voltage. (b) The reciprocal current density-voltage characterisitics and detectivity-voltage characterisitics of NIR OPD discussed in the chapter 4.

5.2 Experimental

The inverted OPDs had the following structure: indium tin oxide (ITO, 70 nm) / C_{60} (40 nm) / PbPc:C_{60} (2.5:1, 250 nm) / PbPc (40 nm) / HATCN (50 ~ 500 nm) / indium zinc oxide (IZO, 10 nm) for OPD without NPB burffer layer and ITO (70 nm) / C_{60} (40 nm) / PbPc:C_{60} (2.5:1, 250 nm) / PbPc (40 nm) / NPB (40 nm) / HATCN (500 nm) / IZO (10 nm) for OPD with NPB buffer layer. The ITO substrate was successively cleaned with detergent solution, acetone, and isopropyl alcohol to remove particles and organic materials. C_{60} served as the acceptor material, and was deposited via thermal evaporation onto the substrate at a rate of 0.5 Å/s. PbPc served as the donor material for NIR light absorption and was co-deposited at a rate of 0.143 Å/s with C_{60} at a rate of 0.057 Å/s, both with and without substrate heating. In the case of substrate heating, the substrate was heated to 180°C. A neat PbPc layer was deposited at a rate of 1.0 Å/s to prevent the formation of an interface between C_{60} and HATCN, which would increase the dark current density in the reverse bias region.[114] The NPB served as a electron blocking layer to prevent electron injection from HATCN and was deposited at a rate of 0.5 Å/s. HATCN served not only as a hole-extraction layer, but also as a buffer to protect the organic layers during formation of the IZO top electrode via sputtering.[64] The HATCN deposition rate was 0.2 Å/s. All of the organic layers were deposited at a base pressure < 1 × 10^{-7} Torr. The substrate was then transferred through a load-lock to another chamber, where the IZO top electrode was formed on top of the HATCN layer using a sputtering process. Sputtering took place under gas flow rates of 30

sccm for Ar and 0.6 sccm for O_2, and a working pressure of 1.9 mTorr. After fabrication, the devices were encapsulated in an N_2 atmosphere before measurements. Current density-voltage (*J-V*) characteristics were measured under dark conditions using a Keithley 237 source measurement unit. The EQE was measured using a 1,000-W Xe lamp (Oriel) combined with a calibrated monochromator (Acton Research). The intensity of monochromatic light was calibrated with the aid of a silicon photodiode (Newport).

5.3 Theoretical model for analysis

The most typical model used to describe the current density behavior of organic semiconductors is the Shockley diode equation. The Shockley diode equation is an equation that describes the dark current density flowing inside and is expressed as follows;

$$J_{dark} = J_0 \left[\exp\left(\frac{qV}{nkT} \right) - 1 \right] \tag{5.1}$$

where q, V, n, k, T represent the elecentary charge, the applied voltate, the ideality factor, the Boltzmann constant and temperature, respectively. J_0 is the dark saturation current density and expressed by $J_0 = J_{00} \exp\left(-\frac{\Delta E_{DA}}{2nkT} \right)$ where J_{00} is the pre-factor and ΔE_{DA} is energy difference between the HOMO level of the donor and the LUMO level of the acceptor. In real devices, there exists a series resistance (R_s) and a parallel resistance (R_p). R_s makes voltage drop in the device and R_p makes leakage current density. The Shockley diode equation is modified as follows;

$$J_{dark} = J_0 \left[\exp\left(\frac{q(V - JR_s)}{nkT} \right) - 1 \right] + \frac{V}{R_p} . \tag{5.2}$$

The value of R_s is typically in the range of a few ohms to a few hundred ohms. Assume that dark current density is 1 μA/cm², the voltage drop due to R_s is in the range of a few microohms to a few milli ohms. Thus, in this chapter,

the voltage drop due to R_s will not be considered in the reverse bias region. In other word, R_s of NIR OPDs discussed in this chaper will be ignored and only R_p will be considered.

When electrons that overcome the injection barrier at the electrode are injected into the organic layer, a different model should be used than the thermionic injection or tunneling injection commonly used in inorganic semiconductors. In this case, the injection current density can be explainded with Scott-Milliaras model.[115] It can be desctibed as;

$$J_{injection} = 4\psi^2 N_0 q\mu E \exp(-\phi_B / kT) \exp f^{1/2} \qquad (5.3)$$

where reduced electric field[115] is

$$f = eEr_c / kT . \qquad (5.4)$$

Hrer, r_C is Coulomb radius ($r_C = e^2 / 4\pi\varepsilon\varepsilon_0 kT$) and

$$\psi(f) = f^{-1} + f^{-1/2} - f^{-1}(1 + 2f^{1/2})^{1/2} . \qquad (5.5)$$

N_0, μ, E, ϕ_B represent the density of chargeable sites, mobility of injected charge carriers, electric field at the interface and injection barrier at the interface. To consider a band bending at the interface, effective field coefficient, C_{effect}, is introduced. Electric field at the interface is expressed as;

$$E = \left(\frac{V_{applied}}{d_{organic}}\right) \cdot C_{effect}. \tag{5.6}$$

In order to describe the dark current density, new model which is combination of diode equation and Scott-Milliaras equation is suggested. The dark current density in the reverse bais region can be described as summation of the current densities;

$$J_{dark} = J_{diode} + J_{leakage} + J_{injection} \tag{5.7}$$

where diode current density is

$$J_{diode} = J_0 \left[\exp\left(\frac{qV}{nkT}\right) - 1 \right], \tag{5.8}$$

the leakage current density is

$$J_{leakage} = \frac{V}{R_p} \tag{5.9}$$

and the injection current density is

$$J_{injection} = 4\psi^2 q\mu N_0 E \exp\left(-\phi_B/kT\right) \exp f^{1/2}. \tag{5.10}$$

5.4 Results and Discussion

Figure 5.2 shows the *J-V* curves with various HATCN thickness. An increase in thickness of HATCN buffer layer resulted in a decrease in dark current density. However, with an applied voltage of -3 V, dark current density saturates to specific value which is in range of $4 \sim 5 \ \mu A/cm^2$. It can be discussed with three components as mentioned above: diode current, leakage current and injection current. Here, reverse bias region can be divided into two regions; diode current dominant region and injection current dominant region. When electron is injected from LUMO of HATCN to LUMO of PbPc triclinic phase, injection barrier can be expected to 0.84 eV with ICT medel[116,117]. Thus, the injection current can be negligible where the absolute value of applied voltage is lower than ~ 0.9 V and diode current can be negligible where the absolute value of applied voltage is higher than ~ 0.9 V.

Figure 5.3a shows the *J-V* curves in diode current dominant region with various HATCN thickness. With an increase in thickness of HATCN, dark current density decreased and the same tendency is shown where absolute value of applied voltage is in range of $0.1 \sim 0.9$ V. The decrease in dark current density can be discussed with plasma damage during sputtering and increase in resistance with increasing the thickness of HATCN buffer layer. If thickness of HATCN buffer layer is not enough to prevent plasma damage, the damage can reach to organic layer leading to leakage current. In this case, as the thickness of HATCN buffer layer increases, the leakage current density decreases along
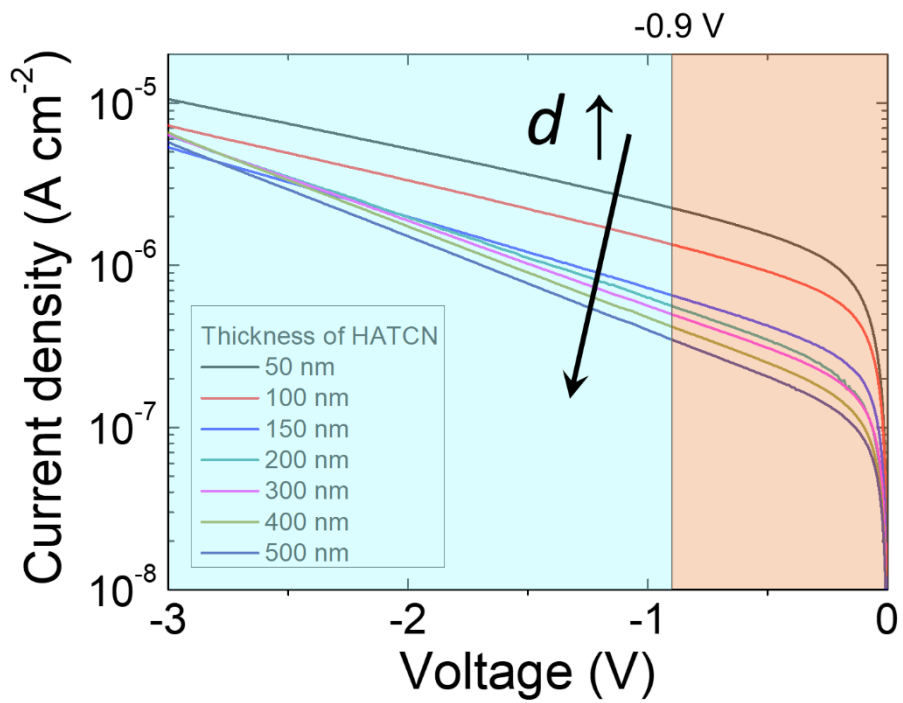
Figure 5.2 *J-V* curves in reverse bias region with various HATCN thickness. Blue region indicates diode current dominant region and red region indicates injection current dominant region.
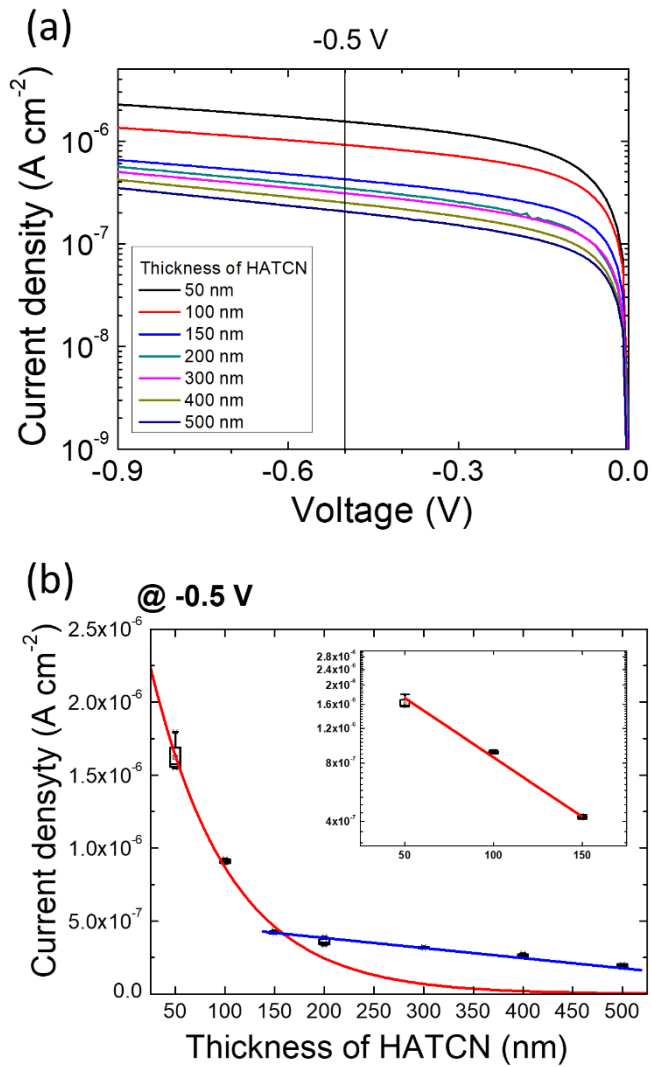
Figure 5.3 (a) *J-V* curves in diode current dominant region with various HATCN thickness. (b) HATCN thickness dependent dark current density at reverse bias of -0.5 V (inset: semi-log scale).
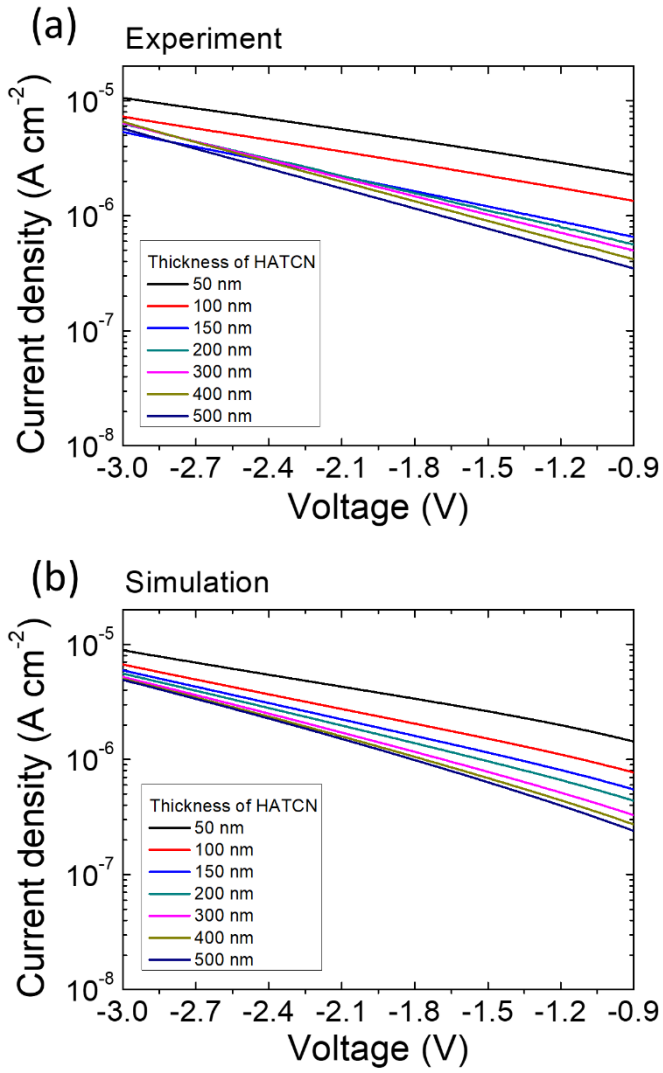
Figure 5.4 *J-V* curves in injection current dominant region with various HATCN thickness. (a) measurement (b) simulation

the exponential function. This is similar to the general energy transfer equation. The red solid line in figure 5.3b represent the exponential decrease in leakage current density. On the other hand, when the thickness of HATCN buffer layer is over 150 nm, it shows a different tendency. Leakage current density decreases along the linear function, meaning that 150 nm of HATCN buffer layer can prevent plasma damage effectively and current density decreases with increase in resistance.

Figure 5.4a and 5.4b show the measured and the simulated J-V curves in injection current dominant region with various HATCN thickness, respectively. For the qualitative analysis of J-V curves in the region, equation (5.7) was modified;

$$J_{dark} = J_{injection} + J_{leakage} \qquad (5.11)$$

and Rp is assumed as;

$$R_p = 13600 \times d_{HATCN} \qquad (5.12)$$

with ε_r =3.0, T=300K, N_0=1 × 10^{27} #/m³, ϕ_B =0.9 eV and μ=1cm²/Vs[118]. With the increase in HATCN thickness, simulated dark current density at -3 V saturate to 4.47 μA/cm² which is the the simulated injection current density at -3 V. The model suggested here can explain the J-V curves with various HATCN thickness very well. However, to reduce the dark current density in reverse bias region, injection current should be suppressed. The effective way to reduce the
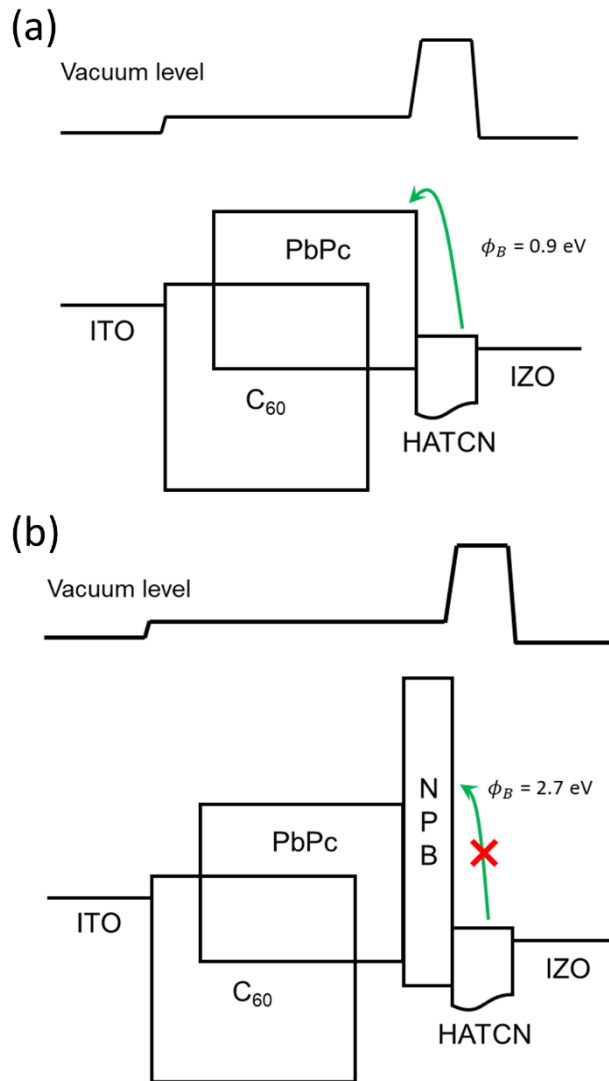
Figure 5.5 Schematic diagram of energy levels. (a) without NPB buffer layer (b) with NPB buffer layer

injection current due to electron injection from HATCN to PbPc, is introducing the electron blocking layer between HATCN and PbPc. Requirements of the electron blocking layer are higher LUMO level compared with LUMO level of PbPc, -3.9 eV from vacuum level, in order to increase the electron injection barrier and similar HOMO level with HOMO level of PbPc, -5.2 eV from vacuum level, for low extraction barrier.

NPB, well-known material for hole-transporting material, can meet these conditions. The HOMO level of NPB is -5.4 eV from vacuum level, leading to negligible injection and extraction barrier between NPB and PbPc. In addition, there is no barrier between NPB and HATCN. The LUMO level of NPB is -2.3 eV from vacuum level and expected electron injection barrier is 2.7 eV. To investigate the effect of the electron blocking layer, NPB was introduced between HATCN and PbPc, as shown in figure 5.5. Figure 5.6 shows the *J-V* curves of NIR OPDs with following structures; ITO (70 nm)/C_{60} (40 nm)/PbPc:C_{60} (2.5:1, 250 nm)/PbPc (40 nm)/without and with NPB buffer layer (40 nm)/HATCN (500 nm)/IZO (10 nm). With the diode equation, R_p, n, J_0 were extracted from *J-V* curves in range of -0.1 ~ 0 V (summarized in table 5.1). Using the model suggested above, the *J-V* characterisitics can be simulated.

Without NPB buffer layer, an injection current density is higher than a diode and a leakage current, meaning that injection current density is dominant in high reverse bias region. In this case, suppression of electron injection from HATCN can reduce the dark current density. On the other hand, with NPB

buffer layer, injection current density is negligible in all ranges. The fitting indicates that injection current from HATCN is effectively prevented with NPB buffer layer. Further reduction of dark current density requires decrease in leakage current density which is higher than diode current density.
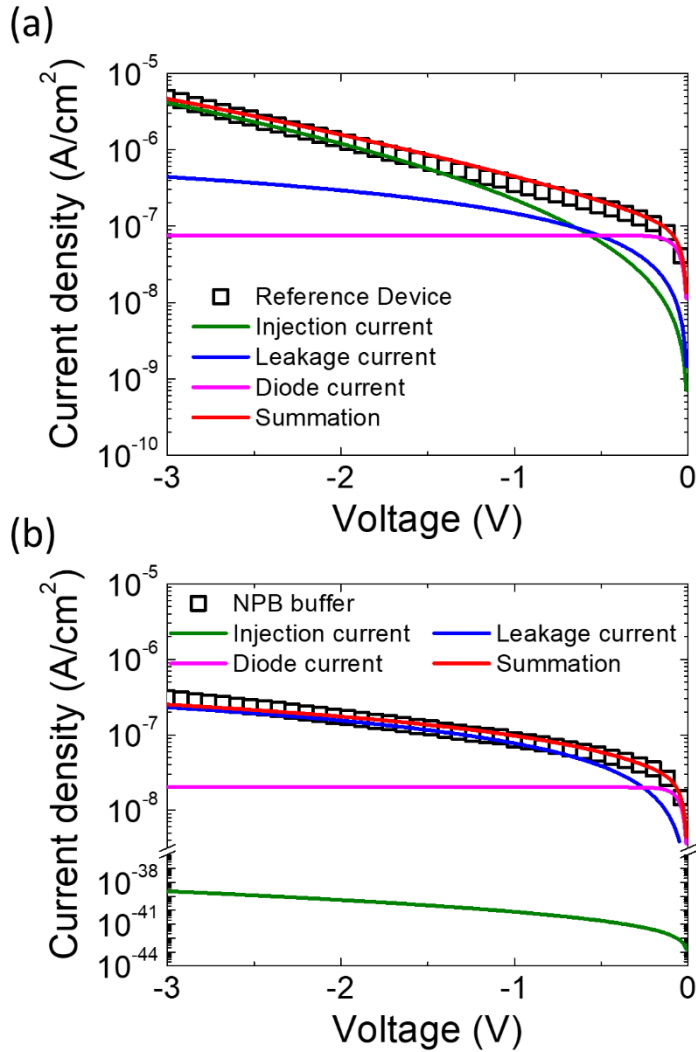
Figure 5.6 *J-V* curves of OPD in reverse bias region. Open symbols indicate experimental data. Blue, magenta and green color solid lines indicate simulated leakage current density, diode current density and injection current density from Scott-Milliaras model.

Table 5.1 Parameters used for simulation.

	J_0 (A/cm^2)[a]	n [a]	R_p (Ω cm^2) [a]	C_{effect}	ϕ_B (eV) [b]	μ (cm^2/Vs)	N_0 (#/m^3)	ε_r
Without NPB	7.6×10^{-8}	2.6	6.8×10^6	5.7	0.84	1.0 [c]	4.07×10^{26} [e]	3
With NPB	2.0×10^{-8}	2	1.3×10^7	8.6	2.7	0.001 [d]	1.0×10^{27}	3

a) Fitted from diode equation in range of -0.1 ~ 0 V

b) From energy levels and ICT model

c) Reference [118]

d) Reference [119]

e) Reference [111]

5.5 Conclusion

The dark current density can be divided into three types: diode current, leakage current and injection current. The diode current and leakage current can be expressed with Shockley diode equation and injection current can be expressed with Scott-Milliaras equation. Here, a theoretical model, combination of the equations, is suggested to describe the dark current density of NIR OPDs in reverse bias region. With an increase in thickness of HATCN buffer layer, dark current density decreased in low reverse bias region. However, dark current density saturated in high reverse bias region. At the high reverse bias region, injection current density is dominant and introducing NPB as electron blocking layer effectively suppress the injection current. Further reduction of dark current density requires decrease in leakage current density which is higher than diode current density.

Chapter 6. Summary and Conclusion

In chapter 2, we controlled the crystallinity of C_{70} in C_{70}-based organic photovoltaic cells. The crystallinity of 5% 4,4′-Cyclohexylidenebis[N,N-bis(4-methylphenyl)-benzenamine] (TAPC) doped C_{70} is improved significantly, especially the (111)-oriented face-centered cubic structure of C_{70}, if CuI was used as a templating layer. The device with oriented C_{70} domain with increased crystallinity exhibited higher hole mobility (3.3×10^{-5} cm^2 V^{-1} s^{-1}) and electron mobility (5.3×10^{-5} cm^2 V^{-1} s^{-1}) compared to reference one which exhibited hole mobility of 8.2×10^{-6} cm^2 V^{-1} s^{-1} and electron mobility of 3.4×10^{-5} cm^2 V^{-1} s^{-1}. The enhanced mobility led to higher charge extraction. As a result, the use of the templating layer in C_{70}-based solar cells with low donor concentration resulted in significant improvement of the fill factor from 0.51 to 0.57 and the power conversion efficiency from 5.56% to 6.23% under simulated AM 1.5G, 1 sun irradiation.

In chapter 3, we controlled the initial growth mode of lead (II) phthalocyanine (PbPc) molecules on to C_{60} substrate, which is required structure for the inverted near-infrared (NIR) OPDs which can be combined with n-channel silicon-based integrated circuits. A spectral response to 1,000 nm was achieved by depositing PbPc on a heated C_{60} layer to form a triclinic rather than a monoclinic phase. The change in initial growth mode was investigated with 10 nm thick PbPc layer on to C_{60} substrate by X-ray diffraction pattern. As a result, NIR OPDs with substrate heating exhibited a

much higher responsivity (35.8 mA/W at 960 nm) compared to a device fabricated without substrate heating (8.4 mA/W). The external quantum efficiency also increased from 0.9 to 4.4%.

In chapter 4, inverted NIR OPDs with bulk-heterojunction (BHJ) structure was fabricated in order to further enhancement of NIR response. In general, PbPc loses crystallinity in a blended layer, which is photo-active layer in OPDs with BHJ structure, resulting in weak NIR absorption in blend films. In this case, neither the use of a templating layer without heating nor substrate heating without the templating layer induced NIR absorption in the blend layer. To form the triclinic phase responsible for NIR light absorption, the substrate was heated during fabrication and C_{60} was used as a templating layer, as well as an electron extraction layer, for an inverted structure. NIR absorption near 950 nm was enhanced, and the structural properties of the film changed dramatically. The OPDs with enhanced NIR absorption exhibited a responsivity of 244 mA/W and an external quantum efficiency of 31.1% at a reverse bias of −3 V and 970 nm. The OPD detectivity also increased to 9.01×10^{12} cm Hz$^{1/2}$/W and 1.36×10^{11} cm Hz$^{1/2}$/W under zero and reverse bias of −3 V, respectively. Furthermore, the origin of the dark current density is investigated. The injection current is blocked by inserting a blocking layer which can suppress the injection of electrons and analyzed through a theoretical model (**In chapter 5**).

These results demonstrate that the controlling crystallinity and crystal structure is effective way to improve not only electrical property but also optical

property in organic optoelectrical device.

Bibliography

[1]   T. M. Clarke, J. R. Durrant, *Chem. Rev.* **2010**, *110*, 6736.

[2]   P. Kumar, S. Chand, *Prog. Photovoltaics Res. Appl.* **2012**, *20*, 377.

[3]   A. Moliton, J.-M. Nunzi, *Polym. Int.* **2006**, *55*, 583.

[4]   L.-Y. Lin, Y.-H. Chen, Z.-Y. Huang, H.-W. Lin, S.-H. Chou, F. Lin,
C.-W. Chen, Y.-H. Liu, K.-T. Wong, *J. Am. Chem. Soc.* **2011**, *133*,
15822.

[5]   Y.-H. Chen, L.-Y. Lin, C.-W. Lu, F. Lin, Z.-Y. Huang, H.-W. Lin, P.-
H. Wang, Y.-H. Liu, K.-T. Wong, J. Wen, D. J. Miller, S. B. Darling,
J. Am. Chem. Soc. **2012**, *134*, 13616.

[6]   P. Peumans, A. Yakimov, S. R. Forrest, *J. Appl. Phys.* **2003**, *93*, 3693.

[7]   H. Dong, H. Zhu, Q. Meng, X. Gong, W. Hu, *Chem. Soc. Rev.* **2012**,
41, 1754.

[8]   F. Hong, X. Guo, H. Zhang, B. Wei, J. Zhang, J. Wang, *Org. Electron.*
2009, *10*, 1097.

[9]   S. Kobayashi, T. Takenobu, S. Mori, A. Fujiwara, Y. Iwasa, *Appl.
Phys. Lett.* **2003**, *82*, 4581.

[10]   A. Hinderhofer, A. Gerlach, K. Broch, T. Hosokai, K. Yonezawa, K.
Kato, S. Kera, N. Ueno, F. Schreiber, *J. Phys. Chem. C* **2013**, *117*,

1053.

[11]   T. B. Singh, N. S. Sariciftci, H. Yang, L. Yang, B. Plochberger, H. Sitter, *Appl. Phys. Lett.* **2007**, *90*, 213512.

[12]   J.-P. Yang, Q.-J. Sun, K. Yonezawa, A. Hinderhofer, A. Gerlach, K. Broch, F. Bussolotti, X. Gao, Y. Li, J. Tang, F. Schreiber, N. Ueno, S.-D. Wang, S. Kera, *Org. Electron.* **2014**, *15*, 2749.

[13]   J.-L. Zhou, J.-S. Yu, X.-G. Yu, X.-Y. Cai, *Chinese Phys. B* **2012**, *21*, 027305.

[14]   Y. Li, W. Lv, X. Luo, L. Sun, F. Zhao, J. Zhang, J. Zhong, F. Huang, Y. Peng, *Org. Electron.* **2015**, *26*, 186.

[15]   W. Lv, J. Zhong, Y. Peng, Y. Li, X. Luo, L. Sun, F. Zhao, J. Zhang, H. Xia, Y. Tang, S. Xu, Y. Wang, *Org. Electron.* **2016**, *31*, 258.

[16]   T.-M. Kim, H. J. Kim, H.-S. Shim, M.-S. Choi, J. W. Kim, J.-J. Kim, *J. Mater. Chem. A* **2014**, *2*, 8730.

[17]   X. Wang, H. Li, Z. Su, F. Fang, G. Zhang, J. Wang, B. Chu, X. Fang, Z. Wei, B. Li, W. Li, *Org. Electron.* **2014**, *15*, 2367.

[18]   H.-S. Shim, H. J. Kim, J. W. Kim, S.-Y. Kim, W.-I. Jeong, T.-M. Kim, J.-J. Kim, *J. Mater. Chem.* **2012**, *22*, 9077.

[19]   J. Dai, X. Jiang, H. Wang, D. Yan, *Appl. Phys. Lett.* **2007**, *91*, 253503.

[20]   H. Jung Kim, H.-S. Shim, J. Whan Kim, H. Hwi Lee, J.-J. Kim, *Appl.*

Phys. Lett. **2012**, *100*, 263303.

[21]   S.-Y. Kim, W.-I. Jeong, C. Mayr, Y.-S. Park, K.-H. Kim, J.-H. Lee,
C.-K. Moon, W. Brütting, J.-J. Kim, *Adv. Funct. Mater.* **2013**, *23*,
3896.

[22]   J. Frischeisen, D. Yokoyama, C. Adachi, W. Brütting, *Appl. Phys. Lett.*
2010, *96*, 073302.

[23]   K. Itaka, M. Yamashiro, J. Yamaguchi, M. Haemori, S. Yaginuma, Y.
Matsumoto, M. Kondo, H. Koinuma, *Adv. Mater.* **2006**, *18*, 1713.

[24]   K. Vasseur, K. Broch, A. L. Ayzner, B. P. Rand, D. Cheyns, C. Frank,
F. Schreiber, M. F. Toney, L. Froyen, P. Heremans, *ACS Appl. Mater.
Interfaces* **2013**, *5*, 8505.

[25]   B. P. Rand, D. Cheyns, K. Vasseur, N. C. Giebink, S. Mothy, Y. Yi,
V. Coropceanu, D. Beljonne, J. Cornil, J. L. Brédas, J. Genoe, *Adv.
Funct. Mater.* **2012**, *22*, 2987.

[26]   J. W. Kim, H. J. Kim, T.-M. Kim, T. G. Kim, J.-H. Lee, J. W. Kim, J.-
J. Kim, *Curr. Appl. Phys.* **2013**, *13*, 7.

[27]   C. H. Cheng, J. Wang, G. T. Du, S. H. Shi, Z. J. Du, Z. Q. Fan, J. M.
Bian, M. S. Wang, *Appl. Phys. Lett.* **2010**, *97*, 083305.

[28]   K. Vasseur, B. P. Rand, D. Cheyns, L. Froyen, P. Heremans, *Chem.
Mater.* **2011**, *23*, 886.

[29] Y. Zhou, T. Taima, T. Miyadera, T. Yamanari, M. Kitamura, K. Nakatsu, Y. Yoshida, *Nano Lett.* **2012**, *12*, 4146.

[30] Z. . Ji, K. . Wong, P. . Tse, R. W. . Kwok, W. . Lau, *Thin Solid Films* **2002**, *402*, 79.

[31] T. V. Basova, V. G. Kiselev, V. A. Plyashkevich, P. B. Cheblakov, F. Latteyer, H. Peisert, T. Chassè, *Chem. Phys.* **2011**, *380*, 40.

[32] L. Ottaviano, L. Lozzi, A. . Phani, A. Ciattoni, S. Santucci, S. Di Nardo, *Appl. Surf. Sci.* **1998**, *136*, 81.

[33] Y. Kim, S. A. Choulis, J. Nelson, D. D. C. Bradley, S. Cook, J. R. Durrant, *Appl. Phys. Lett.* **2005**, *86*, 063502.

[34] Y. Sun, J. H. Seo, C. J. Takacs, J. Seifter, A. J. Heeger, *Adv. Mater.* **2011**, *23*, 1679.

[35] G. Li, Y. Yao, H. Yang, V. Shrotriya, G. Yang, Y. Yang, *Adv. Funct. Mater.* **2007**, *17*, 1636.

[36] W. Zhao, J. P. Mudrick, Y. Zheng, W. T. Hammond, Y. Yang, J. Xue, *Org. Electron.* **2012**, *13*, 129.

[37] T. Sakurai, T. Ohashi, H. Kitazume, M. Kubota, T. Suemasu, K. Akimoto, *Org. Electron.* **2011**, *12*, 966.

[38] T.-M. Kim, H. Shim, M. Choi, H. J. Kim, J. Kim, *ACS Appl. Mater. Interfaces* **2014**, *6*, 4286.

[39] A. Miyamoto, K. Nichogi, A. Taomoto, T. Nambu, M. Murakami, *Thin Solid Films* **1995**, *256*, 64.

[40] Y. Li, J. Zhang, W. Lv, X. Luo, L. Sun, J. Zhong, F. Zhao, F. Huang, Y. Peng, *Synth. Met.* **2015**, *205*, 190.

[41] R. W. Lof, M. A. van Veenendaal, B. Koopmans, H. T. Jonkman, G. A. Sawatzky, *Phys. Rev. Lett.* **1992**, *68*, 3924.

[42] W. Osikowicz, M. P. de Jong, W. R. Salaneck, *Adv. Mater.* **2007**, *19*, 4213.

[43] T. R. Ohno, Y. Chen, S. E. Harvey, G. H. Kroll, J. H. Weaver, R. E. Haufler, R. E. Smalley, *Phys. Rev. B* **1991**, *44*, 13747.

[44] K. Harigaya, *Phys. Rev. B* **1992**, *45*, 13676.

[45] S. Saito, A. Oshiyama, Y. Miyamoto, N. Hamada, S. Sawada, *Nanotechnology* **1992**, *3*, 167.

[46] N. S. Sariciftci, L. Smilowitz, A. J. Heeger, F. Wudl, *Science (80-.).* **1992**, *258*, 1474.

[47] M. Pope, C. E. Swenberg, *Electronic Processes in Organic Crystals and Polymers*, Oxford University Press, **1999**.

[48] Y. M. Wang, P. V Kamat, L. K. Patterson, *J. Phys. Chem.* **1993**, *97*, 8793.

[49] M. Zhang, H. Wang, H. Tian, Y. Geng, C. W. Tang, *Adv. Mater.* **2011**,

23, 4960.

[50]   X. Xiao, J. D. Zimmerman, B. E. Lassiter, K. J. Bergemann, S. R.

          Forrest, *Appl. Phys. Lett.* **2013**, *102*, 073302.

[51]   Y. Zheng, W. J. Potscavage, T. Komino, M. Hirade, J. Adachi, C.

          Adachi, *Appl. Phys. Lett.* **2013**, *102*, 143304.

[52]   Y. Zheng, W. J. Potscavage, T. Komino, C. Adachi, *Appl. Phys. Lett.*

          2013, *102*, 153302.

[53]   G. Chen, H. Sasabe, Z. Wang, X.-F. Wang, Z. Hong, Y. Yang, J. Kido,

          Adv. Mater. **2012**, *24*, 2768.

[54]   R. Pandey, A. A. Gunawan, K. A. Mkhoyan, R. J. Holmes, *Adv. Funct.*

          Mater. **2012**, *22*, 617.

[55]   K. Kudo, T. Saraya, S. Kuniyoshi, K. Tanaka, *Mol. Cryst. Liq. Cryst.*

          Sci. Technol. Sect. A. Mol. Cryst. Liq. Cryst. **1995**, *267*, 423.

[56]   B. Ecker, J. C. Nolasco, J. Pallarés, L. F. Marsal, J. Posdorfer, J. Parisi,

          E. von Hauff, *Adv. Funct. Mater.* **2011**, *21*, 2705.

[57]   W. Tress, A. Petrich, M. Hummert, M. Hein, K. Leo, M. Riede, *Appl.*

          Phys. Lett. **2011**, *98*, 063301.

[58]   C.-T. Lee, C.-H. Lee, *Org. Electron.* **2013**, *14*, 2046.

[59]   B. Yu, L. Huang, H. Wang, D. Yan, *Adv. Mater.* **2010**, *22*, 1017.

[60]   W. Chen, L. Huang, X. Qiao, J. Yang, B. Yu, D. Yan, *Org. Electron.*

physics, Mater. Appl. **2012**, *13*, 1086.

[61] K.-J. Baeg, M. Binda, D. Natali, M. Caironi, Y.-Y. Noh, *Adv. Mater.*
      2013, *25*, 4267.

[62] G. Konstantatos, E. H. Sargent, *Nat. Nanotechnol.* **2010**, *5*, 391.

[63] K.-H. Lee, D.-S. Leem, J. S. Castrucci, K.-B. Park, X. Bulliard, K.-S.
      Kim, Y. W. Jin, S. Lee, T. P. Bender, S. Y. Park, *ACS Appl. Mater.*
      Interfaces **2013**, *5*, 13089.

[64] D.-H. Kim, K.-S. Kim, H.-S. Shim, C.-K. Moon, Y. W. Jin, J.-J. Kim,
      Appl. Phys. Lett. **2014**, *105*, 213301.

[65] M. G. Han, K.-B. Park, X. Bulliard, G. H. Lee, S. Yun, D.-S. Leem,
      C.-J. Heo, T. Yagi, R. Sakurai, T. Ro, S.-J. Lim, S. Sul, K. Na, J. Ahn,
      Y. W. Jin, S. Lee, *ACS Appl. Mater. Interfaces* **2016**, *8*, 26143.

[66] Y. Higashi, K.-S. Kim, H.-G. Jeon, M. Ichikawa, *J. Appl. Phys.* **2010**,
      108, 034502.

[67] H.-W. Lin, S.-Y. Ku, H.-C. Su, C.-W. Huang, Y.-T. Lin, K.-T. Wong,
      C.-C. Wu, *Adv. Mater.* **2005**, *17*, 2489.

[68] X. Gong, M. Tong, Y. Xia, W. Cai, J. S. Moon, Y. Cao, G. Yu, C.-L.
      Shieh, B. Nilsson, A. J. Heeger, *Science (80-.)* **2009**, *325*, 1665.

[69] E.-C. Chen, S.-R. Tseng, Y.-C. Chao, H.-F. Meng, C.-F. Wang, W.-C.
      Chen, C.-S. Hsu, S.-F. Horng, *Synth. Met.* **2011**, *161*, 1618.

[70]   S. Matthew Menke, R. Pandey, R. J. Holmes, *Appl. Phys. Lett.* **2012**, *101*, 223301.

[71]   L. Xiao, S. Chen, X. Chen, X. Peng, Y. Cao, X. Zhu, *J. Mater. Chem. C* **2018**, *6*, 3341.

[72]   C. Montenegro Benavides, S. Rechberger, E. Spiecker, M. Berlinghof, T. Unruh, M. Biele, O. Schmidt, C. J. Brabec, S. F. Tedde, *Org. Electron.* **2018**, *54*, 21.

[73]   X. Liu, Y. Lin, Y. Liao, J. Wu, Y. Zheng, *J. Mater. Chem. C* **2018**, *6*, 3499.

[74]   M. Binda, T. Agostinelli, M. Caironi, D. Natali, M. Sampietro, L. Beverina, R. Ruffo, F. Silvestri, *Org. Electron.* **2009**, *10*, 1314.

[75]   X. Hu, Y. Dong, F. Huang, X. Gong, Y. Cao, *J. Phys. Chem. C* **2013**, *117*, 6537.

[76]   Z. Su, F. Hou, X. Wang, Y. Gao, F. Jin, G. Zhang, Y. Li, L. Zhang, B. Chu, W. Li, *ACS Appl. Mater. Interfaces* **2015**, *7*, 2529.

[77]   R. Nie, X. Deng, L. Feng, G. Hu, Y. Wang, G. Yu, J. Xu, *Small* **2017**, *13*, 1603260.

[78]   Z. Wu, W. Yao, A. E. London, J. D. Azoulay, T. N. Ng, *ACS Appl. Mater. Interfaces* **2017**, *9*, 1654.

[79]   Z. Tang, Z. Ma, A. Sánchez-Díaz, S. Ullbrich, Y. Liu, B. Siegmund,

A. Mischok, K. Leo, M. Campoy-Quiles, W. Li, K. Vandewal, *Adv. Mater.* **2017**, *29*, 1702184.

[80] S. Xiong, J. Tong, L. Mao, Z. Li, F. Qin, F. Jiang, W. Meng, T. Liu, W. Li, Y. Zhou, *J. Mater. Chem. C* **2016**, *4*, 1414.

[81] J. Han, D. Yang, D. Ma, W. Qiao, Z. Y. Wang, *Adv. Opt. Mater.* **2018**, *1800038*, 1800038.

[82] Y. Yao, Y. Liang, V. Shrotriya, S. Xiao, L. Yu, Y. Yang, *Adv. Mater.* **2007**, *19*, 3979.

[83] J. D. Zimmerman, V. V. Diev, K. Hanson, R. R. Lunt, E. K. Yu, M. E. Thompson, S. R. Forrest, *Adv. Mater.* **2010**, *22*, 2780.

[84] J. D. Zimmerman, E. K. Yu, V. V. Diev, K. Hanson, M. E. Thompson, S. R. Forrest, *Org. Electron.* **2011**, *12*, 869.

[85] T. Yang, K. Sun, X. Liu, W. Wei, T. Yu, X. Gong, D. Wang, Y. Cao, *J. Phys. Chem. C* **2012**, *116*, 13650.

[86] J. Qi, L. Ni, D. Yang, X. Zhou, W. Qiao, M. Li, D. Ma, Z. Y. Wang, *J. Mater. Chem. C* **2014**, *2*, 2431.

[87] L. Li, Y. Huang, J. Peng, Y. Cao, X. Peng, *J. Mater. Chem. C* **2014**, *2*, 1372.

[88] X. Hu, K. Wang, C. Liu, T. Meng, Y. Dong, S. Liu, F. Huang, X. Gong, Y. Cao, *J. Mater. Chem. C* **2014**, *2*, 9592.

[89]   H. Zhang, S. Jenatsch, J. De Jonghe, F. Nüesch, R. Steim, A. C. Véron, R. Hany, *Sci. Rep.* **2015**, *5*, 9439.

[90]   B. Siegmund, A. Mischok, J. Benduhn, O. Zeika, S. Ullbrich, F. Nehm, M. Böhm, D. Spoltore, H. Fröb, C. Körner, K. Leo, K. Vandewal, *Nat. Commun.* **2017**, *8*, 15421.

[91]   S. Tedde, E. S. Zaus, J. Furst, D. Henseler, P. Lugli, *IEEE Electron Device Lett.* **2007**, *28*, 893.

[92]   D. Baierl, B. Fabel, P. Lugli, G. Scarpa, *Org. Electron.* **2011**, *12*, 1669.

[93]   D. Baierl, B. Fabel, P. Gabos, L. Pancheri, P. Lugli, G. Scarpa, *Org. Electron.* **2010**, *11*, 1199.

[94]   J.-H. Lee, J.-J. Kim, *J. Inf. Disp.* **2013**, *14*, 39.

[95]   M. Takase, Y. Miyake, T. Yamada, T. Tamaki, M. Murakami, Y. Inoue, *Tech. Dig. - Int. Electron Devices Meet. IEDM* **2015**, *2016–Febru*, 30.2.1.

[96]   J. Janczak, Y. Marina Idemori, *Polyhedron* **2003**, *22*, 1167.

[97]   D. Placencia, W. Wang, R. C. Shallcross, K. W. Nebesny, M. Brumbach, N. R. Armstrong, *Adv. Funct. Mater.* **2009**, *19*, 1913.

[98]   M. Hiramoto, K. Kitada, K. Iketaki, T. Kaji, *Appl. Phys. Lett.* **2011**, *98*, 023302.

[99]   K. Yokoyama, T. Kaji, M. Hiramoto, *Jpn. J. Appl. Phys.* **2013**, *52*,

04CR06.

[100] M. C. Valsakumar, N. Subramanian, M. Yousuf, P. C. Sahu, Y. Hariharan, A. Bharathi, V. Sankara Sastry, J. Janaki, G. V. N. Rao, T. S. Radhakrishnan, C. S. Sundar, *Phys. Rev. B* **1993**, *48*, 9080.

[101] J. Gong, G. Ma, G. Chen, *J. Mater. Res.* **1996**, *11*, 2071.

[102] M. Limonov, Y. E. Kitaev, A. Chugreev, *Phys. Rev. B - Condens. Matter Mater. Phys.* **1998**, *57*, 7586.

[103] G. Wortmann, Y. S. Grushko, A. Bolotov, E. A. Bychkov, W. Bensch, H. Werner, R. Schlögl, *Mol. Cryst. Liq. Cryst. Sci. Technol. Sect. A. Mol. Cryst. Liq. Cryst.* **1994**, *245*, 313.

[104] C. H. B. Ng, W. Y. Fan, *J. Phys. Chem. C* **2007**, *111*, 9166.

[105] Y. Quo, N. Karasawa, W. a. Goddard, *Nature* **1991**, *351*, 464.

[106] S.-W. Liu, W.-C. Su, C.-C. Lee, C.-W. Cheng, C.-C. Chou, C.-F. Lin, *J. Electrochem. Soc.* **2012**, *160*, G14.

[107] J. Bisquert, G. Garcia-Belmonte, A. Munar, M. Sessolo, A. Soriano, H. J. Bolink, *Chem. Phys. Lett.* **2008**, *465*, 57.

[108] J. L. de Boer, S. van Smaalen, V. Petricek, M. DusekP, M. A. Verheijen, G. Meijer, *Chem. Phys. Lett.* **1994**, *219*, 469.

[109] V. D. Blank, S. G. Buga, G. A. Dubitsky, N. R. Serebryanaya, M. Y. Popov, B. Sundqvist, *Carbon N. Y.* **1998**, *36*, 319.

[110] K. Ukei, *Acta Crystallogr. Sect. B Struct. Crystallogr. Cryst. Chem.* **1973**, *B29*, 2290.

[111] Y. Iyechika, K. Yakushi, I. Ikemoto, H. Kuroda, *Acta Crystallogr. Sect. B Struct. Crystallogr. Cryst. Chem.* **1982**, *38*, 766.

[112] Y.-H. Tak, K.-B. Kim, H.-G. Park, K.-H. Lee, J.-R. Lee, *Thin Solid Films* **2002**, *411*, 12.

[113] K. Tvingstedt, C. Deibel, *Adv. Energy Mater.* **2016**, *6*, 1502230.

[114] M. Choi, S. Lee, H. J. Kim, J. Kim, *Org. Electron.* **2018**, *61*, 164.

[115] J. C. Scott, G. G. Malliaras, *Chem. Phys. Lett.* **1999**, *299*, 115.

[116] H. Mockert, D. Schmeisser, W. Gtipel, **1989**, *19*, 159.

[117] S. Braun, W. R. Salaneck, M. Fahlman, *Adv. Mater.* **2009**, *21*, 1450.

[118] W. Wacławek, M. Ząbkowska-Wacławek, *Thin Solid Films* **1987**, *146*, 1.

[119] S.-W. Liu, C.-C. Lee, W.-C. Su, C.-H. Yuan, C.-F. Lin, K.-T. Chen, Y.-S. Shu, Y.-Z. Li, T.-H. Su, B.-Y. Huang, W.-C. Chang, Y.-H. Liu, *Sci. Rep.* **2015**, *5*, 10384.

초 록

유기 반도체는 낮은 공정 비용, 가벼운 무게, 기판 유연성, 대면적 제조에 대한 적용 성 등의 이점이 있으며 이러한 특성으로 최근 많은 연구가 이루어지고 있다. 특히, 광 활성 물질로 제작되는 유기광전소자는 학계와 업계 모두에서 각광받고있는 연구주제이다. 유기광전소자는 빛 에너지와 전기 에너지를 서로 변환시킬 수 있는 장치를 말하며, 예를 들어 입사되는 빛 에너지로부터 자유 전하를 생성하여 전력을 생산하는 유기태양전지와 입사되는 빛을 검출하는 유기광검출기가 있다. 이러한 소자들은 유기 박막으로 이루어지며, 유기물이 박막을 형성할 경우 유기물 층의 결정도와 분자 배향에 따라 전기적 특성과 광학적 특성이 전체 소자 특성에 영향을 미친다. 따라서 결정 성장 제어 및 분자 배향 제어는 유기물의 전기적, 광학적 특성을 개선하기 위한 좋은 전략이 될 수 있다.

먼저, C_{70} 기반의 유기태양전지에서 광 활성 층을 이루고 있는 C_{70}의 결정도를 제어하였다. 5%의 4,4′-Cyclohexylidenebis[N,N-bis(4-methylphenyl)benzenamine] (TAPC)가 도핑 되어 있는 광 활성 층은 CuI를 배향 층으로 사용할 경우 확연한 결정도의 향상을 보였으며, 특히 (111) 방향의 면심 입방 구조가 뚜렷하게 관찰되었다. 결정도가 향상될 경우

116

정공의 이동도 값은 8.2 × 10^{-6} cm^2 V^{-1} s^{-1}에서 3.3 × 10^{-5} cm^2 V^{-1} s^{-1}로 증가하였으며 전자 이동도 값은 3.4 × 10^{-5} cm^2 V^{-1} s^{-1}에서 3.4 × 10^{-5} cm^2 V^{-1} s^{-1}로 증가하였다. 향상된 전하 이동도 값은 C_{70} 기반의 유기태양전지의 성능을 향상시켰다. 충진율이 0.51에서 0.57로 증가하였고, 그 결과 AM 1.5G, 1 Sun 조건에서 광전변환효율이 5.56% 에서 6.23% 로 증가하였다. 이는 CuI 배향층이 전자주개물질 뿐만 아니라 전자받개물질의 결정도를 효과적으로 제어할 수 있음을 시사한다.

두 번째로는 배향 효과를 이용하여 유기물의 흡수를 변화시키는 연구를 진행하였다. lead (II) phthalocyanine (PbPc) 는 비결정 또는 monoclinic 상을 이루고 있을 때 붉은 빛을 흡수하지만, triclinic 상을 이루게 되면 적외선의 빛을 흡수하게 된다. PbPc를 이용하여 실리콘 집적 회로와 접합하기 위하여 요구되는 역구조 유기광검출기를 설계하였고, 가열된 C_{60} 기판 위에 성장하는 PbPc는 적외선 흡수를 보이는 triclinic 상을 이루었다. 초기 성장 모드를 살펴보기 위하여 10 nm 두께의 얇은 PbPc 측을 C_{60} 기판 위에 형성하여 X-ray 측정을 진행하였으며, 기판 가열 여부에 따라 뚜렷한 차이를 보였다. 그 결과로 960 nm 에서 35.8 mA/W의 응답도를 갖는 유기광검출기를 제작할 수 있었다.

적외선 응답성을 증가시키기 위하여 혼합박막 구조를

도입하였다. PbPc는 혼합박막을 형성할 경우 결정도가 깨지게 되어 적외선을 흡수하지 못한다. 배향층의 도입 및 기판 가열 효과 모두 PbPc 기반 혼합박막의 적외선 흡수를 유도하지 못하였다. 우리는 앞서 사용한 C_{60} 이 배향효과가 있다는 것을 확인하고, 가열된 배향층을 도입함으로써 PbPc 기반 혼합박막의 적외선 흡수를 구현할 수 있었다. 950 nm 에서 흡수가 뚜렷하게 증가하였으며, 그 결과로 244 mA/W의 응답도 및 31.1%의 외부광자효율을 달성하였다. 970 nm 에서의 검출도는 9.01×10^{12} cm Hz$^{1/2}$/W로 증가하였다. 더 나아가, 암전류 밀도의 원인을 규명하고 전자의 주입을 억제할 수 있는 차단층을 삽입하여 주입전류를 차단하고 이를 이론적 모델을 통하여 분석하였다.

주요어: 유기태양전지, 배향층, 유기광검출기, 기판가열, 결정성장, 역구조 적외선 검출기

학번: 2014 – 30233

118

CURRICULUM VITAE

Min-Soo Choi

Department of Materials Science & Engineering

Seoul National University, Seoul, 151-744, Korea

+82-2-875-2412 (Office)

E-mail: momms711@snu.ac.kr

Education

2014.03 ~ 2018.08 **Ph.D.** in Materials Science & Engineering

Supervisor: Professor Jang-Joo Kim

Seoul National University, Seoul, Korea

2012.03 ~ 2014.02 **M.S.** in Materials Science & Engineering

Supervisor: Professor Jang-Joo Kim

Seoul National University, Seoul, Korea

2008.03 ~ 2012.02 **B.S.** in Materials Science & Engineering

Seoul National University, Seoul, Korea

Research Interests

Organic photovoltaic cells, Organic photodetector, Crystal analysis, Growth control, Templating, Heat-treatment of organic film, bulk-heterojunction, Inverted photodetector, Near-infrared photodetector

Professional Skills

- Design and fabrication of organic electronic devices: Thermal vacuum evaporator, Glove-box, Spin coater

- The optoelectronic analyses on organic semiconductors: UV-vis-NIR absorption spectroscopy, OPV & OPD characteristic measurements, refractive index

- Optical simulation for OPV & OPD

- The structural characterization of organic semiconductors: AFM, XRD, α-STEP

List of Publications

1. **<u>Min-Soo Choi</u>**, Jang-Joo Kim*, "Analysis of dark current density with theoretical model in PbPc-based near-infrared organic photodetectors", In preparation.

2. **<u>Min-Soo Choi</u>**, Sangmin Chae, Hyo Jung Kim, Jang-Joo Kim*, "Control of Crystallinity in PbPc:C_{60} Blend Film and Application for Inverted Near-Infrared Organic Photodetector", *ACS Applied Materials & Interfaces* DOI: 10.1021/acsami.8b08803

3. **<u>Min-Soo Choi</u>**, Siwoo Lee, Hyo Jung Kim, Jang-Joo Kim*, "Inverted near-infrared organic photodetector with oriented lead (II) phthalocyanine molecules via substrate heating" *Organic Electronics* 61, 164-169 (2018)

4. Beom-Soo Kim, Min-Hyung Choi, **<u>Min-Soo Choi</u>**, Jang-Joo Kim*, "Composition-controlled organometal halide perovskite via CH3NH3I pressure in vacuum codeposition process", *Journal of Materials Chemistry A* 4 (15), 5663-5668 (2016)

5. **<u>Min-Soo Choi</u>**, Tae-Min Kim, Hyun-Sub Shim, Beom-Soo Kim, Hyo Jung Kim, and Jang-Joo Kim*, "Enhancement of the Fill Factor through an Increase of the Crystallinity in Fullerene-Based Small-Molecule Organic Photovoltaic Cells", *ACS Applied Materials & Interfaces* 7 (17), 9134-9138 (2015)

6. Beom-Soo Kim, Tae-Min Kim, **Min-Soo Choi**, Hyun-Sub Shim, Jang-Joo Kim*, "Fully vacuum-processed perovskite solar cells with high open circuit voltage using MoO3/NPB as hole extraction layers", *Organic Electronics* 17, 102-106 (2015)

7. Jihun Kim, Hyun-Sub Shim, Horim Lee, **Min-Soo Choi**, Jang-Joo Kim, and Yongsok Seo, "Highly Efficient Vacuum-Processed Organic Solar Cells Containing Thieno[3,2-b]thiophene-thiazole", *The Journal of Physical Chemistry C* 118, 11559 (2014)

8. Tae-Min Kim, Hyo Jung Kim, Hyun-Sub Shim, **Min-Soo Choi**, Ji Whan Kim and Jang-Joo Kim, "The epitaxial growth of lead phthalocyanine on copper halogen compounds as the origin of templating effects", *Journal of Materials Chemistry A* 2, 8730 (2014)

9. Tae-Min Kim, Hyun-Sub Shim, **Min-Soo Choi**, Hyo Jung Kim and Jang-Joo Kim, "Multilayer Epitaxial Growth of Lead Phthalocyanine and C70 Using CuBr as a Templating Layer for Enhancing the Efficiency of Organic Photovoltaic Cells", *ACS Applied Materials & Interfaces* 6, 4286 (2014)

List of Presentations

International Conference

1. Beom-Soo Kim, Min-Hyung Choi, **<u>Min-Soo Choi</u>**, Jang-Joo Kim, "Composition-Controlled Organic/Inorganic Hybrid Perovskite via Working Pressure of CH3NH3I in Vacuum Co-Deposition Process", The 8th International Workshop on Flexible & Printable Electronics (2016 IWFPE), November 23-24 (November 23), 2016, Korea (Poster)

2. Beom-Soo Kim, Min-Hyung Choi, **<u>Min-Soo Choi</u>**, Jang-Joo Kim, "Composition-Controlled Perovskite Via CH3NH3I Pressure in Vacuum Co-Deposition Process", International Conference on Hybrid and Organic Photovoltaics (HOPV16), June 28-July 1 (June 29), 2016, United Kingdom (Poster)

3. Beom-Soo Kim, Tae-Min Kim, **<u>Min-Soo Choi</u>**, Hyun-Sub Shim, Jang-Joo Kim, "Fully vacuum-processed CH3NH3PbI3 perovskite solar cells with high open circuit voltage using MoO3/NPB layer", The International Symposium on Recent Advanes and Future Issues in Organic Electroluminscence (ISOEL2016), February 17-19 (February 18), 2016, Korea (Poster)

4. **<u>Min-Soo Choi</u>**, Tae-Min Kim, Hyun-Sub Shim, Beom-Soo Kim, Hyo Jung Kim, Jang-Joo Kim, "Enhancement of the Fill Factor through an Increment of the Crystallinity in Fullerene-Based Small-Molecule Organic Photovoltaic Cells", The International Symposium on Recent Advanes and

Future Issues in Organic Electroluminscence (ISOEL2016), February 17-19 (February 18), 2016, Korea (Poster)

5. **<u>Min-Soo Choi</u>**, Tae-Min Kim, Hyun-Sub Shim, Beom-Soo Kim, Hyo Jung Kim, and Jang-Joo Kim, "Enhancement of the fill factor through an increase of the crystallinity in fullerene-based small-molecule organic photovoltaic cells", The 7th International Workshop on Flexible & Printable Electronics 2015 (IWFPE 2015), November 4-6 (November 5), 2015, Korea (Poster)

6. Beom-Soo Kim, Tae-Min Kim, **<u>Min-Soo Choi</u>**, Hyun-Sub Shim, Jang-Joo Kim, "Fully vacuum co-deposited CH3NH3PbI3 perovskite solar cell with 1.12 V of circuit voltage employing MoO3/NPB layers as a hole transport layers", The 7th International Workshop on Flexible & Printable Electronics 2015 (IWFPE 2015), November 4-6 (November 5), 2015, Korea (Poster)

7. **<u>Min-Soo Choi</u>**, Tae-Min Kim, Hyun-Sub Shim, Beom-Soo Kim, Hyo Jung Kim, and Jang-Joo Kim, "Enhancement of The Fill Factor through An Increase of The Crystallinity in Fullerene-based Small-Molecule Organic Photovoltaic Devices", KJF-ICOMEP 2015, September 6-9 (September 7), 2015, Korea (Poster)

8. Beom-Soo Kim, Tae-Min Kim, **<u>Min-Soo Choi</u>**, Hyun-Sub Shim, and Jang-Joo Kim, "Fully Vacuum Deposited CH3NH3PbI3 Perovskite Solar Cells with High Open Circuit Voltage Using MoO3/NPB Layers", KJF-ICOMEP 2015, September 6-9 (September 7), 2015, Korea (Poster)

9. **<u>Min-Soo Choi</u>**, Tae-Min Kim, Hyun-Sub Shim, Beom-Soo Kim, Hyo Jung Kim, and Jang-Joo Kim, "Enhancement of fill factor through increase of crystallinity in fullerene based small molecule organic photovoltaic cells", 26th International Conference on Molecular Electronics and Devices (IC ME&D 2015), May 21-22 (May 22), 2015, Korea (Poster)

10. Beom-Soo Kim, Tae-Min Kim, **<u>Min-Soo Choi</u>**, Hyun-Sub Shim and Jang-Joo Kim, "Fully vacuum-processed CH3NH3Pb3I3 perovskite solar cells with high open circuit voltage using MoO3/NPB layer", International Conference on Hybrid and Organic Photovoltaics 2015 (HOPV15), May 10-13 (May 12), 2015, Italy (Poster)

11. **<u>Min-Soo Choi</u>**, Tae-Min Kim, Hyun-Sub Shim, Beom-Soo Kim and Jang-Joo Kim, "Enhancement of Fill Factor via Increase of Crystallinity in Fullerene Based Small Molecule Organic Photovoltaic Cells Using Copper Iodide as a Templating Layer", The 6th Asian Conference on Organic Electronics (A-COE 2014), November 12-14 (November 13), 2014, Taiwan (Poster)

12. Beom-Soo Kim, Tae-Min Kim, **<u>Min-Soo Choi</u>**, Hyun-Sub Shim and Jang-Joo Kim, "Fully-Vacuum Processed Perovskite Solar Cells with High Open Circuit Voltage Using MoO3/NPB Layers", The 6th Asian Conference on Organic Electronics (A-COE 2014), November 12-14 (November 13), 2014, Taiwan (Poster)

13. Tae-Min Kim, Hyun-Sub Shim, **<u>Min-Soo Choi</u>**, Hyo Jung Kim and Jang-Joo Kim, "Multi-layer Epitaxial Growth of Lead-Phthalocyanine and C70

Using CuBr as a Templating Layer for Enhancing the Efficiency of Organic Photovoltaic Cells", 10th International Conference on Electroluminescence and Organic Optoelectronics (ICEL), August 31-September 3, 2014, Germany (poster)

14. Tae-Min Kim, Hyun-Sub Shim, **<u>Min-Soo Choi</u>**, Hyo Jung Kim and Jang-Joo Kim, "Multilayer Epitaxial Growth of Lead Phthalocyanine and C70 Using CuBr as a Templating Layer for Enhancing the Efficiency of Organic Photovoltaic Cells", 2014 Joint Symposium of Korean Society of Photoscience - Korea Organic Solar Cell Society, Jun 20-21, 2014, Korea (Poster)

15. Tae-Min Kim, Hyun-Sub Shim, **<u>Min-Soo Choi</u>**, and Jang-Joo Kim, "Multi-layer epitaxial growth of lead-phthalocyanine and C70 using CuBr as a templating layer for the efficiency enhancement of organic photovoltaic cells", 5th Asian Conference on Organic Electronics (A-COE 2013), November 13-15 (November 15), 2013, Korea (poster)

16. Tae-Min Kim, Hyun-Sub Shim, **<u>Min-Soo Choi</u>**, and Jang-Joo Kim, "Heteroepitaxial growth of lead-phthalocyanine and C70 using CuBr as a templating layer for the efficieny enhancement of organic photovoltaic cells", IRTG 2013 (8th German-Korean Polymer Symposium), August 26-29 (August 28), 2013, Germany (poster)

Domestic Conference

1. 김범수, 최민형, **<u>최민수</u>**, 김장주, "Composition-controlled organic/inorganic hybrid perovskite via CH3NH3I pressure in vacuum co-deposition process", 2016 한국고분자학회 춘계학술대회, April 6-8 (April 7), 2016, Korea (Poster)

2. **<u>Min-Soo Choi</u>**, Tae-Min Kim, Hyun-Sub Shim, Beom-Soo Kim, Hyo Jung Kim, Jang-Joo Kim, "Enhancement of the Fill Factor through an Increase of the Crystallinity in Fullerene-Based Small-Molecule Organic Photovoltaic Cells", 2015 Materials Fair, October 1

3. **<u>최민수</u>**, 김태민, 심현섭, 김범수, 김효정, 김장주, "Enhancement of fill factor via increase of crystallnity in fullerene based small molecule organic photovoltaic cells using copper iodide as a templating layer", 2015 한국고분자학회 춘계학술대회, April 8-10 (April 9), 2015, Korea (Poster)

4. 김범수, 김태민, **<u>최민수</u>**, 심현섭, 김장주, "Fully vacuum-processed perovskite solar cells with Voc of 1.12 V employing MoO3/NPB layer", 2015 한국고분자학회 춘계학술대회, April 8-10 (April 9), 2015, Korea (Poster)

5. **<u>최민수</u>**, 김지환, 김효정, 김장주, "The comparision of C60 and C70 in bulk heterojunctions formed by alternation thermal deposition", 2013 한국고분자학회 춘계학술대회, April 11-12, 2013